Master's thesis

NTNU
Norwegian University of Science and Technology
Faculty of Engineering
Department of Civil and Environmental Engineering

Ole Jakob Bedringås

Hydraulic modeling of free surface flow and scour around bridge piers

Master's thesis in Civil and Environmental Engineering
Supervisor: Elena Pummer
Co-supervisor: Wolfgang Richter, Nils Solheim Smith
March 2023

NTNU
Norwegian University of
Science and Technology

Ole Jakob Bedringås

Hydraulic modeling of free surface flow and scour around bridge piers

Master's thesis in Civil and Environmental Engineering
Supervisor: Elena Pummer
Co-supervisor: Wolfgang Richter, Nils Solheim Smith
March 2023

Norwegian University of Science and Technology
Faculty of Engineering
Department of Civil and Environmental Engineering

NTNU
Norwegian University of
Science and Technology

M.Sc. Thesis Agreement

The aim of the Master Thesis is to investigate scour processes around the pillars of the Sluppen bridge using CFD. OpenFOAM will be the main CFD-software, and the scouring will be related to the riverbed shear stress. Additional CFD software (Ansys Fluent, Flow 3D, SedFOAM) will be considered if there is enough time. Before, the inhabitants of Trondheim could kayak in the standing wave located near the Sluppen bridge in the Nidelva river. However, bathymetric surveys showed that scour holes had appeared downstream of the Sluppen bridge. The scour holes were filled with rockfill material to protect the bridge. Unfortunately, the kayak wave disappeared when the scour holes were removed. This topic will shed light on the scour processes today and facilitate for further studies on how the kayak wave can be reestablished without endangering the stability of the Sluppen bridge.

Abstract

Previously, kayakers used to be able to surf a standing wave located under Sluppen bridge in the river Nidelva in Trondheim. However, bathymetric surveys revealed that a scour hole had been formed downstream of the bridge piers. The scour hole has since been refilled, but this incident revealed the scour potential of the bridge piers. Unfortunately, the standing wave disappeared after the scour hole was refilled. This thesis aims to shed light on the current scour processes induced by the Sluppen bridge piers and facilitate for further studies on how the kayak wave can be reestablished without endangering the stability of Sluppen bridge.

A section of Nidelva past Sluppen bridge is simulated. The multiphase solver interFoam, part of the CFD toolbox OpenFOAM, is used to simulate the river. A scour model is developed to determine the critical sediment diameter at the riverbed. First, the shear stress on the riverbed is sampled using ParaView. Then, the critical sediment diameter is defined as the sediment diameter that makes the dimensionless critical shear stress equal to the bed slope corrected, dimensionless critical shear stress. The bed slope correction factor considers the angle parallel to and normal to the flow direction. The critical sediment diameter is calculated for three different discharges and the simulated water level is compared against measurements, but not further calibrated.

Fifteen two-dimensional channel simulations are performed to relate the sand-grain roughness, k_s, in interFoam to the Manning-Strickler number, K_{st}. Additionally, the simulated shear stresses are compared against the theoretical shear stress for uniform flow in the two-dimensional channel simulation. Finally, a 1:31.5 physical model is constructed to demonstrate how a surf wave can be recreated under Sluppen bridge.

Sammendrag

Tidligere kunne kajakkpadlere surfe på en stående bølge under Sluppen bru i Nidelva i Trondheim. Imidlertid avslørte batymetrimålinger at ei erosjonsgrop hadde dannet seg nedstrøms bropilarene. Erosjonsgropa ble fylt igjen, men hendelsen avslørte erosjonspotensialet til brupilene. Den stående bølgen forsvant etter igjenfyllingen av erosjonsgropa. Denne masteroppgaven vil belyse dagens skuringsprosesser indusert av Sluppen brupilarer og legge til rette for videre studier av hvordan kajakkbølgen kan reetableres uten å sette stabiliteten til Sluppen bru i fare.

Et elvestrekke av Nidelva ved Sluppen bru er simulert. Den numeriske flerfaseløseren interFoam, en del av CFD-verktøykassen OpenFOAM, brukes til å simulere elvestrekket. En erosjonsmodell er utviklet for å finne den kritiske sedimentdiameteren ved elvebunnen. Først blir skjærspenningene ved elvebunnen hentet ut ved hjelp av ParaView. Deretter blir den kritiske sedimentdiameteren beregnet som den diameteren som gjør den dimensjonsløse kritiske skjærspenningen lik den dimensjonsløse kritiske skjærspenningen korrigert for bunnhelning. Korreksjonen for bunnhelning tar hensyn til bunnhelningen parallelt med og normalt på strømningsretningen. Den kritiske sedimentdiameteren er beregnet for tre ulike vannføringer og den simulerte vannstanden sammenlignes med vannstandsmålinger, men kalibreres ikke videre.

Femten simuleringer av todimensjonale kanaler er gjennomført for å relatere sandkornruheten, k_s, i interFoam til Mannings ruhetstall, K_{st}. De simulerte skjærspenningene sammenlignes med den teoretiske skjærspenningen for uniform strømning i kanalsimuleringen. En fysisk modell med skala 1:31.5 er til slutt konstruert for å gi en pekepinn på hvordan en surfebølge kan gjenskapes under Sluppen bru.

Acknowledgements

I will start by thanking my supervisors because this thesis would not have been possible without them. My supervisor at NTNU, associate professor Elena Pummer, my co-supervisor at NTNU, PhD candidate Nils Solheim Smith and the supervisor at TU Graz, Dipl. -Ing. Wolfgang Richter were all to great help and support throughout the entire process.

In addition, PhD candidate at TU Graz, Misagh Moradali provided valuable insight into the field of numerical modelling. Nils Reidar Olsen, professor at NTNU, gave advise on shear stress calculations in computational fluid dynamics, while Dipl. -Ing Gerald Krebs at TU Graz assisted me with QGIS. Josef Markus Saurer built the piers for the physical model and Dietmar Schofauer helped me whenever I was lost in the laboratory.

Thanks to every one of you!

Table of contents

List of Figures

List of Tables

Abbreviations

ADCP	Acoustic Doppler Current Profiler
CFD	Computational Fluid Dynamics
CFD-DEM	Computational Fluid Dynamics – Discrete Element Method
CFL	Courant-Friedrichs-Lewy
DEM	Digital Elevation Model
DTM	Digital Terrain Model
NTNU	Norwegian University of Science and Technology university
RANS	Reynolds-averaged Navier-Stokes
VOF	Volume of Fluid

Symbols

μ	Angle of repose (Deg)
ω	Angle between length axis of pier and flow direction (Deg)
g	Acceleration of gravity (m/s^2)
$q_{bed\ load}$	Bed load transport rate (kg/ms)
K	Bed slope correction factor (-)
α	Bed slope normal to flow direction (Deg)
ϕ	Bed slope parallel to flow direction (Deg)
Δx	Cell length (m)
C	Courant number (-)
d_c	Critical sediment diameter (m)
τ_0	Critical shear stress on a flat riverbed (N/m^2)
τ_c	Critical shear stress on a sloped riverbed (N/m^2)
ρ	Density (kg/m^3)
y	Depth (m)
θ_c	Dimensionless critical shear stress (-)
θ	Dimensionless shear stress (-)
u^+	Dimensionless velocity (-)
y^+	Dimensionless wall distance (-)
Q	Discharge (m^3/s)
Q_{model}	Discharge in physical model (m^3/s)
Q_{model}	Discharge in prototype (m^3/s)
d	Distance from riverbed to point in the stream (m)
β	Empirical factor relating k_s to K_{st} (m$^{0.5}$/s)
C	Empirical factor for turbulent kinetic energy shear stress (-)
f	External force (m/s$_2$)
u'	Fluctuating component of the velocity (m/s)
F_r	Froude number (-)
$F_{r_{control}}$	Froude number control calculation (-)
$F_{r_{model}}$	Froude number in physical model (-)
$F_{r_{prototype}}$	Froude number in prototype (-)
ν	Kinematic viscosity (m^2/s)
$L_{protection}$	Length of scour protection (m)

l	Length of pier (m)
K_{st}	Manning-Strickler number ($m^{1/3}/s$)
n	Normal vector (-)
C_{max}	Maximum Courant number (-)
$X_{Objective}$	Objective function for equilibrium scour models
Re^*	Particle Reynolds number (-)
p	Pressure (kg/m^3)
k_s	Sand-grain roughness (m)
k_s^+	Sand-grain roughness in wall units (-)
d_s	Sediment diameter (m)
d_x	Sediment diameter larger than the diameter of x% of mass (m)
K_f	Shape factor for bridge piers (-)
τ	Shear stress (N/m^2)
τ_k	Shear stress calculated from turbulent kinetic energy (N/m^2)
τ_R	Shear stress calculated from Reynolds stress tensor (m^2/s^2)
R	Shear stress symmetric tensor (m^2/s^2)
u_*	Shear velocity (m/s)
u_τ	Shear velocity at a wall (m/s)
I	Slope of water surface (-)
s	Specific gravity (-)
t	Time (s)
Δt	Time step (s)
$\bar{u}$	Time-averaged velocity (m/s)
k	Turbulent kinetic energy (m^2/s^2)
ϵ	Turbulent energy dissipation rate (m^2/s^3)
q	Unit discharge (m^2/s)
u	Velocity (m/s)
V_{lokal}	Velocity upstream bridge pier nose (m/s)
κ	von Karman coefficient (-)
a	Width of pier (m)

1 Introduction

1.1 General

A hydraulic structure placed in a river will alter the flow and can lead to scour of the riverbed. Bridge piers are particularly susceptible to scour, such as local scour, contraction scour and natural scour. Contraction scour is caused by accelerated flow under bridges. The bridge opening is smaller than the natural river width and the flow velocities and shear stresses increase between the bridge piers and between the piers and abutments. Furthermore, heavy turbulence can occur downstream of the bridge and lead to scour (Fergus, Hoseth, & Sæterbø, 2010).

53% of bridge failures in the US are assumed to be caused by bridge scour (Wardhana & Hadipriono, 2003), but it may be a less significant reason in Norway, where the rock quality is generally good. Nonetheless, bridge scour is not an uncommon occurrence. The bridge Badderen bru in North Troms nearly collapsed due to scour in 2022. In response, the Norwegian Public Roads Administration decided to increase its efforts to prevent bridge scour (Statens vegvesen, 2022). In addition, climate changes may increase the future cost of bridge scouring due to greater floods (Nemry & Demirel, 2012).

Multiple studies use computational fluid dynamics (CFD) to estimate scour. There is a great variety of numerical scour models, but they can be generalized into three different model types. *Sediment transport rate models* have independent flow and scour models. The shear stress induced by the flow field is the scour agent. *Two-phase models* treat the sediments as a phase and include the sediment-flow interactions. Finally, *CFD-DEM models* simulate the motion of individual particles (Zhao, 2022).

The study focuses on the Sluppen bridge in Trondheim, Norway, where the large bridge piers have caused a scour hole downstream of the bridge. The piers obstruct the flow and increase the upstream water level. The flow is accelerated between the piers and then slowed down by the downstream subcritical flow. In the past, the site was suitable for river surfing, both for kayakers and surfers. However, for the safety of the bridge stability, the scour hole was refilled, and the surf wave disappeared. The kayak community in Trondheim wanted the surf wave back and the municipality of Trondheim decided to investigate the problem. This thesis will mainly focus on conducting CFD simulations of the existing river and creating suitable post-processing tools for the numerical simulation. The multiphase solver interFoam, part of the CFD toolbox OpenFOAM, is used for the numerical simulations. A smaller section of this thesis will be dedicated to a qualitative physical model study with the aim of recreating the surf wave under Sluppen bridge.

In this study, a scour model for computing critical sediment diameter at the riverbed is developed as a post-processing tool for CFD-simulations. The tool is suitable for numerical models of large-scale hydraulic problems. The aim of the scour model is to find the sediment diameters which make the dimensionless shear stresses at the riverbed equal to the dimensionless critical shear stress. A reduction factor of the critical sediment diameter which considers the slope of the riverbed is also implemented. These steps are equivalent to the first calculation steps of *sediment transport rate models*. However, contrary to *sediment transport rate models*, sediment transport is not computed. In addition, a post-

processing code for the local Froude number along an arbitrary slice of the river domain is developed. Both the code for the critical sediment diameter and the local Froude number are tested on the two-dimensional channel simulation. Finally, fifteen two-dimensional channel simulations are performed to obtain a relationship between the equivalent sand-gran roughness, k_s, in InterFoam, and the Manning-Strickler number.

1.2 Description of the site

Sluppen bridge is located over the river Nidelva in the city of Trondheim, Norway (Figure 1 and Figure 2). The first bridge at the site was built in 1864, while the current beam bridge was finished in 1977. However, the bridge piers are original from 1864 (Fremstad & Thingstad, 2007). Upstream of the bridge, there is a discharge gauge with daily recordings of discharge data since 1881 (Figure 1). A hydroelectric power plant, *Nedre Leirfoss Kraftverk*, is located 2.5 km upstream of the bridge. The power plant is the closest of several upstream plants that together regulate the discharge in Nidelva (Statkraft, 2022). The median discharge of Nidelva is 94 m^3/s (The Norwegian Water Resources and Energy Directory, 2023).

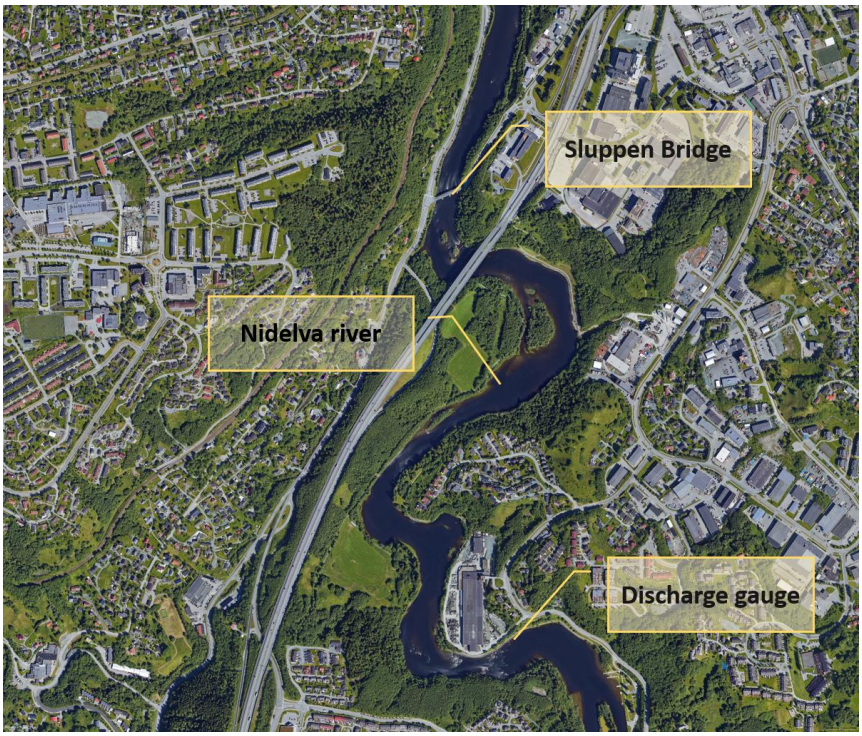

Figure 1: Plan view of Sluppen bridge (Google Earth Pro, 2017).

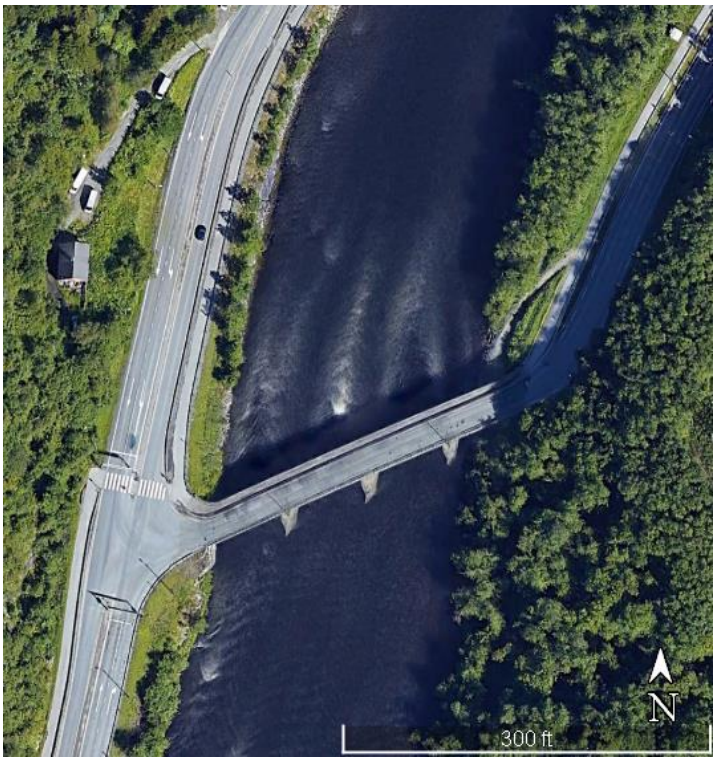

Figure 2: Plan view of Sluppen bridge with larger scale (Google Earth Pro, 2017)

The consulting company SWECO did bathymetric surveys of the riverbed in 2015 and 2018. These surveys revealed a scour hole downstream of the bridge as illustrated in Figure 3. In addition, the 2018 survey revealed that the scour hole had moved closer to the bridge since 2015. The development of the scour hole was assumed to threaten the stability of the bridge, and it was decided to refill the scour hole. There is no documentation of the refill material or its extent.

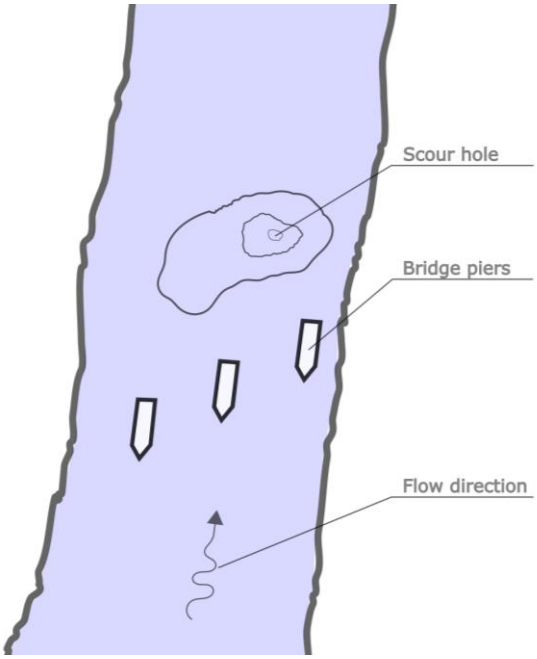

Figure 3: The current scour hole is located downstream of the bridge piers.

The bridge piers are shown in Figure 4. The flow is restricted by the piers, and the upstream water level is higher than the downstream water level. The flow is accelerated between the piers and turbulence, air entrainment and surface waves are visible in the pictures.

Figure 4: Sluppen bridge from the downstream side (picture provided by NTNU).

2 Theory

2.1 Hydraulics

2.1.1 Bridge scour

Bridge scour is typically divided into natural scour, local scour, and contraction scour. Altogether, they contribute to the total scour at the location of a bridge (Parker, Bratton, S., & D., 1997).

1. Local scour refer to scour that happens near the piers and abutments. The flow is obstructed and displaced near the constructions, which increases the local velocities. In addition, horse-shoe vortices can create downward-facing velocity vectors towards the foot of the construction (Lai, Liu, Bombardelli, & Song, 2022).
2. Contraction scour occurs when the channel width is narrowed due to a bridge or another structure. The piers, abutments or bridge embankment reduces the cross-sectional area of the river under the bridge and the flow velocities increase. Downstream of the bridge, the cross-sectional area is suddenly increasing, which can induce heavy turbulence (Fergus, Hoseth, & Sæterbø, 2010).
3. Natural scour is the scour happening at the bridge location independently of the bridge.

2.1.2 Shields diagram

The Shields diagram (Shields, 1936) determines the incipient motion of a sediment particle on a flat channel bed. Shields parameter $\theta\ (-)$, the dimensionless shear stress, is calculated as follows:

$$\theta = \frac{\tau}{\rho \cdot g \cdot (s-1) \cdot d_s} \tag{2.1}$$

Here, $\tau\ (N/m^2)$ denotes the shear stress, $\rho\ (kg/m^3)$ denotes the fluid density, $s\ (-)$ is the specific gravity of the sediment, $g\ (m/s^2)$ denotes the acceleration of gravity, and $d_s\ (m)$ refers to the sediment diameter. The derivation of θ is based on equilibrium of shear forces on the bed (Fergus, Hoseth, & Sæterbø, 2010). Shields diagram shows the relation between the dimensionless shear stress, and the particle Reynolds number $Re^*\ (-)$:

$$Re^* = \frac{u_* d_s}{\nu} \tag{2.2}$$

The parameter $\nu\ (m^2/s)$ denotes kinematic viscosity and $u_*\ (m/s)$ denotes the shear velocity, which is defined as $\sqrt{\tau/\rho}$. The incipient motion of a particle occurs when the dimensionless shear stress exceeds a critical value in the Shields diagram. In the following, this dimensionless critical shear stress on a flat riverbed is denoted θ_c. For gravel and coarser sediments, θ_c is approximately constant. However, experimental studies show a great scatter in this constant θ_c (Buffington & Montgomery, 1999). Buffington and Montgomery (1999) suggest $\theta_c = 0.045$, while Fergus et al. proposes $\theta_c = 0.05$. The scatter of the constant θ_c points to the fact that a portion of the sediments with a uniform grain size distribution start to move below $\theta_c = 0.045$. Experiments are mainly done with a uniform grain size distribution but experiments with non-uniform grain size distributions show that the substitution $d_{60} = d_s$ is acceptable.

If the riverbed has a downhill slope, a particle on the bed will have a gravitational component acting on it in the stream direction, and less shear stress is needed to initiate movement of the particle. It has been shown that there is a reduction of the critical shear stress for a downhill slope. Similarly, critical shear stress is higher for an uphill slope. Furthermore, the slope normal to the flow is shown to reduce the dimensionless critical shear stress. A formulation of the bed slope correction of the critical shear stress, considering both the bed angle parallel and normal to the flow direction, is (Dey, 2001):

$$K = 0.954 \cdot \left(1 - \frac{\phi}{\mu}\right)^{0.745} \cdot \left(1 - \frac{\alpha}{\mu}\right)^{0.372} \tag{2.3}$$

with

$$\tau_c = K \cdot \tau_0 \tag{2.4}$$

Here, critical shear stress on a flat riverbed, τ_0, must be multiplied with the bed slope correction factor $K\,(-)$ to get the critical shear stress of an inclined riverbed, τ_c. The angle $\alpha\,(degree)$ denotes the angle of the bed slope normal to the flow, the angle $\phi\,(degree)$ is the angle of the bed slope parallel to the flow and $\mu\,(degree)$ is the angle of repose. The angle of repose is observed to vary for uphill and downhill slopes (Lysne, 1969). Walstra et al. (2007) proposed a slightly different variant of the bed slope correction of the critical shear stress based on Dey (2001):

$$K = \left(1 - \frac{\phi}{\mu}\right)^{0.75} \cdot \left(1 - \frac{\alpha}{\mu}\right)^{0.37} \tag{2.5}$$

2.1.3 Scour protection regulations

The Norwegian regulation for scour protection is found in Jenssen and Tesaker (2009). This regulation states that the riprap should extend two times the width of the pier in all directions of the pier, but at least 2 meters (Figure 5). If the bridge piers are not aligned with the flow direction, a larger area must be protected. In this case, the riprap should extend two times the projected width of the pier perpendicular to the flow direction in all directions. However, it is difficult to build the piers parallel to the flow direction in practice.

Jenssen and Tesaker (2009) illustrate this with an example of the extent of the scour protection: A bridge is located on a river bend and the assumed angle of deviation between the length axis of the pier and the flow direction is 15 degrees. The formula for the length of the scour protection to each side of the pier, $L_{protection}\,(m)$, is:

$$L_{protection} = (a + l \cdot \sin(\omega)) \cdot 2 \tag{2.6}$$

The parameter $l\,(m)$ denotes the length of the pier, $a\,(m)$ denotes the width of the pier and $\omega\,(degrees)$ denotes the angle between the length axis of the pier and the flow direction. Figure 5 illustrates the Norwegian scour protection for a bridge pier. The width of the pier is a, and the scour protection is $2a$ to all sides of the pier. The flow direction is parallel to the length axis of the pier.

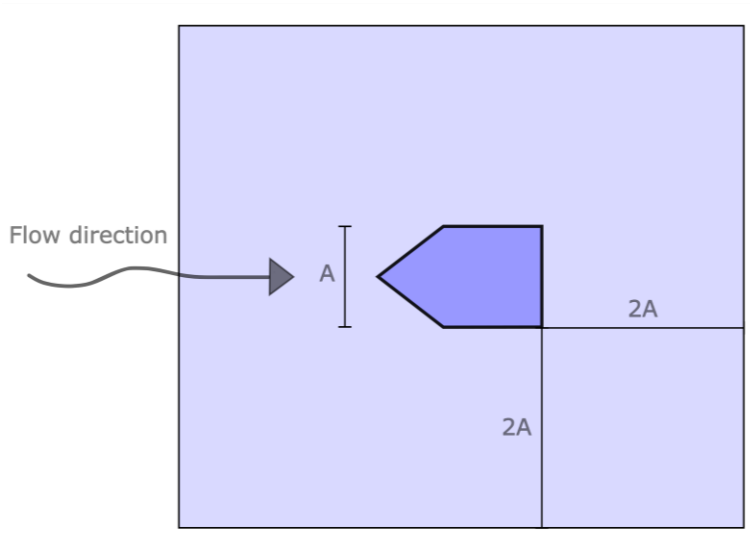

Figure 5: Norwegian scour protection regulation for a bridge pier.

Jenssen and Tesaker (2009) cover scour protection around the piers and abutments, but state that the long-term degradation should be evaluated separately. A lowered riverbed can propagate upstream towards the bridge piers and threaten the stability of the scour protection. Jenssen and Tesaker (2009) propose that extending the scour protection downstream of the bridge to prevent degradation of the riverbed might be necessary in certain cases. Scour may still occur outside of the scour protection if only the minimum requirements are met.

In addition, the greatest floods do not always pose the most critical situations: smaller floods can produce higher velocities and greater potential of scour. Thus, different flow rates should be evaluated. A stable stone diameter for bridge scour protection can be computed with the following formula (Jenssen & Tesaker, 2009):

$$D_{50} = K_f \cdot \frac{0.692 V_{local}^2}{2g(s-1)} \tag{2.7}$$

Here, $D_{50}\ (m)$ denotes the stone diameter bigger than the diameter of 50% of the mass of the sediment sample. $K_f\ (-)$ is a shape factor for the bridge piers equal to 2.3 for bridge piers with a pointy edge on the upstream side (Figure 5). $V_{local}\ (m/s)$ denotes the velocity located next to the upstream part of the bridge pier. V_{local} can be measured physically, retrieved from numerical models, or estimated as the product of the average velocity in the channel and a) a factor of 1 for piers located in a straight channel or an inner bend, or b) a factor of 1.7 for piers in an outer river bend. The specific gravity $s\ (-)$ is usually set to 2.6 (-).

2.1.4 Channel roughness

The roughness of the riverbed is a fundamental parameter in open-channel flow, affecting the flow resistance, water level and shear stress. Uniform flow occurs in a channel when every point in each streamlines has the same velocity vector. This is an ideal situation for understanding hydraulic principles, such as how channel roughness affects free surface flow. The Manning-Strickler equation is a popular equation for describing uniform flow:

$$Q = K_{st} \cdot A \cdot R_h^{\frac{2}{3}} \cdot I^{\frac{1}{2}} \tag{2.8}$$

$Q\ (m^3/s)$ denotes the discharge, $K_{st}\ (m^{\frac{1}{3}}/s)$ denotes the Manning-Strickler value, $A\ (m^2)$ denotes the cross-sectional area of the flow and $I\ (-)$ denotes the slope of the water surface. For steady uniform flow, the shear stress on the channel bed can be derived by solving the equilibrium of the shear force and the gravity component in the stream direction with respect to the shear stress:

$$\tau = \rho \cdot g \cdot h \cdot I \tag{2.9}$$

The water depth is denoted $h\ (m)$. The velocity along a vertical profile in a channel with uniform flow can be described by boundary layer theory. The following formula was proposed by Keulegan (1938):

$$\frac{U}{u_*} = 6.25 + 1/\kappa \cdot \ln\left(\frac{\mathrm{d}}{\mathrm{k_s}}\right) \tag{2.10}$$

$U\ (m/s)$ denotes the velocity in streamwise direction at a distance $d\ (m)$ from the channel bed and $\kappa\ (-)$ is the von Karman coefficient, equal to 0.4. Lastly, $k_s\ (m)$ denotes the sand-grain roughness. Normally, the sand-grain roughness is assumed to be proportional to d_x. $X\%$ of the mass of the sediments from a sample contains particles with a smaller diameter than the diameter $d_x\ (m)$. A literature review by Van Rijn (1982) suggests that the formula for k_s ranged from $k_s = 2.5 \cdot d_{90}$ to $k_s = 1.25 \cdot d_{35}$. It is worth noting that the formulas build on laboratory experiments, which all are made under different conditions. Thus, each formula is only valid under special circumstances. However, despite efforts to find a linear relationship between k_s and d_x, there does not exist a single formula valid for all conditions. Furthermore, the relationship between Manning-Strickler number and d_x is proposed as:

$$K_{St} = \frac{c}{d_x^{\frac{1}{6}}} \tag{2.11}$$

where c is an empirical factor. Because k_s is assumed to be proportional to d_x, k_s can substitute d_x in equation (2.11):

$$K_{st} = \frac{\beta}{k_s^{\frac{1}{6}}} \tag{2.12}$$

Here, $\beta\ (m^{0.5}/s)$ is an empirical factor. The US Army Corps of Engineers (2016) suggests $\beta = 29.24\ m^{0.5}/s$ for natural channels. Mayer-Peter and Müller (1948) suggest $\beta = 26\ m^{0.5}/s$.

2.1.5 Hydraulic jumps and river surf waves

Hydraulic jumps are formed in channels and rivers in the transition between an upstream supercritical flow and a downstream subcritical flow. Supercritical flow and subcritical flow are defined as flows with a Froude number higher and lower than 1, respectively. The squared Froude number is, in hydraulic engineering, the ratio of inertia to gravity. The equation for the dimensionless Froude number is:

$$F_r = \frac{u}{(gy)^{0.5}} \tag{2.13}$$

In this equation, $u\ (m/s)$ denotes the local velocity of water and $y\ (m)$ denotes the water depth. Hydraulic jumps are undular and not broken by white-water waves for upstream Froude number between 1 and 1.7, weak for upstream Froude number between 1.7 and 2.5, oscillating for upstream Froude number between 2.5 and 4.5, stable for upstream

Froude number between 4.5 and 9 and rough for upstream Froude numbers above 9 (Jesudhas, Balanchandar, & Murzyn, 2018).

Under special conditions, surfers and kayakers can surf on a standing wave in front of the hydraulic jump. Asiaban et al. (2021) designed an artificial surf wave on a flat riverbed with a ramp and a kicker. Figure 6 shows the ramp (number 1), which increases the upstream water depth and leads the water towards the kicker (number 2). The kicker aims at guiding the supercritical flow upwards to create a surfable supercritical wave. The point between the supercritical flow and the downstream subcritical flow is located downstream of the wave (number 3).

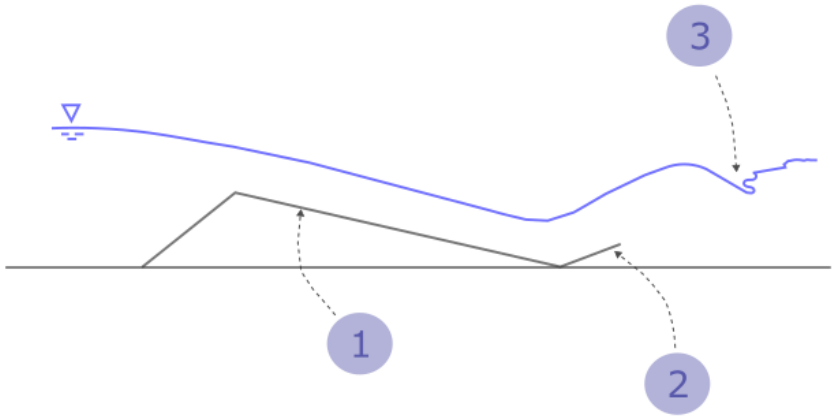

Figure 6: An artificial surf wave (after Figure 1 in Asiaban et al. (2021))

The surf wave in the Eisbach Canal in Munich is one of the most famous river surf waves. A plank is placed in front of the wave to guide the supercritical flow upwards (Geimer, 2014).

Figure 7: The surf wave in Eisbach Canal in Munich (photo by author).

2.1.1 Physical modelling

Physical modelling of hydraulics is an important tool for understanding and predicting the behaviour of fluids in real-world situations. To accurately model fluid flow, it is necessary to use scaling techniques to ensure that the physical properties of the model match those of the prototype.

To ensure that the physical model replicates the prototype, three laws of similitude should be fulfilled. The laws of similitude are geometric similitude, kinematic similitude, and dynamic similitude. Geometric similitude refers to the similarity of form between the model and the prototype, where the ratio of lengths in the model and prototype must be equal. Kinematic similitude refers to that the ratio of the velocity and acceleration between the model and the prototype must be equal. Finally, dynamic similitude is achieved when the ratios of forces in the model and the prototype are equal.

Physical models are created with a constant geometric scale to fulfil geometric similitude. The scale is decided by the wanted accuracy and the available resources, such as time, economic resources, and space. Furthermore, dynamic similitude is partly achieved by having the same ratio of the two dominant forces in the model and prototype (Briggs, 2013).

Froude scaling is applied in physical modelling where inertia and gravity are the dominant forces in the prototype. By maintaining the same Froude number (F_r) in the physical model and the prototype, the ratio of inertia and gravity becomes equal in the physical model and the prototype. Systems with free surface flow are usually scaled with Froude scaling. In hydraulic engineering, having the same Froude number in the prototype and model is achieved by scaling the discharge. The Froude scale factor for the discharge can be derived by solving the equation $F_{r_{model}} = F_{r_{prototype}}$ with respect to the discharge in the model ($L_{model}^3 T_{model}^{-1}$):

$$Q_{model} = \lambda^{5/2} \cdot \mathrm{Q}_{\mathrm{prototype}} \tag{2.14}$$

Furthermore, equation (2.14) can be solved with respect to the velocity in the model to show that kinematic similitude is achieved. However, full dynamic similitude cannot be achieved when only two forces have the same ratio in the model and prototype. Scale effects are introduced because not all the laws of similitude can be satisfied when scaling free-surface flow.

For example, Reynolds number describes the ratio of inertial forces to viscous forces and is a measure of weather the flow is turbulent or laminar. Reynolds number for open-channel flow is approximately $u \cdot y/\nu$, when $y \gg b$, where $\nu = 10^{-6}\frac{m^2}{s}$ denotes the kinematic viscosity of water at 20 degrees Celsius. If the physical model is scaled using Froude scaling, the Reynolds number cannot be the same in the model and prototype unless the geometric scale is 1:1. Thus, the effect of the viscous force is different in the model than in the prototype. To minimize this scaling error, it is recommended to have a sufficiently high Reynolds number. In a review article on two-phase flow with focus air concentration, Pfister and Chanson (2014) propose a minimum Reynold number above $2 \cdot 10^5$.

The Weber number describes the ratio of the inertial forces to the surface tension forces. Although it is not used for scaling large-scale hydraulic systems, it does provide a minimum criterion for physical models: to avoid significant surface tension in the model, it is preferable to maintain a depth of at least 2 cm (Lia & Havrevoll, 2021). A visible effect of the lack of dynamic similitude is that physical models usually underestimate the air-entrainment compared to the prototype due to a relative overestimation of viscosity and surface tension (Pfister & Chanson, 2014).

2.2 Computational fluid dynamics

2.2.1 Software

CFD software is used to simulate and analyze the behaviour of fluids in a variety of applications. There are several three-dimensional CFD software suitable for river hydraulics, such as REEF3D, Ansys Fluent, Delft 3D, Flow-3D, STAR-CCM+, SSIIM and OpenFOAM. The open-source software OpenFOAM is applied in this thesis. OpenFOAM can generally produce results of comparable accuracy with similar computational cost compared to commercial software (Olsen, 2015).

2.2.1 Reynolds-Averaged Navier-Stokes (RANS) equations

CFD software aim at solving the Navier-Stokes equations: the continuity equation (equation (2.15)) and the momentum equation (equation (2.16)). The momentum equation is an extended form of Newton's second law, while the continuity equation conserves mass. The Navier-Stokes equations are derived from the force balance of laminar flow.

$$\frac{\partial \mathrm{u_i}}{\partial \mathrm{x_i}} = 0 \qquad | \, i = 1,2,3 \tag{2.15}$$

$$\frac{\partial \mathrm{u_i}}{\partial \mathrm{t}} + u_j \frac{\partial \mathrm{u_i}}{\partial \mathrm{x_j}} = -\frac{1}{\rho}\frac{\partial p}{\partial \mathrm{x_i}} + \frac{\partial}{\partial \mathrm{x}} \nu \left(\frac{\partial u_i}{\partial \mathrm{xj}} + \frac{\partial \mathrm{u_j}}{\partial \mathrm{xi}} \right) + f_i \qquad | \, i,j = 1,2,3 \tag{2.16}$$

In equation (2.15), $\mathrm{u_i}$ $\left(\frac{m}{s}\right)$ denotes the velocity component in the direction $\mathrm{x_i}$. In equation (2.16), ρ $\left(\frac{kg}{m^3}\right)$ denotes the density of the fluid, $\mathrm{t}\,(s)$ denotes the time, $\mathrm{p}\,(\mathrm{kg}\cdot\mathrm{m}^{-3})$ denotes the pressure, ν $\left(\frac{m^2}{s}\right)$ denotes the kinematic viscosity and f $(\frac{m}{s^{-2}})$ is and external force, such as gravity.

The RANS equation is popular due to the computationally low cost. The RANS equation solves Navier-Stokes equations by applying time-averaging of the velocities. The velocity at time t, $u(t)$, is the sum of a time-averaged velocity, $\bar{u}$, and a fluctuating component, u':

$$u(t) = \bar{u} + u' \tag{2.17}$$

The mean of the fluctuating velocity component is assumed to be zero over a sufficiently long time:

$$\overline{u'} = 0 \tag{2.18}$$

Substituting equation (2.18) into equation (2.17) gives:

$$\bar{u}_i(t) = \bar{u} \tag{2.19}$$

However, for the non-linear term $u_j \frac{\partial \mathrm{u_i}}{\partial \mathrm{x_j}}$, the fluctuating velocity component cannot be averaged to zero:

$$\overline{u_j(t)u_\iota(t)} = \bar{u}_j(t)\bar{u}_i(t) + \overline{u_j' u_i'} \tag{2.20}$$

Substituting equation (2.19) into the continuity equation (equation (2.15)) yields:

$$\frac{\partial \bar{u}_i}{\partial \mathrm{x_i}} = 0 \qquad | \, i = 1,2,3 \tag{2.21}$$

And substituting equation (2.19) and equation (2.20) into the momentum equation (equation (2.16)) gives:

$$\frac{\partial \bar{u}_i}{\partial \mathrm{t}} + \bar{u}_j \frac{\partial \bar{u}_i}{\partial \mathrm{x_j}} = -\frac{1}{\rho}\frac{\partial \bar{p}}{\partial \mathrm{x_i}} + \frac{\partial}{\partial \mathrm{x}}\left(\nu\left(\frac{\partial \bar{u}_i}{\partial \mathrm{xj}} + \frac{\partial \bar{u}_j}{\partial \mathrm{xi}}\right) - \overline{u_j' u_i'}\right) + \bar{f}_i \qquad | \, i,j = 1,2,3 \tag{2.22}$$

The extra term $\overline{u_j' u_i'}$ yields the components of the Reynolds stress tensor. Because the indexes i and j both refer to three dimensions, six more terms must be solved. There are no velocity fluctuations in laminar flow and $\overline{u_j' u_i'}$ is zero, but fluctuations appear for turbulent flow. Thus, turbulence models must be introduced to close the RANS equations (equation (2.22) and equation (2.21)) for turbulent flow.

The Boussinesq approximation relates Reynolds stress to the turbulent eddy viscosity. The $k-\epsilon$-model solves an isotropic turbulent eddy viscosity using two partial differential equations for the turbulent kinetic energy, $k\ (m^2/s^2)$, and the turbulent energy dissipation rate, $\epsilon\ (m^2/s^3)$. The turbulent kinetic energy is by definition:

$$k = 0.5 \cdot (\overline{u'^2}_1 + \overline{u'^2}_2 + \overline{u'^2}_3) \tag{2.23}$$

2.2.1 Volume of Fluid (VOF) method

The VOF method is a numerical method for solving the free surface between two phases. To determine the location of the interface, an additional continuity equation for $\alpha\ (-)$ is solved:

$$\frac{\partial \alpha}{\partial t} + \mathrm{u_j}\frac{\partial \alpha}{\partial \mathrm{x_j}} = 0 \qquad | \, i = 1,2,3 \tag{2.24}$$

The principle is to model a mixture of two fluids in each cell. The α fraction varies from 1 if the cell is filled with one phase, to 0 if the cell only contains the second phase. The interphase is located at the surface where $\alpha = 0.5$. The VOF method produces a diffuse interphase, smeared out for increasing cell sizes. Equation (2.24) can be interpreted as a conservation of the volume fraction of water to air along a streamline.

2.2.2 Courant number

The Courant-Friedrichs-Lewy (CFL) condition states that the Courant number $C\ (-)$ must be less than a maximum value. The CFL condition has the form:

$$C = \frac{\mathrm{u}\cdot\Delta t}{\Delta x} \leq C_{max} \tag{2.25}$$

Here, u denotes the velocity in each cell, $\Delta t\ (s)$ denotes the time step, $\Delta x\ (m)$ denotes the cell length and $C_{max}\ (-)$ denotes the maximum value of the courant number. The Courant number is a measure of the stability of the numerical scheme. The value of C_{max} depends on the applied numerical scheme. For all stable explicit schemes, C_{max} is limited. On the other hand, more implicit schemes are more stable than explicit schemes and can utilize a greater Courant number. Lower values of the Courant number yield better stability but increase the computational time. Higher values will also reduce the accuracy in the temporal domain (Hellevik, 2020).

2.2.3 Height of cells closest to walls

In CFD modelling, there are requirements for the distance between cell centres closest to a wall and the wall. In the following, two such requirements will be presented. One of these

requirements depends on the dimensionless wall distance. The dimensionless wall distance $y^+ (-)$ is defined as:

$$y^+ = \frac{u_\tau \cdot y}{\nu} \tag{2.26}$$

Here, $u_\tau \, (m/s)$ denotes the shear velocity at the wall, and $y \, (m)$ denotes the distance from the wall to point of interest. Furthermore, the dimensionless velocity $u^+ (-)$ is defined as:

$$u^+ = u/u_\tau \tag{2.27}$$

The concept of y^+ predicts the location of the viscous sublayer, the buffer sublayer, and the log-law sublayer in a turbulent boundary layer. A y^+-value between 0 and 5 predicts the location of the viscous sublayer. The viscous sublayer is a region of the flow where the viscous forces are dominant, and the dimensionless velocity and the dimensionless wall distance are equal. This sublayer is located adjacent to a solid surface in a fluid flow.

A y^+-value between 5 and 30 predicts the location of the buffer layer. This layer describes a transitional flow regime where the flow goes from the viscous sublayer to the log-law layer. A y^+-value between 30 and 500 predicts the location of the log-law layer. Both turbulent forces and viscous forces are important in the log-law layer, and the relation between the dimensionless velocity and the dimensionless distance from the wall is logarithmic. A y^+-value above 500 predicts the location of the outer layer where inertial forces are dominant (Versteeg & Malasekera, 2007).

In the log-law layer, wall functions are developed to describe the universal nature of boundary layers to find the velocity in the cell centre closest to a wall. Proper use of wall functions in CFD requires the first cell centre to be located within the log-law layer. Therefore, y^+ should be between 30 and 500 in cell centres closest to walls. However, wall functions have also been used for higher y^+-values. Hoff et al. (2010) apply y^+-values between $1.5 \cdot 10^4$ to $2 \cdot 10^4$.

Another requirement is related to the sand-grain roughness, k_s, if a boundary condition with the sand-grain roughness is applied. Blocken et al. (2007) suggest that it is physical meaningful to have a distance from the wall to the first cell centre greater than k_s. Fluent 6.1 User's Guide (Fluent Inc., 2003) stresses that the centre of the cell closest to the wall should be greater than k_s for best result. This requirement has been removed in later versions of Fluent (ANSYS Inc., 2013). To the author's knowledge, there is no information available on whether this requirement also has been removed in OpenFOAM.

2.2.4 Errors in numerical modelling

There are multiple error sources in numerical modeling. ERCOFTAC (2000) proposes Best Practice Guidelines for CFD, and lists the following sources of error:

1. Modelling errors occur when the real physical systems are modelled with mathematical equations. For example, the popular Reynolds-averaged Navier-Stokes (RANS) equations use a time-averaged velocity to solve Navier-Stokes equations. This abstraction of reality cannot fully capture the unsteady and fluctuating nature of turbulent flow (Bensow, Fureby, & Liefvendahl, 2006).
2. Numerical approximation errors occur when mathematical differential equations are discretized. In CFD, this discretization will never be completely correct. One numerical approximation error is false diffusion. False diffusion causes sharp gradients to be smeared out and is caused by an inaccurate discretization of convective terms. It is necessary to interpolate the values from the centre of the

cells to the walls between the cells in numerical modelling and this interpolation causes diffusion. False diffusion can be reduced by (1) aligning the axis of the hexahedral grid to the flow direction, (2) using a finer mesh and (3) applying higher-order schemes. The industry standard is to use grid independency analysis to ensure that the mesh is refined enough (Olsen, 2017).

3. Errors due to wrong boundary conditions and input data. Real-world system boundaries are often highly complex, and describing these boundaries with boundary conditions and input data can lead to errors. For example, a bathymetric survey of a river might not capture the correct bathymetry.
4. A lack of knowledge of how to conduct a CFD analysis can lead to errors.
5. Software code can contain mistakes and bugs, leading to errors in numerical simulation.
6. Convergence errors can occur if the simulation has not converged properly. Multiphase flow is solved with iterative solvers, and these iterations must converge in each time step. In addition, the quantity of interest, such as the water level, must converge for steady-state investigations of transient simulations.

2.2.1 Numerical roughness

The numerical roughness does not necessarily follow the empirical formulas proposed in equation (2.12). Chen et al. (2021) modelled a 30 km long river reach with both interFoam and the hydraulic software MASS2. Both models were calibrated against water level measurements by varying k_s and the Manning-Strickler value, respectively. By back-calculations, it was found a reasonable relation between the Manning-Strickler value and the sand-grain roughness:

$$K_{St} = \frac{21.6}{k_s^{\frac{1}{6}}} \tag{2.28}$$

Other studies utilize experimental equations to relate the Manning-Strickler value to k_s. Almeland et al. (2018) sets $k_s = 0.0017$ based on a table Manning-Strickler value for cement-lined channels ($K_{St} = 90$), in an OpenFOAM simulation. This corresponds to:

$$K_{St} = \frac{31.1}{k_s^{\frac{1}{6}}} \tag{2.29}$$

Richter et al. (2021) used $k_s = 0.3\ m$ to simulate unlined rock with a Manning-Strickler value of 32 $m^{\frac{1}{3}}/s$ in Ansys Fluent. This corresponds to:

$$K_{St} = \frac{26.2}{k_s^{\frac{1}{6}}} \tag{2.30}$$

2.3 Numerical modelling of scour

This chapter presents numerical scour models. Zhao (2022) categories the current CFD scour models into sediment transport rate models including equilibrium scour models, CFD-DEM models, and two-phase models. The following sections will describe each scour model.

2.3.1 Sediment transport rate models

Sediment transport rate models are one-phased models. The Navier-Stokes equation is resolved for the flow field, and the solution of the flow field decides the scour rate. This

scour rate is typically computed with empirical formulas. Usually, Reynolds-Averaged Navier-Stokes equations (RANS) are used due to their high computational efficiency.

First, the flow field is simulated. Thereafter, the shear stress on the riverbed is computed. Scour will take place if the flow-induced dimensionless shear stress is higher than the dimensionless critical shear stress (equation (2.1)) at a specific point. The shear stress on the bed can be calculated as:

$$\tau_k = C \cdot \rho_w \cdot k \,. \tag{2.31}$$

C is equal to 0.3 (Baranaya, Olsen, & Sturm, 2014), ρ_w denotes the density of water and k is the turbulent kinetic energy.

The dimensionless critical shear stress can be calculated in several ways (Soulsby, 1997). Some formulas use the velocity near the bed to compute the dimensionless critical shear stress, while others use a constant critical dimensionless shear stress: Rüther et al. (2005) uses a dimensionless critical shear stress value of 0.047. Next, a reduction of the critical shear stress on an arbitrary sloped bed can be considered: Bihs and Olsen (2011) use the bed slope correction of the critical shear stress formula of Dey (2001) (equation (2.3)) with the angle of repose being $\mu = 35$ degrees for uphill slopes and $\mu = 45$ degrees for downhill slopes. Furthermore, the numerical studies utilize empirical formulas to relate the non-dimensional shear stress and non-dimensional critical shear stress to the bed transport rate:

$$q_{bed\ load} = f(\theta, \theta_{cr}) \,. \tag{2.32}$$

Several formulations of the bed load transport rate formula exist (Table 1).

Table 1: Sources of formula in the form of equation (2.32) and the implementation.

Source of bed load formula in the form of equation (2.32)	**Source of numerical scour study where this formula is implemented**
(Roulund, Sumer, Fredsøe, & Michaelsen, 2005)	(Kim, Chen, & Briaud, 2020)
(Van Rijn, 1987)	(Ahmad, Bihs, Myrhaug, Kamath, & Arntsen, 2020)
(Engelund & Fredsoe, 1976)	(Zhao, Cheng, & Zang, 2010)
(Meyer-Peter & Müller, 1948)	(Jalal & Hassan, 2020)

Suspended sediments are often modeled by solving the convection-diffusion equation. Some studies leave out the suspended load for clear-water scour. After the bed load and/or the suspended load are modeled, the bed profile is updated based on the scour and sedimentation. In addition, sand-slide models can be included to limit the slope angle. After the bed profile is updated, a new flow field can be computed, and the iterative procedure continues. Finally, the scour hole reaches equilibrium, and a maximum scour depth can be retrieved.

2.3.2 Two-phased models

Two-phased models simulate the sediments as a separate phase. The interphase between the water phase and sediment phase is not sharp, but the phase changes gradually from fluid to sediment. In these Eulerian-Eulerian models, the momentum and continuity equations are solved for both phases. In the OpenFOAM toolbox, SedFOAM is one such

model. SedFOAM has shown a good performance of scour modeling for simple geometries (Cheng, Hsu, & Calantoni, 2017).

There are a few advantages of two-phase models compared to one-phase models. The interphase between the fluid and sediment phase allows for a potentially better representation of the sediment-water slurry close to the riverbed, also known as the sheet flow. In addition, the bed is implicitly modelled in two-phase models, in contrast to one-phase models, which need several algorithms to update the riverbed, such as the empirical sand-slide algorithms.

On the other hand, the computational cost increases because an extra phase must be modeled. Two-phase models have not been used on complex cases, as compared to one-phase models, due to their higher computational costs (Zhao, 2022). Lastly, the behaviour of the sediment-water mixture needs further research, and treating this slurry as two phases might not be optimal (Song, Xu, & Liu, 2022).

2.3.3 CFD-DEM models

CFD-DEM models are Eulerian-Lagrangian models. Discrete Element Method (DEM) is used to model sediments, while CFD is used to model the fluid phase. DEM simulates the movement of each particle based on Newton's second law (Sun & Xiao, 2016). SediFOAM is a CFD-DEM model belonging to the OpenFOAM software (Sun & Xiao, 2016).

CFD-DEM models can simulate particle-particle interaction, particle-flow interaction, and flow-particle interaction. However, the computational cost is much higher than sediment transport models because each sediment particle is modeled. Thus, CFD-DEM has only been used for small-scale problems (Zhao, 2022).

2.3.4 Equilibrium scour models

Equilibrium scour models aim at finding the equilibrium scour depths, but do not provide information about the history of the scour development. These models utilize optimization algorithms: The bed profile is iteratively altered to minimize an objective function.

Like sediment transport models, the flow field is first simulated with CFD, before the non-dimensional shear stress and the non-dimensional critical shear stress on the bed are calculated. Equilibrium scour models can also include bed slope corrections and sand-slide algorithms. The objective function can be formulated in different ways, but Pang et al. (2016) propose:

$$X_{Objective} = abs(\theta - \theta_{cr}) \, . \tag{2.33}$$

Here, $X_{Objective}$ denotes the objective function. The riverbed is updated to minimize this objective function in every bed cell. If the objective function is reduced, a new simulation of the flow field is carried out with the new bed profile. The simulation ends if the objective function reaches a predefined limit.

The advantage of equilibrium scour models is the computationally low cost compared with sediment transport models (Zhao, 2022). Mandviwalla et al. (2020) developed a 2-dimensional equilibrium scour model for bed load using OpenFOAM. However, this model is to the author's knowledge not made publicly available and there are no other publicly available equilibrium scour models for OpenFOAM.

2.4 InterFoam

There are multiple methods for handling the free surface in CFD. One approach is to use the rigid lid approximation using a single phase. In OpenFOAM, the solver pimpleFoam can simulate flow with the rigid lid approximation. This approximation ignores free surface deformations. However, the method is only suitable for flows with a Froude number lower than 0.8 (Constantinescu & Koken, 2011). Cho et al. (2022) showed that the Reynolds shear stress is decreased in 30% of the flow depth beneath the rigid lid. The multiphase solver interFoam is chosen because modelling a correct shear stress is desirable and the Froude number is assumed to be high downstream of the piers. InterFoam models the free surface with the VOF method.

2.4.1 Discretization schemes

The different terms in the momentum and continuity equations are discretized using discretization schemes. In OpenFOAM, the schemes are found in *0/*fvSchemes. The schemes applied in this thesis are described in the following.

Transient schemes:

- *Euler* is a first-order implicit scheme used for transient terms (OpenFOAM Foundation Ltd, 2022).

Gradient schemes:

- *Gauss linear* is second-order accurate and unbound.
- *cellMDLimited Gauss linear 1* can be used for grad(U) in case of poor-quality mesh. The scheme offers stability but is dissipative. However, the scheme is more unstable and less dissipative than *cellLimited Gauss linear 1*. The coefficient 1 stands for boundedness and is the only used option. The cellLimited schemes provide stability by limiting the gradients so the extrapolated values at the cell walls are not outside the constrictions of surrounding cells (OpenFOAM Foundation Ltd, 2022).

Divergence schemes:

- *Gauss linearUpwind grad(U)* is a second-order unbound scheme.
- *Gauss vanLeer* is a second-order accurate and unbound divergence scheme. The scheme is less unbound than *limitedLinear*.
- *Gauss linear* is second-order accurate and unbound.
- *Gauss upwind* is first-order accurate and bounded.

Laplacian schemes:

- *Gauss linear corrected* is a second-order accurate Laplacian scheme with a correction of the gradients. An alternative scheme is Gauss linear limited with the entry 0 to 1, which can be used for poorer mesh-quality.

Interpolation schemes:

- *Linear* is a scheme used for the interpolation of values from the centre of a cell wall to the centre of another cell. *Linear* is the most used scheme for interpolation.

Surface-normal gradient schemes:

- *corrected* can be used as a surface-normal gradient scheme. The scheme uses central-differencing and corrects for non-orthogonality (OpenFOAM Foundation Ltd, 2022).

2.4.2 Settings for the solution algorithms

The solver algorithms can be modified with settings in the directory *0/fvSolution*. The settings are described in the following:

- *MulesCorr* determines if the semi-implicit MULES (Multidimensional Universal Limiter for Explicit Solution) or the explicit MULES is utilized. The semi-implicit version of MULES can utilize a higher Courant number and is supposed to be faster than its explicit counterpart (The OpenFOAM Foundation Ltd, 2014).
- *nLimiterIter* is the number of MULES iterations. The recommended value is 3-5 for Courant numbers less than 3 and 5-10 for higher Courant numbers (Wolf Dynamics, 2014).
- *nAlphaCorr* controls the number of times the α-equation is solved in one timestep. This improves the quality of the solution by fixed point iteration. A value of two means that the α-equation is solved once and this solution is used in the computation of the second and final solution of α (OpenFOAM Foundation Ltd, 2022). A value of two or higher is suitable for simulations with high Courant numbers (Wolf Dynamics, 2014).
- The parameter *nAlphaSubCycles* determines the number of subcycles within a timestep. The α-equation is solved for each subcycle and the maximum Courant number at the interface within each subcycle is the maximum Courant number at the interface, *maxAlphaCo*, divided by *nAlphaSubCycles*. This provides stability to the numerical scheme without excessive computational costs. The solution time can be vastly decreased by increasing the global Courant number, *maxAlphaCo,* and *nAlphaSubCycles* (CFD Direct, 2018).
- *cAlpha* determines the compression of the interface. The most used value is 1 (Wolf Dynamics, 2014).
- *alphaApplyPrevCorr* determines if the last time step should be used as an initial estimate or not. The last time step should be used as an initial estimate for slowly varying flows (Wolf Dynamics, 2014).
- *solver* specifies the linear solver used for numerically solving the discretized equation at hand. The solver *smoothSolver* uses a *smoother* to solve the discretized equation. The *solver PCG* (Preconditioned Conjugate Gradient) is a solver for the pressure equation. The alternative, the GAMG solver, is faster for a few processors. *GAMG* (geometric-algebraic multi-grid) is a *solver* which generates a preliminary solution on a coarser mesh and transfers the solution to a finer mesh.
- A *smoother* is an operation applied to a system of linear equations before the solution process starts to increase convergence and reduce discretization errors. The smoother *symGaussSeidel* uses the symmetric Gauss-Seidel method. DICGaussSeidel is another variant of the Gauss-Seidel method.
- *nPreSweeps* is the number of sweeps as the mesh becomes coarser in the *GAMG* algorithm. Sweeps refer to the number of smoothing iterations in each solver iteration (SimFlow, 2017).
- *nPostSweeps* is the number of sweeps as the mesh becomes refined (OpenFOAM Foundation Ltd, 2022).

- *Preconditioners* are used to improve the convergence of iterative solution algorithms for linear systems of equations (Xi, 2005). The preconditioner *DIC* (Simplified Diagonal-based Incomplete Cholesky preconditioner) utilize incomplete Cholesky factorization (OpenFOAM Foundation Ltd, 2022).
- The solution algorithm stops if either the *tolerance*-, the *relTol*- or the *max Iter* criterion is achieved. The *tolerance* criterion is achieved if the residual is lower than a user-specified value. The *relTol* criterion is achieved if the ratio of the last residual to the first residual is below a user-specified value. The *maxIter* criterion is achieved if the number of iterations reaches a user-specified value. Furthermore, stricter convergence criteria can be specified for the final iteration under *<name of field>Final* (OpenFOAM Foundation Ltd, 2022).
- *momentumPredictor* controls the solving of the momentum predictor and is usually turned off for multiphase flow (OpenFOAM Foundation Ltd, 2022).
- *nCorrectors* determines the number of times the pressure equation and momentum corrector are solved in the PISO and PIMPLE algorithms. The value of *correctors* is usually 2-3 (OpenFOAM Foundation Ltd, 2022).
- *nOuterCorrectors* controls the number of outer correctors in the PIMPLE-algorithm. The PISO-version of the PIMPLE algorithm uses 1 outer corrector. Higher values can be considered for large Courant numbers (Wolf Dynamics, 2014).
- *nNonOrthogonalCorrector*s is used by both PISO and PIMPLE. The parameter determines the number of non-orthogonal corrections in the solution of the pressure equation (OpenFOAM Foundation Ltd, 2022). It is recommended to use at least 1. Higher values can be considered for highly non-orthogonal meshes (Wolf Dynamics, 2014).
- *Relaxation factors* control the under-relaxation of the solution algorithm. Under-relaxation increases stability but is not recommended for highly transient problems (OpenFOAM Foundation Ltd, 2022).

2.4.3 Boundary conditions

The boundary conditions are specified in the field directories in the *0* directory. The fields are *U*, *alpha.water*, *nut*, *k*, *epsilon,* and *p_rgh*. *U* denotes the velocity, *alpha.water* is the α-fraction, *nut* is the turbulent viscosity, *k* is the turbulent kinetic energy, *epsilon* is the turbulent kinetic energy dissipation rate and *p_rgh* is an alternative pressure. To understand the implementation of the boundary conditions of the pressure in this thesis, a brief explanation of the alternative pressure is given. The alternative pressure is defined as (OpenCDF Ltd, 2018):

$$p\_rgh = p - \rho gh \tag{2.34}$$

The numerical implementation is defined in *createFluidFields.H* on line 103 (OpenFOAM Foundation Ltd, 2021):

```
Line 86     p_rgh = p - rho*gh
```

Here, `rho` is the density of the fluid phase, `p` is the pressure and `gh` is defined in file *gh.H* (OpenFOAM Foundation Ltd, 2021):

```
Line 1     Info<< "Calculating field g.h\n" << endl;

Line 2      dimensionedScalar ghRef(- mag(g)*hRef);

Line 3      volScalarField gh("gh", (g & mesh.C()) - ghRef);
```

Here, `mesh.C()` is the coordinate of the centre of the cell, `&` denotes the inner product, `g` denotes the acceleration of gravity and `hRef` is the reference elevation. The default value is zero. Thus, `ghRef` is the negative product of the absolute value of the acceleration of gravity and the reference elevation. The parameter `gh` is the inner product of the acceleration of gravity and the coordinate of the evaluated cell center minus `ghRef`.

For example, if the acceleration of gravity is equal to -9.81 m/s^2, `hRef` is 0, the elevation of `mesh.C()` is an arbitrary positive value, z, and `rho` is equal to 1000 kg/m^3, `gh` becomes $-9.81 \cdot z$ according to line 2 and 3. Substituting `gh` into line 86 in *createFluidFields.H* gives `p_rgh = p - 1000*9.81*z`. This shows that when the pressure is zero, the term p_rgh is equal to $1000 \cdot 9.81 \cdot z$. Thus, a constant water level at elevation z can be determined on a boundary by setting p_rgh equal to $1000 \cdot 9.81 \cdot z$.

There are (at least) two methods of applying a boundary condition with a constant outlet water depth below an air phase using a fixed pressure at the outlet. The first method is to create two patches at the outlet boundary. The outlet boundary condition for p_rgh in the air patch can be set equal to 0 and equal to $1000 \cdot 9.81 \cdot z$ in the water patch. The second method is to change the reference elevation `hRef` to the desired water level elevation. This is done by adding a *hRef* file to the *constant* directory. The outlet boundary can contain one patch where the p_rgh is equal to 0.

Using a pressure boundary condition at the outlet and a velocity boundary condition at the inlet is a well-defined combination. OpenCFD Ltd (2016) states that specifying the discharge at the inlet using *variableHeightFlowRateInletVelocity* and a fixed value for `p_rgh` at the outlet using *fixedValue* provides excellent stability. However, Thorenz and Strybny (2012) report that the results of interFoam simulations with constant water depth are dependent on the distance from the origin if a fixed value for `p_rgh` is used with two patches as described above. Thorenz and Strybny (2012) argue that the change in the term `rho*gh` at the interface is greater for greater values of `h`, and thus, the pressure gradient at the interphase increases and becomes harder to solve numerically. Teuber et al. (2019) use a constant value for `p_rgh` at the water phase equal to $1000 \cdot 9.81 \cdot z$ and constant value equal to 0 in the air phase (as described above), while Thorenz and Strybny (2012) chose to prescribe a boundary condition for the pressure `p`, including both the hydrostatic pressure and the dynamic pressure contribution using the functionality of OpenFOAM-1.6. The boundary conditions applied in this thesis are briefly explained in the following:

- *zeroGradient* is a Neumann boundary condition where the gradient is set to 0.
- *variableHeightFlowRateInletVelocity* is a boundary condition for the velocity at the inlet. The discharge can be specified, while the water level is varying according to the discharge and downstream conditions.
- *fixedFluxPressure* is a Neumann boundary condition for the pressure. This boundary condition adjusts the pressure gradient according to the velocity boundary condition.
- *variableHeightFlowRate* is a mixed boundary condition where the α-fraction is constrained by a maximum and minimum value. The gradient of α is zero between these two values. However, if α is either lower than the minimum value or larger than the maximum value, α is set to a fixed value equal to the minimum or maximum value, respectively.

- *fixedValue* is a Dirichlet boundary condition. A constant boundary value must be specified.
- *calculated* is a boundary condition where the field where this boundary condition is applied, is decided by the other fields and turbulence properties.
- *totalPressure* is a boundary condition for the pressure at the boundary open to the atmosphere. The static pressure on the boundary is calculated based on a user-specified total pressure.
- *noSlip* is a Dirichlet boundary condition for the velocity at boundaries near solid surfaces. The velocity value is set to zero at the boundary.
- *pressureInletOutletVelocity* is a mixed boundary condition for the velocity where the outflow velocity is determined by a Neumann condition with the gradient being zero and the inflow velocity is a Dirichlet boundary determined by the pressure. This boundary condition is often used together with the *totalPressure* boundary condition.
- *epsilonWallFunction* is a Dirichlet boundary condition for the turbulent energy dissipation near a solid surface. The formula for the turbulent energy dissipation depends on the y^+ value.
- *kqRWallfunction* is a Neumann boundary condition for the turbulent kinetic energy near a solid surface. The *kqRWallfunction* has similarities to the *zeroGradient* boundary condition.
- *nutkRoughWallFunction* is a boundary condition for the turbulent viscosity near a rough solid surface. The user-specified sand-grain roughness, k_s, and the user-specified roughness constant C_s determines the roughness of the wall. The roughness constant is typically equal to 0.5. The formula of the turbulent viscosity depends on the sand-grain roughness in wall units, $k_s{}^+$ and the y^+-value.
- *empty* is a boundary condition used for the sides in two-dimensional cases.

2.4.4 Initial conditions

The initial water level can be specified in the directory setFieldsDict. This directory can create a horizontal water level using *boxToCell*, or an inclined water level using *rotatedBoxToCell*. Furthermore, a coarse case can be used as the initial condition for a finer case with the utility *mapFields*.

The initial condition of the other fields inside the mesh is set in their respective directories located in the 0-directory after the keyword *internalField*. On the boundaries, the initial condition is specified after the keyword *value.*

2.4.1 Shear stress in interFoam

The utility *wallShearStress* is a built-in calculation of the shear stress next to a solid surface. The shear stress, τ_R (m^2/s^2), is calculated as the inner product between the shear stress symmetric tensor, R (m^2/s^2), and the normal vector to the cell wall, $\boldsymbol{n}$ (-):

$$\tau_R = R \cdot n \tag{2.35}$$

The unit of the shear stress is given in m^2/s^2 and the utility *wallShearStress* must be multiplied by the density of the water to retrieve the shear stress at the riverbed in Pa. The turbulent kinetic energy is also used as a measure of the bed shear stress (equation (2.31)). The turbulent kinetic energy can be extracted from the cell centres closest to the riverbed using post-processing tools.

2.4.1 ParaView

ParaView (Kitware, Inc., 2023) is a widely used open-source software tool for data visualization and provides a user-friendly graphical interface for computational simulations. The software is downloaded together with OpenFOAM unless specified otherwise. ParaView also supports python macros, which enables the user to automate repetitive post-processing tasks. Macros can be generated by tracing clicks in the graphical interface. Afterwards, the user can make changes to the code.

3 Method

3.1 Material

3.1.1 Hydraulic data

A discharge gauge is located approximately 2 km upstream of Sluppen bridge (Figure 1). The gauge has records of discharge data since 1881 as shown in Figure 8.

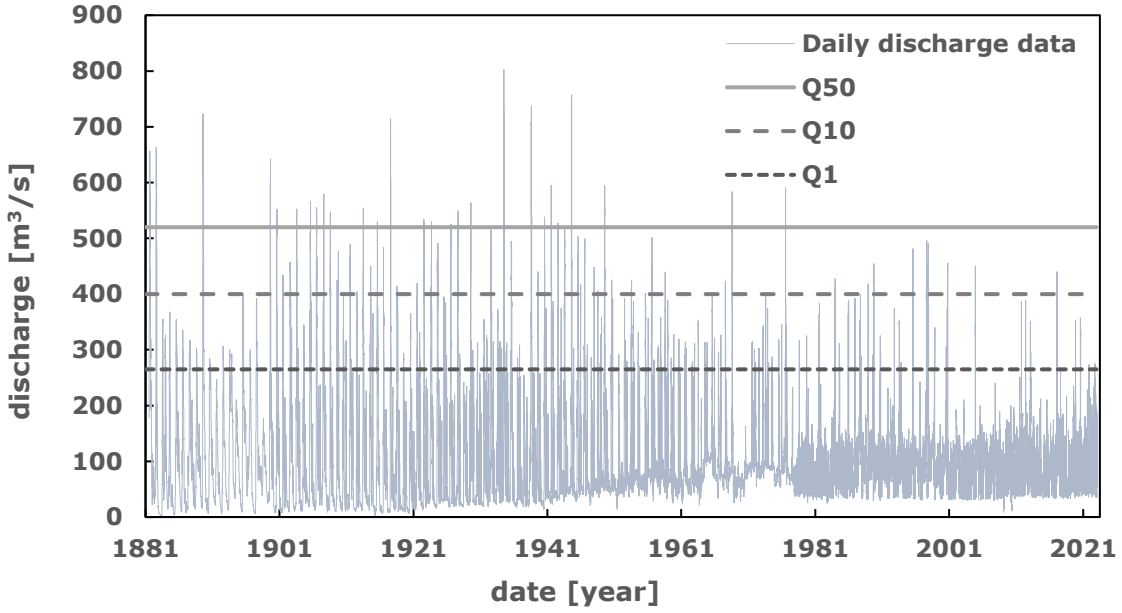

Figure 8: Discharge data from gauge located 2 km upstream of Sluppen bridge.

The return intervals for selected years are listed in Table 2 (The Norwegian Water Resources and Energy Directory, 2023). It must be stressed that the effect of regulation by the upstream hydroelectric power plants is not considered.

Table 2: Flood discharges with return intervals.

Return interval (year)	Discharge (m^3/s)
1	265
10	400
50	520

The results of a one-dimensional HEC-RAS model were provided by NTNU. The bathymetry used in this HEC-RAS model is shown in Appendix 1. The water level downstream of the bridge is used as input to the interFoam simulation. Table 3 shows the water level downstream of the bridge for a given discharge in HEC-RAS. The downstream water levels are extracted at the location of the outlet boundary in the interFoam simulation.

Table 3: Discharge and downstream water level from HEC-RAS simulation.

Discharge (m^3/s)	Downstream water elevation (m)
85	4.8
135	5.1
400	6.4

3.1.2 Bathymetry

The Norwegian Public Roads Administration provided drawings of the piers from 1976 (Appendix 2). To determine the location and the angle of the piers, the Norwegian University of Science and Technology (NTNU) measured the location of the piers on each side of the bridge. The location of the piers relative to the river is shown in Appendix 3.

SWECO performed a bathymetric survey near the Sluppen bridge piers on December 15, 2022. The digital elevation model (DEM) and the location of the piers are shown in Appendix 4. A Surveyor M9 (an Acoustic Doppler Current Profiler (ADCP) system) and the software HydroSurveyor were used to measure the bathymetry. The measured points are shown in Appendix 5. This bathymetry does not cover the riverbanks. However, NTNU provided a DEM of Nidelva covering both riverbanks and the downstream riverbed (Appendix 1). This DEM is created by a combination of Surveyor M9 and LiDAR measurements but has a coarser resolution than the measurement data from SWECO.

3.1.3 Computational resources

The simulations run on a remote computer located at the Norwegian University of Science and Technology in Norway. This computer has 40 Intel® Xeon® Gold 5218R 2.1 GHz processors. All simulations in this study are run in parallel with 39 processors.

3.2 Scour model

The method proposed in the following is inspired by the sediment transport rate models and equilibrium scour depth models. Contraction scour under real bridges is a large-scale phenomenon. Thus, it is emphasized to reduce the computational cost and simplify the modelling.

From a safety point of view, one can argue that any scour close to the bridge pier is unacceptable. Thus, it is crucial to find out *if* scour will take place. This will make any computational methods which include sediment sizes highly uncertain. Established scour models usually aim at finding the maximum scour depth or the riverbed profile at equilibrium. These models normally utilize information about the sediment properties and aim at finding a maximum scour depth for transient simulations. Unfortunately, there are no samples of the in-situ riverbed sediments near the Sluppen bridge. Instead, the scour model in this study estimates a critical sediment diameter at the riverbed for a steady-state situation.

The method for computing the critical sediment diameter is given below.

1. First, a steady flow field is simulated in interFoam.
2. The product of the bed shear stress utility *wallShearStress*, the α-fraction and the density of water (1000 km/m^3) is extracted using ParaView as shown in the

attachment *wallShearStressUtility.py*. The attachments are described in Appendix 7.

3. Next, *wallShearStress,* the riverbed coordinates and the turbulent kinetic energy are interpolated from an unstructured to a structured grid. This is done in Python using the function *scipy.interpolate.griddata* and shown in the attachment *codeFroudeNumber.py*.
4. The bed slope correction factor K is calculated according to equation (2.5). The angle of repose is 45 degrees for downhill slopes and 34 degrees for uphill slopes.

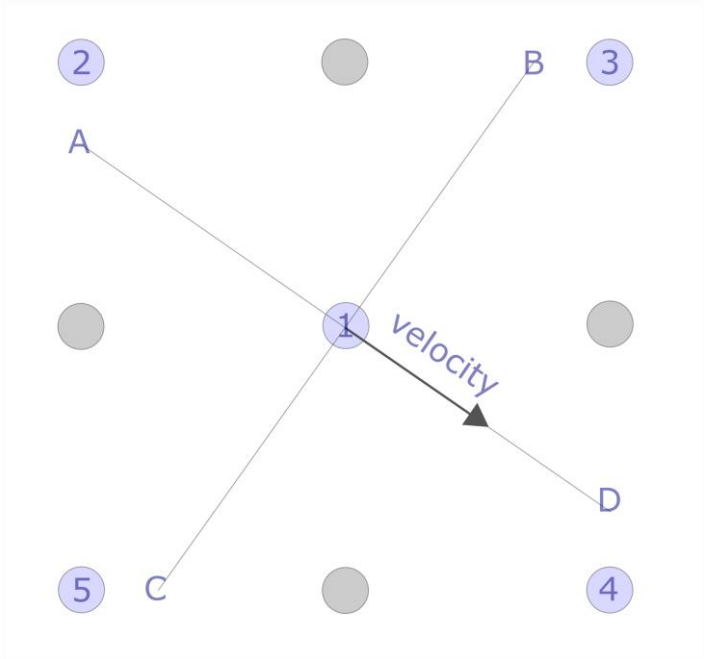

Figure 9: Sketch of calculation of bed slope correction on a structured grid.

Figure 9 illustrates the calculation of the bed slope correction factor K. The circles show grid points on a structured grid. After the interpolation, the grid is structured. The bold arrow illustrates the velocity vector. Each circle has an x, y, and z coordinate. The velocity vector is retrieved from grid point number 1.

The bed slope angle parallel to the flow is calculated between the coordinates of A and D. The coordinate of A is linearly interpolated between the coordinates of point 2 and point 5. The coordinate of D is linearly interpolated between the coordinates of point 3 and point 4.

The bed slope angle normal to the flow is calculated between the coordinates of B and C. The coordinate of B is linearly interpolated between the coordinates of point 2 and point 3. The coordinate of C is linearly interpolated between the coordinates of point 4 and point 5.

5. The non-dimensional critical shear stress on a sloped bed is calculated. According to Buffington and Montgomery (1999), the critical shear stress on a flat riverbed is $\theta_0 = 0.045$. By applying equation (2.4) and that $\theta_c \propto \tau_c$, the following equation for the non-dimensional critical shear stress on a sloped bed can be derived:

$$\theta_c = K \cdot 0.045\,. \tag{3.1}$$

6. The critical sediment diameter at the riverbed is calculated by setting the dimensionless shear stress at the riverbed equal to the dimensionless critical shear stress on an inclined bed. In dimensionless form, this can be expressed as

$$\theta = \theta_c \cdot K. \tag{3.2}$$

Substitution of equation (2.1) into equation (3.2) gives:

$$\frac{\tau}{\rho \cdot g \cdot (s-1) \cdot d_c} = K \cdot 0.045\,. \tag{3.3}$$

Here, d_c is a critical sediment diameter. A value of 2.65 (-) is used for s. Lastly, equation (3.3) is solved with respect to the critical sediment diameter:

$$d_c = \frac{\tau}{\rho \cdot g \cdot (s-1) \cdot K \cdot 0.045} \tag{3.4}$$

Equation (3.4) indicates that stable sediments at the riverbed must be greater than d_c. If the sediment diameter is lower than this critical value, the non-dimensional shear stress on a sloped bed will be lower than the critical shear stress, and scour will take place.

3.3 Investigation of two-dimensional channel flow

A two-dimensional channel is investigated using interFoam. The aim of this exercise is to relate the numerical roughness, k_s, to the Manning-Strickler and compare simulated shear stresses with theoretical shear stress.

3.3.1 Mesh generation, boundary- and initial conditions

The simulations consist of a 2km long channel with a constant downstream water level and a varying upstream water level. A backwater effect occurs in the downstream part of the channel and the upstream water level converges towards the normal depth. The geometry, boundary- and initial conditions of the two-dimensional channel are further described below and illustrated in Figure 10.

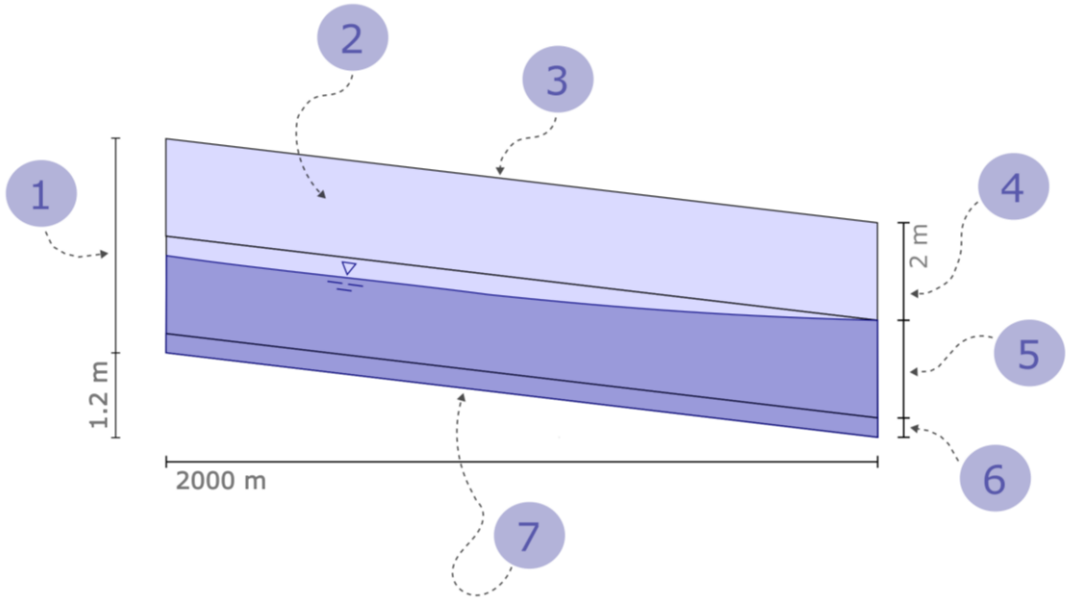

Figure 10: The setup of the 2D channel. The figure is not in scale.

Each number in Figure 10 describes a property of the channel. These numbers are described in the following:

1. The inflow is constant, but the water level is varying. This is achieved using the boundary condition *variableHeightFlowRateInletVelocity* for the velocity and the boundary condition *variableHeghtFlowRate* for the velocity. The case is run with 3 different discharges for each value of k_s ($q = 1\frac{m^3}{s}$ and $q = 2\frac{m^3}{s}$ and $q = 5\frac{m^3}{s}$).
2. The sides have the boundary condition *empty* to make the case two-dimensional.
3. The boundary conditions of the roof of the channel are abstractions of an open atmosphere. The boundary condition for the velocity is *pressureInletOutletVelocity* and the boundary condition for the pressure is *totalPressure*.
4. The upper part of the channel is 2 m high for all cases and the cell size is 0.1m in the direction normal to the flow (upwards) and 0.4m in the streamwise direction.
5. Number 5 points towards the middle part of the channel. The cell size is 0.05m for $q = 1\frac{m^3}{s}$ and $q = 2\frac{m^3}{s}$ and 0.1m for $q = 5\frac{m^3}{s}$ m in the direction normal to the flow. The cell size is 0.4m in the streamwise direction. The outlet, consisting of points 4, 5 and 6 in Figure 10, has zero-gradient (Neumann) boundary conditions for all fields except for the alternative pressure, *p_rgh*, viscosity, *nut*, and the α-fraction, *alpha.water*. The alternative pressure is zero (Dirichlet boundary condition), and the viscosity is calculated from the other fields. The α-fraction has a fixed value equal to 1 in the middle and lowest part of the channel (number 5 and number 6) and a zero-gradient boundary condition in the upper part of the channel (number 4). A hRef file is added to the constant directory and changes the reference elevation to the desired elevation: the point between the middle (number 5) and upper part (number 4) of the channel (attachment *2Dchannel/constant/hRef*). The combination of a fixed value of 0 for the alternative pressure and the new reference elevation fixes the outlet water level between the middle and upper layers. Figure 10 shows that the downstream water level is fixed. The height of the middle layer and the hRef file are varied for each case. Thus, the outlet water depth is changed for each case. This is done to make the simulation reach uniform flow easier in the upstream part of the channel.
6. The height of the lowest cell layer is equal to two times k_s (Blocken, Stathopoulos, & Carmeliet, 2007).
7. The cell size in the length direction is 0.4m in the lowest cell layer. The riverbed has a rough wall boundary condition, *nutkRoughWallFunction*, and the roughness is determined by k_s. For each of the three discharges, 5 different k_s-values are evaluated (Table 4). This results in 15 different cases. The slope is constant 0.0006 (-).

Table 4: Input values for the sand-grain roughness.

$\boldsymbol{k_s}$ $(\boldsymbol{m})$
0.2
0.1
0.05
0.025
0.001

The simulation time is 4000 seconds for all $q = 1\frac{m^3}{s}$ and $q = 2\frac{m^3}{s}$ and 5000 seconds for $q = 5\frac{m^3}{s}$. The initial water level is specified using *rotatedBoxToCell* in the setFields directory. The initial depth is equal to the converged outlet depth for each case. Further setting can be found in the attachment *2Dchannel* for the case of $q = 1\frac{m^3}{s}$ and $k_s = 0.1m$.

3.3.2 Roughness calibration

One way to determine the k_s-value in a river is by relating the sediment grain size distribution to k_s using empirical formulas (Van Rijn, 1982). Another method to determine the k_s-value in a river is by relating k_s to the Manning-Strickler value (Meyer-Peter & Müller, 1948). However, the numerical implementation of roughness might differ from experimental behaviour. Therefore, the aim of this chapter is to relate the numerical roughness in OpenFOAM, k_s, to the Manning-Strickler value. The method is described below.

The two-dimensional channel cases are first simulated until the water levels converge. Then, the water depths are extracted 300 meters downstream of the inlet for all cases. The flow is approximately uniform at this location. The Manning-Strickler value is calculated as follows:

$$K_{st} = \frac{Q}{A \cdot R^{\frac{2}{3}} \cdot I^{\frac{1}{2}}} = \frac{q}{y^{\frac{5}{3}} \cdot I^{\frac{1}{2}}} \tag{3.5}$$

Here, q ($\frac{m^2}{s}$) denotes unit discharge, and the last equal sign comes from that $R \to y$ when $b \gg y$. This is valid for a two-dimensional case, where the width of the channel can be thought of as infinitely wide. Furthermore, by substituting equation (3.5) into equation (2.12), β can be calculated as follows:

$$\beta = \frac{q}{y^{\frac{5}{3}} \cdot I^{\frac{1}{2}}} \cdot k_s^{\frac{1}{6}} \tag{3.6}$$

Thus, the β-value is used to relate the k_s-value to the Manning-Strickler value and will finally be compared against values from literature (Meyer-Peter & Müller, 1948; US Army Corps of Engineers, 2016) and numerical implementations (Richter, Vereide, Mauko, Havrevoll, & Schneider, 2021; Almeland, Olsen, Bråveit, & Aryal, 2018; Chen, 2021).

3.3.3 Shear stress verification

The shear stress on the riverbed is a crucial parameter in scour models. The cases presented in section *3.3 Investigation of two-dimensional channel flow* are used to verify the shear stress computations in OpenFOAM. For uniform flow, the theoretical shear stress on the riverbed is calculated according to equation (2.9). Thus, the simulated bed shear stresses can be compared with the theoretical shear stress at the section of the channel where the flow is uniform. The shear stresses are evaluated 300 meters downstream of the inlet for all cases. Here, the simulated shear stress has stabilized, and the flow is approximately uniform. Both the shear stress based on the turbulent kinetic energy (equation (2.31)) and the shear stress based on the Reynold shear stress tensor (equation (2.35)) is compared against the theoretical uniform shear stress.

3.3.1 Verification of post-processing of Froude number

A procedure for post-processing of the Froude number along a slice of the domain is developed (attachment *codeFroudeNumber.py*). The coordinates of the free surface located where $\alpha = 0.5$ and the location of the riverbed are first exported from the simulation using function objects (attachment *Q135Fine/system/controlDict*). The free surface, the riverbed and the velocity along a slice are transferred to CSV files using ParaView (attachment *ParaView/froudeNumber.py*). The code in the attachment *codeFroudeNumber.py* interpolates the velocity to a structured grid using scipy.interpolate.griddata(). Thereafter, the velocity is integrated from the riverbed to the free surface by Simpson's rule using scipy.integrate.simps(). The depth-averaged velocity is the ratio of the integrated velocity to the depth. Finally, the Froude number can be computed along the slice:

$$F_r = \frac{\bar{u}}{(gy)^{0.5}} \tag{3.7}$$

Here, $\bar{u}$ denotes the depth-averaged velocity. This post-processing code is compared against the formula for a two-dimensional case:

$$F_{r_{control}} = \frac{\frac{q}{y}}{(gy)^{0.5}} \tag{3.8}$$

Equation (3.8) is valid for a two-dimensional channel case when the unit discharge is known. The code (attachment *codeFroudeNumber.py*) and equation (3.8) are compared in the two-dimension channel simulation with $q = 1\,m^2/s$ and $k_s = 0.2\,m$. The depth, y, in equation (3.8) is calculated as the distance from the riverbed to the free surface.

3.3.1 Verification of bed slope correction

The post-processing code of the bed slope correction of the critical sediment diameter (attachment *codeFroudeNumber.py*) is controlled against a hand calculation (equation (2.5)) for a two-dimensional channel simulation. The aim of the verification is to see if the bed slope correction produces the correct output on a bed with a constant slope. The code is tested on three data sets:

1) A two-dimensional channel simulation with a constant downhill slope.
2) A two-dimensional channel simulation with a constant uphill slope.
3) A two-dimensional channel simulation with a constant downhill slope and a constant bed slope normal to the flow direction.

3.4 Numerical simulation of Nidelva at Sluppen bridge

This chapter describes the interFoam simulations of Nidelva at Sluppen bridge. Three separate cases are simulated with different discharges. The discharges and outlet water depths are shown in Table 3. Figure 11 shows a flowchart of the steps for each of the three simulations. First, the extent of the river is determined in QGIS. Then, the background mesh is created using the utility *blockMesh*. Thereafter, the boundary conditions of the outlet pressure and the inlet discharge are changed. The case is copied into a fine and a coarse case. The fine case is created by refining a specified volume and adding layers using the utility *snappyHexMesh.* On the other hand, the coarse case is not refined nor are layers added using *snappyHexMesh.* The utility *snappyHexMesh* only snaps the background mesh to the STL files of the terrain and the piers for the coarse case. The coarse case is then initiated with the utility *setFields* and simulated until a steady state convergence is

achieved. The fine case uses the final timestep of the coarse case as initial conditions using the *mapFields* utility. The fine case is then simulated until convergence. Convergence is achieved when the imbalance between the inflow and the outflow is low, and the free surface is stable. The meshing is further described in section 3.4.1 Mesh generation and the boundary conditions are further described in section 3.4.2 Boundary and initial conditions.

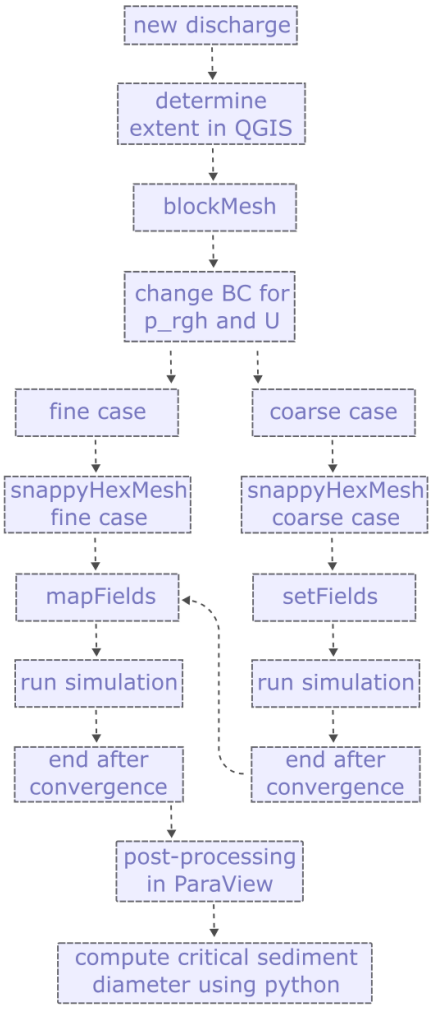

Figure 11: Flowchart for the computation of critical sediment diameter using interFoam.

The settings of the case of $Q = 135\, m^3/s$ is shown in the attachments *Q135Coarse* and *Q135Fine*. The settings for the background mesh and the boundary condition are similar for the coarse and fine cases. However, the setting of *snappyHexMeshDict* and the initial conditions are different for the coarse and fine cases (Figure 11). The settings that are changed for $Q = 85\, m^3/s$ and $Q = 400\, m^3/s$ are described in section *3.4.1 Mesh generation* and section *3.4.2 Boundary and initial conditions*.

3.4.1 Mesh generation

This chapter explains how the mesh is generated. The drawings of the bridge piers, the outlet water depth from HEC-RAS and the two digital elevation models are the material used to create the mesh. The mesh is created using the utility *blockMesh* (attachment

Q135Fine/system/blockMeshDict) and the utility *snappyHexMesh* (attachment *Q135Fine/system/snappyHexMeshDict* and *Q400Fine/system/snappyHexMeshDict*).

First, the DEMs from SWECO (Appendix 4) and NTNU (Appendix 1) are combined in QGIS. The DEM from NTNU covers the area outside of the DEM from SWECO. The Gaussian Filter by SAGA GIS is applied to the combined DEMs to smooth the surface and the edges. The settings of the Gaussian Filter are shown in Appendix 6. The smoothed DEM is exported as an STL file. An STL file of the piers is created in AutoCAD using the drawings of the piers (Appendix 2). The STL file of the terrain and the piers are used as geometric input to OpenFOAM and are shown in Figure 12.

Figure 12: The STL file of the terrain is shown in blue and the STL file of the piers is in white.

The initial background mesh is created using the utility *blockMesh.* The extent of the initial mesh covers a uniform elevation for each case. This elevation is 2 m above the outlet elevation. Figure 13 shows the horizontal extent of the initial mesh in the case of Q = 135 m^3/s. The STL file of the bathymetry is shown with the constant elevation of 7.1masl between white and black colour. It is seen that the initial mesh covers a constant elevation and that the blocks are oriented in a streamwise direction.

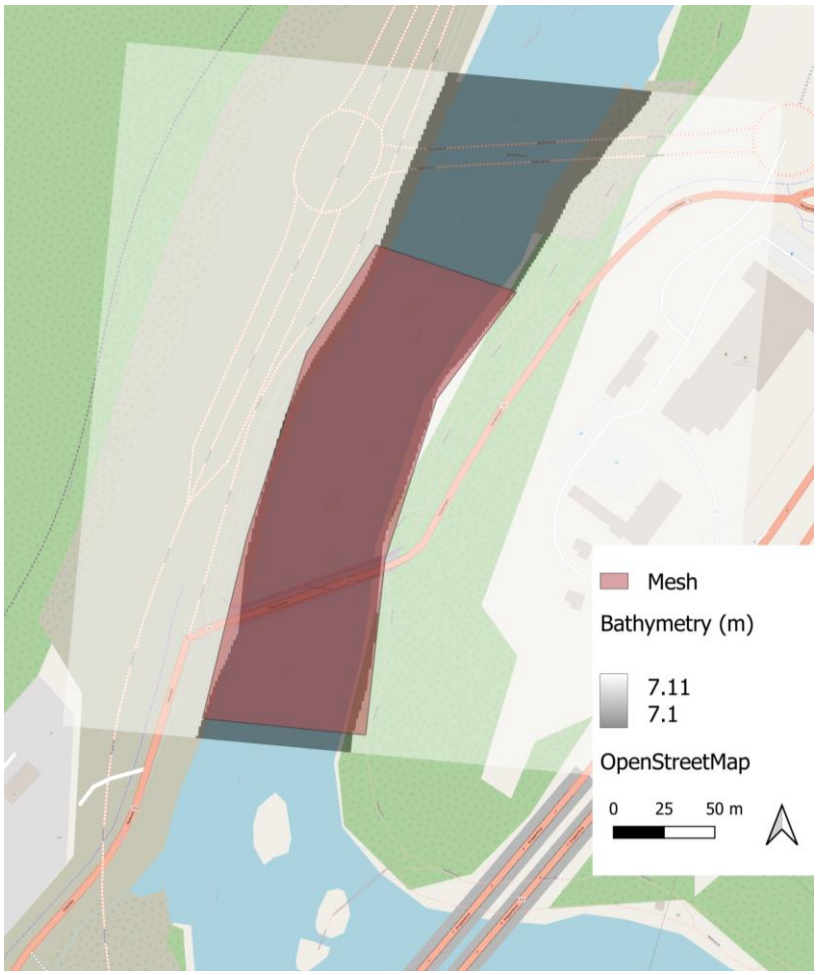

Figure 13: The horizontal extent of the initial mesh covers a constant elevation.

Figure 14 illustrates the vertical extent and the blocks of the initial mesh. Number 1 in Figure 14 points towards the 3 upper horizontal blocks. These blocks are filled with air during the simulation. Number 2 points towards the middle layer. Here, 3 blocks are filled with both air and water during the simulation. Number 3 points to the 3 bottom blocks filled with water during the simulation. The outlet water elevation is located at a fixed elevation between the bottom layer and the middle layer. The separation of the domain into 3 vertical block layers is made for the following reasons: 1) the top part, filled with air, can contain bigger cells, since the accuracy of the air phase is less important, 2) The middle layer extends above the outlet water elevation and contains finer cells. This is needed because the upstream water depth is higher than the downstream water depth due to the flow restrictions of the piers, and 3) the bottom layer is needed to fix the outlet water depth between the bottom layer and the middle layer. These blocks do also contain finer cells, similar to the middle layer.

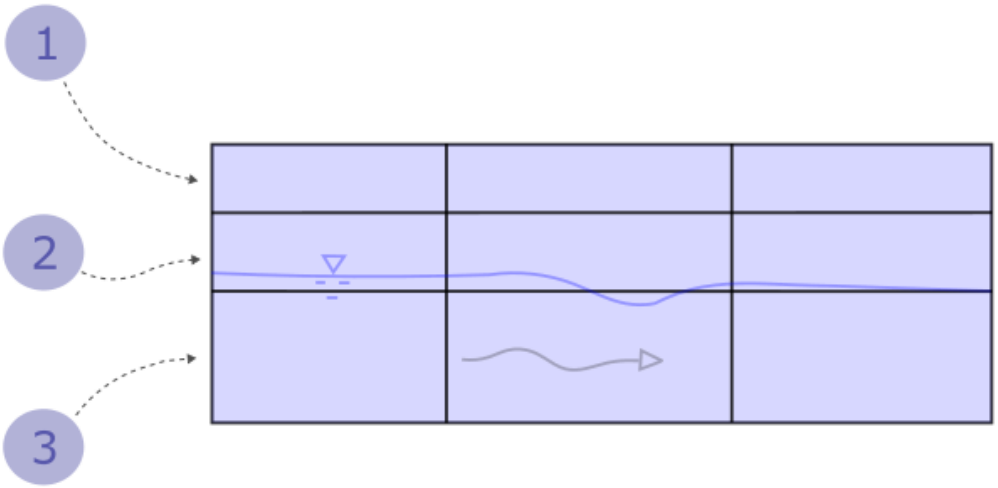

Figure 14: Vertical extent of the initial mesh along the stream direction.

Table 5 shows the cell sizes and vertical height of the top, middle and bottom layers denoted respectively 1, 2 and 3 in Figure 14.

Table 5: Cell sizes and vertical heights of the blocks.

Block	**Vertical height** (m)	**cell size** $width \cdot length \cdot height\ (m^3)$
Top layer (Number 1)	1.5	$0.8 \cdot 0.8 \cdot 0.5$
Middle layer (Number 2)	2	$0.8 \cdot 0.8 \cdot 0.2$
Bottom layer (Number 3)	equal to outlet elevation from the HEC-RAS simulation	$0.8 \cdot 0.8 \cdot 0.2$

Figure 15 shows the blocks in the initial mesh created by the utility *blockMesh* (attachment *Q135Fine/system/blockMeshDict*). The mesh consists of 9 blocks, three in the vertical direction and three in the horizontal direction.

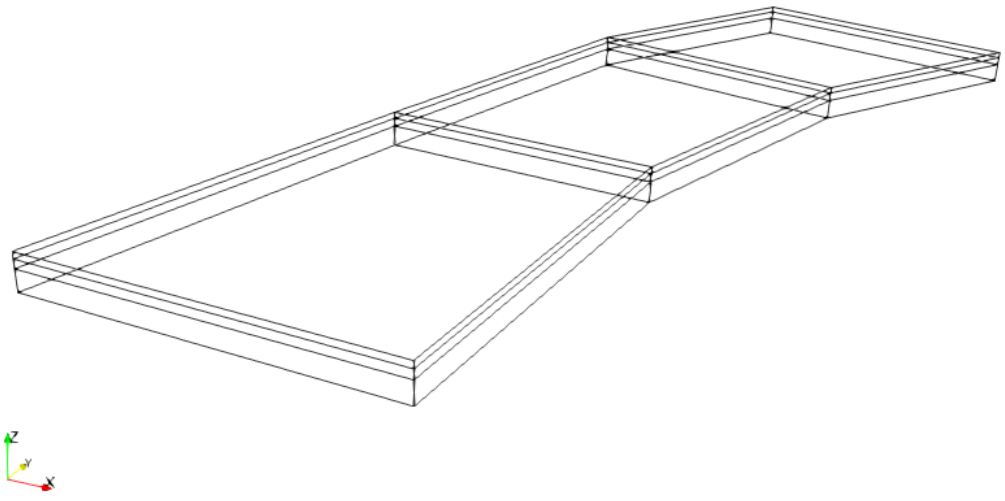

Figure 15: Initial mesh created by the blockMesh utility.

The last step of the mesh generation is to utilize the *SnappyHexMesh* utility. The usage differs for the coarse and fine cases. For the coarse cases, no layers nor refined regions are added. However, layers equal to 2 times k_s are added, and cells are refined within a specified region for the fine cases. The sketch of the final geometry is shown in Figure 16. The mesh is shown in blue, and the location of the scour hole is indicated by black contour lines. The cells inside the square *refined region* (Figure 16) have half the length of the cells outside the refined region in each direction for the fine cases.

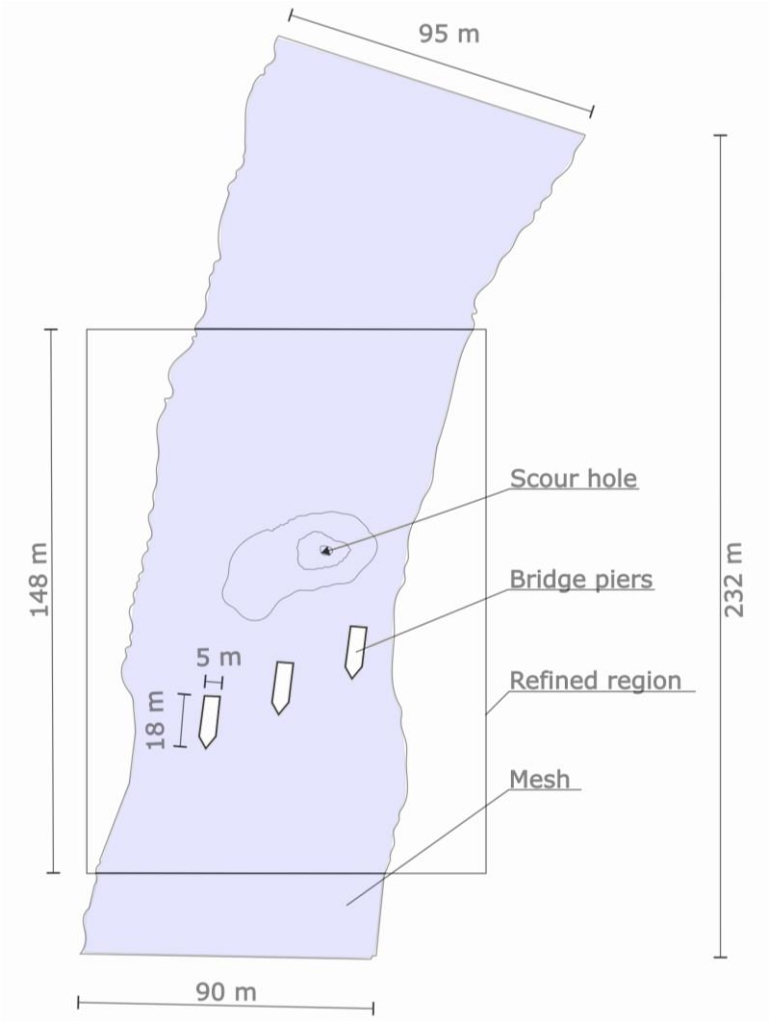

Figure 16: Extent of the mesh and location of the scour hole and refined region.

3.4.2 Boundary and initial conditions

A sketch of the geometry and the different boundaries are shown in Figure 17. A description of each point and the name of the boundary condition is described in Table 6. The settings of the boundary and initial conditions are found in the files in the attachment *Q135Fine/0*, *Q135Coarse/system/setFieldsDict* and *Q135Fine/system/mapFieldsDict*.

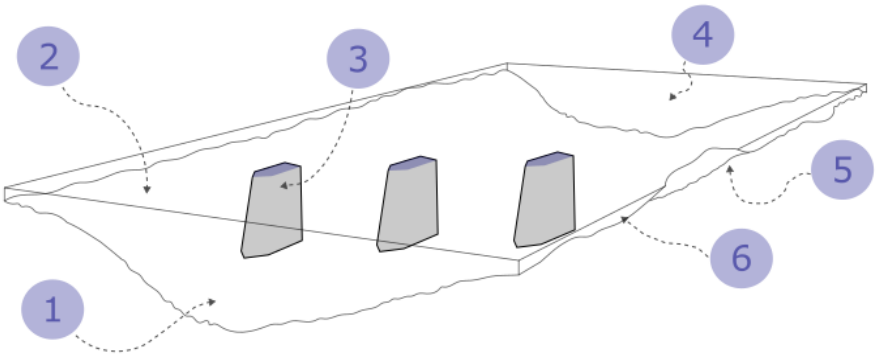

Figure 17: Sketch of geometry and location of boundary conditions.

Number 3 in Figure 17 shows the piers and number 5 shows the riverbed. The boundary condition *nutkRoughWallFunction* is used for both the riverbed and the piers. The parameter k_s is determined based on the result of the two-dimensional channel simulations. For both the riverbed and the piers, $k_s = 0.1\ m$ is applied. This corresponds to $K_{St} = 35\ m^{1/3}/s$ using equation (2.12) and $\beta = 24.1\ m^{0.5}/s$.

Number 4 in Figure 17 shows the outlet. The flow is subcritical at the site. For subcritical flow, the flow is determined by downstream conditions. Thus, the water depth at the outlet should be fixed in the numerical model. In this thesis, this is done by specifying a fixed value for *p_rgh* using the boundary condition *fixedValue.* The outlet boundary condition for *p_rgh* in the air phase is equal to 0 and equal to $1000 \cdot 9.81 \cdot z$ in the water phase. The parameter z denotes the distance from the horizontal plane $z = 0$ to the elevation of the outlet water depth. The outlet water depths for a given discharge are retrieved from the HEC-RAS simulation shown in Table 3.

Table 6: Boundary conditions in the simulation of Sluppen bridge.

Number	Description	Field	Boundary condition
1	**Inlet**	U	variableHeightFlowRateInletVelocity
		p_rgh	fixedFluxPressure
		alpha.water	variableHeightFlowRate
		k	fixedValue
		epsilon	fixedValue
		nut	calculated
2	**Atmosphere**	U	pressureInletOutletVelocity
		p_rgh	totalPressure
		alpha.water	inletOutlet
		k	inletOutlet
		epsilon	inletOutlet
		nut	calculated
3	**Piers**	U	noSlip
		p_rgh	fixedFluxPressure
		alpha.water	zeroGradient

		k	kqRWallFunction
		epsilon	epsilonWallFunction
		nut	nutkRoughWallFunction
4	**Outlet water**	U	zeroGradient
		p_rgh	fixedValue
		alpha.water	fixedValue
		k	zeroGradient
		epsilon	zeroGradient
		nut	calculated
4	**Outlet air**	U	zeroGradient
		p_rgh	zeroGradient
		alpha.water	zeroGradient
		k	zeroGradient
		epsilon	zeroGradient
		nut	calculated
5	**Riverbed**	U	noSlip
		p_rgh	fixedFluxPressure
		alpha.water	zeroGradient
		k	kqRWallFunction
		epsilon	epsilonWallFunction
		nut	nutkRoughWallFunction
6	**Sides**	U	pressureInletOutletVelocity
		p_rgh	totalPressure
		alpha.water	inletOutlet
		k	inletOutlet
		epsilon	inletOutlet
		nut	calculated

3.4.3 Scour protection regulations

The aim of this exercise is to present the method of how to calculate the critical sediment diameter around the Sluppen bridge piers according to the scour protection regulation.

The extent of the scour protection can be calculated using equation (2.6). Jenssen and Tesaker (2009) assumed an angle of 15 degrees between the length axis of the piers and the flow direction for piers in a river. For simplicity, the same angle is used in this study.

The D_{50} value is calculated using equation (2.7). The piers have a sharp edge towards the flow direction and a shape factor of $K_f = 2.3$ is used.

$$D_{50} = K_f \cdot \frac{0.692 V_{local}^2}{2g(s-1)} = 2.3 \cdot \frac{0.692 V_{local}^2}{2 \cdot 9.81(2.6-1)} \quad (3.9)$$

The variable V_{local} is retrieved from the numerical simulation 0.5 m from the upstream edge of the piers. Finally, D_{max} is 2 times D_{50}.

3.5 Physical model test of Nidelva at Sluppen bridge

A physical model of Nidelva and the Sluppen bridge piers is created. The model is created by modifying an existing model with a movable bed at the hydraulic laboratory of the

institute of Hydraulic Engineering and Water Resource Management, at the Graz University of Technology.

Froude scaling is applied to ensure an accurate representation of the ratio of inertia to gravity in the model and prototype. The geometric scale is determined by comparing the width of the existing model to the width of Nidelva at Sluppen bridge. This results in a geometric scale of 1:31.5. Technicians at the laboratory constructed scaled piers based on the drawings (Appendix 2), which were then placed in the model. The existing model has a riverbend opposite to the prototype, so the model piers are mirrored compared to the prototype. Additionally, a scour hole is dug out in the movable bed to imitate the prototype riverbed.

Figure 18: The physical model with scour hole and bridge piers.

The discharge is scaled after equation (2.14). A prototype discharge of $Q_p = 120\frac{m^3}{s}$ is evaluated. This corresponds to a scaled model discharge of $Q_m = 22\frac{l}{s}$. The outlet depth is controlled with an adjustable weir and the discharge is controlled upstream with a valve. The aim of the physical model is to recreate a surf wave between the piers. The budget is limited, so it is assumed that a wave should be made of low-cost materials, such as stones, wood, or large sandbags.

4 Results

4.1 Results of 2D channel cases

4.1.1 Roughness calibration

Longitudinal profiles of the water depths are shown in Figure 19, Figure 20 and Figure 21, similar to Figure 10. The water depths are extracted 300 meters downstream of the inlet. This user-specified depth is varied for each case.

Table 7). A β–value is computed for each case (

Table 8) according to equation (3.6).

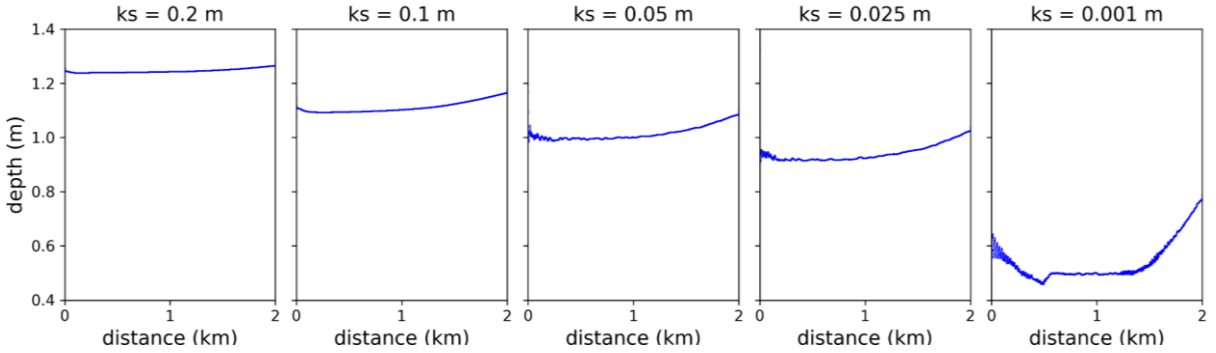

Figure 19: Depth of two-dimensional channel simulation for $q = 1\,m^2/s$.

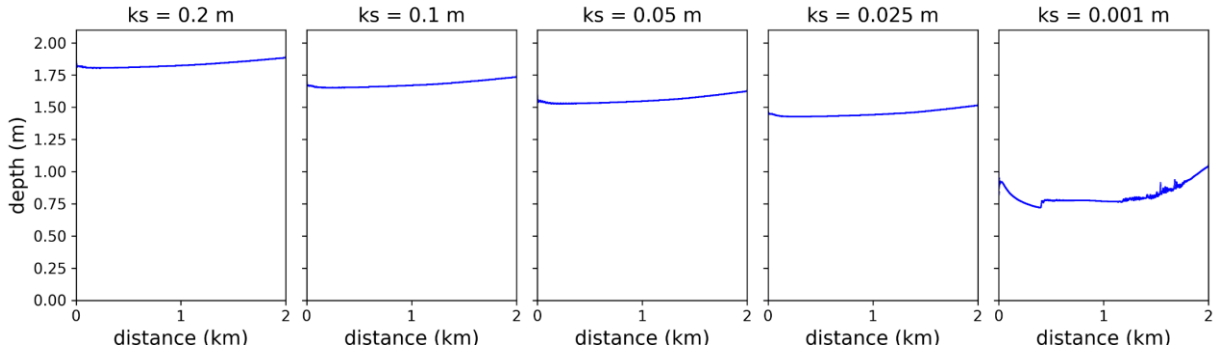

Figure 20: Depth of two-dimensional channel simulation for $q = 2\,m^2/s$.

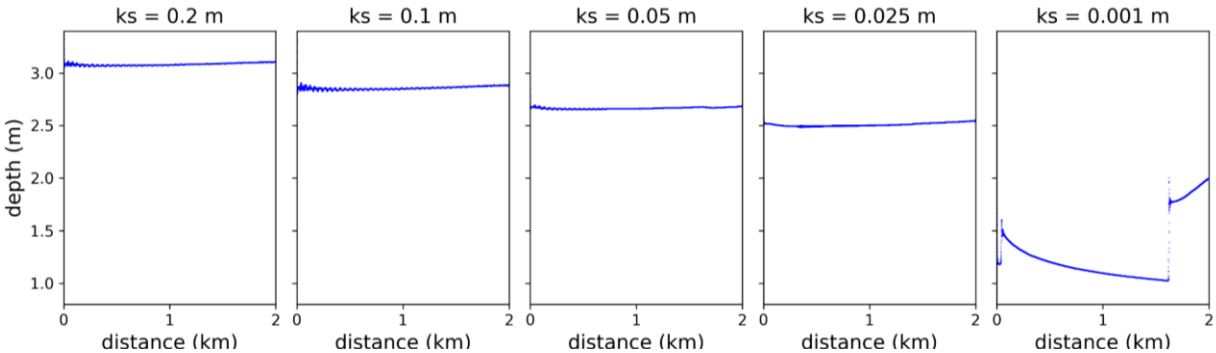

Figure 21: Depth of two-dimensional channel simulation for $q = 5\,m^2/s$.

The upstream water depths are to the left in each plot in Figure 19, Figure 20 and Figure 21. The upstream water depths are not fixed and vary with the roughness. It is seen that the water level increases with increasing roughness. The water depths to the right in each plot in Figure 19, Figure 20 and Figure 21 are fixed to a location close to the assumed uniform depth. This user-specified depth is varied for each case.

Table 7: Water depths are sampled 300 meters downstream of the inlet.

	Water depth (m)		
$\boldsymbol{k_s\ (m)}$	*q=1 m²/s*	*q=2 m²/s*	*q=5 m²/s*
0.2	1.24	1.81	3.07
0.1	1.09	1.65	2.85
0.05	1.0	1.53	2.65
0.025	0.92	1.43	2.49
0.001	0.51	0.74	1.28

Table 8: β-values are computed for all 2D channel cases.

	$\boldsymbol{\beta\ (m^{0.5}/s)}$		
$\boldsymbol{k_s\ (m)}$	*q=1 m²/s*	*q=2 m²/s*	*q=5 m²/s*
0.2	21.83	23.31	24.08
0.1	23.97	24.06	24.31
0.05	24.87	24.39	24.36
0.025	25.34	24.39	24.06
0.001	40.13	42.69	43.06

The free surfaces of the cases of $k_s = 0.001\,m$ are different than the cases of higher k_s-values. For $q = 1\,m^2/s$, $q = 2\,m^2/s$ and $q = 5\,m^2/s$, the critical depths are 0.47m, 0.74m, and 1.37m, respectively. The sampled depths, 300m from the inlet, are for $k_s = 0.001\,m$ and $q = 1\,m^2/s$, $q = 2\,m^2/s$ and $q = 5\,m^2/s$ slightly above, equal to and below the critical depths respectively. It should also be noted that the depths 300m from the inlet are not good predictors of uniform depths for the cases of $k_s = 0.001\,m$: uniform flow is located further downstream or not achieved (Figure 19, Figure 20 and Figure 21). Equation (3.6) does not seem to hold in the case of $k_s = 0.001$: the computed value of β is higher than for the cases of higher k_s-value. Excluding the case of $k_s = 0.001$, the average β–value for $q = 1\,m^3/s$, $q = 2\,m^3/s$ and $q = 5\,m^3/s$ can be seen in Table 9.

Table 9: Average β-values excluding the cases of $k_s = 0.001$.

	$\boldsymbol{\bar{\beta}\ (m^{0.5}/s)}$			
Statistical tool	*q=1 m²/s*	*q=2 m²/s*	*q=5 m²/s*	*total*
Average	24.0	24.04	24.2	24.1
Standard deviation of sample				0.86

4.1.2 Shear stress verification

The simulated shear stress (equation (2.31), equation (2.35)) and the theoretical shear stress (equation (2.9)) of the 2D cases are sampled 300 meters downstream of the inlet.

The longitudinal profiles of the simulated shear stresses (A and B) and theoretical shear stresses (C) are shown in Figure 22.

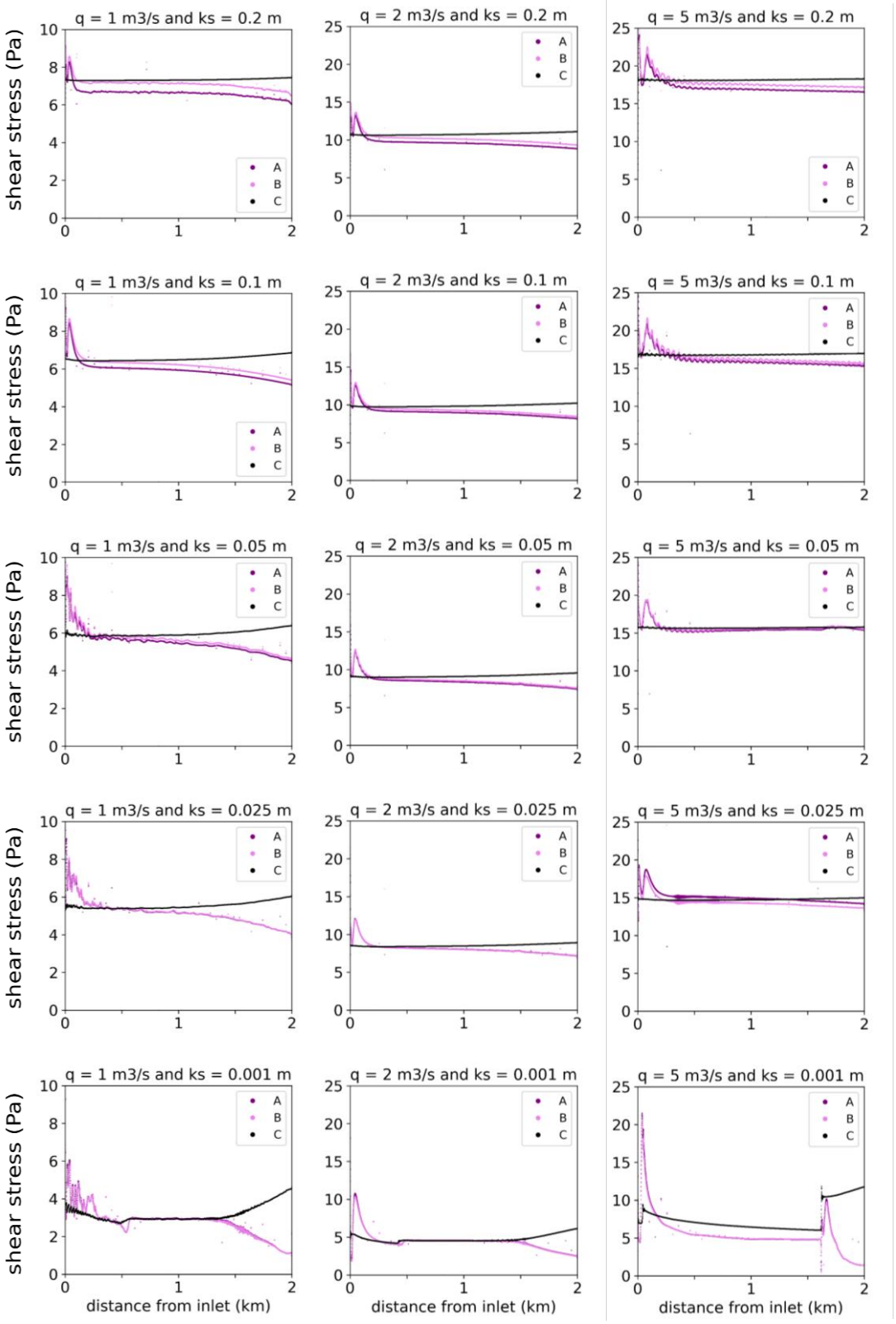

Figure 22: Plots of shear stresses in the two-dimensional channels.

Figure 22 shows the shear stresses denoted A, B and C. A denotes the simulated shear stress based on the turbulent kinetic energy according to equation (2.31). B denotes the

simulated shear stress based on Reynolds shear stress tensor from equation (2.35) and C denotes the theoretical shear stress assuming uniform flow according to equation (2.9). The shear stresses are compared 300 meters downstream of the inlet (Table 10). The left side of each plot in Figure 22 shows the upstream parts of the channel. Here, the flow is approximately uniform and the formula for the theoretical shear stress (equation (2.9)) is valid. The right side of each plot in Figure 22 shows the downstream parts of the channel. Here, the flow is not uniform and the formula for the theoretical shear stress is not valid.

It is observed that both the shear stress based on the Reynolds stress tensor and the turbulent kinetic energy mostly provides a close prediction of the theoretical shear stress during uniform flow (Figure 22). However, the case of $k_s = 0.001\text{m}$ and $q = 5\frac{\text{m}^2}{\text{s}}$ does not provide acceptable result.

Table 10: Comparison of simulated shear stress and theoretical shear stress.

$\boldsymbol{q}$	$\boldsymbol{k_s}$	$\boldsymbol{\tau_{TKE}}$	$\boldsymbol{\tau_R}$	$\boldsymbol{\tau_{uniform}}$	$\frac{\boldsymbol{\tau_{TKE}-\tau_{uniform}}}{\boldsymbol{\tau_{uniform}}}$	$\frac{\boldsymbol{\tau_R-\tau_{uniform}}}{\boldsymbol{\tau_{uniform}}}$
(m^2/s)	*(m)*	*(N/m^2)*	*(N/m^2)*	*(N/m^2)*	*(%)*	*(%)*
1	0.2	6.7	7.17	7.3	-8.22	-1.51
1	0.1	6.09	6.38	6.44	-5.43	-0.93
1	0.05	5.8	5.96	5.87	-1.19	1.53
1	0.025	5.58	5.56	5.42	2.95	2.58
1	0.001	2.94	2.96	2.98	-1.34	-0.67
2	0.2	9.78	10.32	10.63	-8.0	-2.92
2	0.1	9.19	9.51	9.73	-5.55	-2.26
2	0.05	8.67	8.83	9.01	-3.77	-2.0
2	0.025	9.32	8.3	8.4	-0.95	-1.19
2	0.001	4.29	4.31	4.35	-1.38	-0.92
5	0.2	17.45	18.03	18.06	-3.38	-0.17
5	0.1	16.73	17.06	16.73	-0.18	1.79
5	0.05	15.23	15.37	15.23	-2.5	-1.6
5	0.025	15.18	14.49	15.18	3.41	-1.29
5	0.001	6.33	6.32	6.33	-15.6	-15.73
average					-3.41	-1.69
average excluding k_s = 0.001m					-2.54	-0.68

4.1.3 Convergence

The water level at the end time (blue curve) and the water level at 500s before the end time (red curve) is plotted in Figure 23, Figure 24 and Figure 25 for $q = 1\ m^2/s$, for $q = 2\ m^2/s$ and for $q = 5\ m^2/s$, respectively. It is shown that the water level is steady over the 500 last seconds of the simulation.

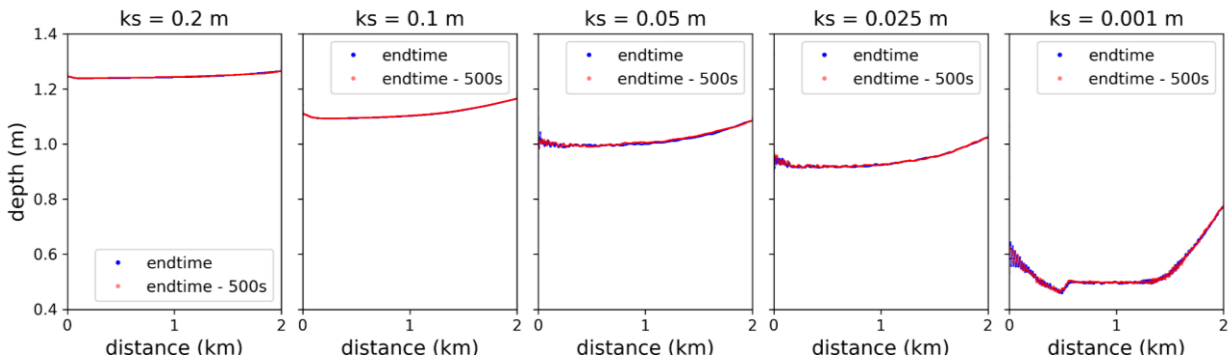

Figure 23: The water depth at the end time and 500 seconds before the end for $q = 1\ m^2/s$.

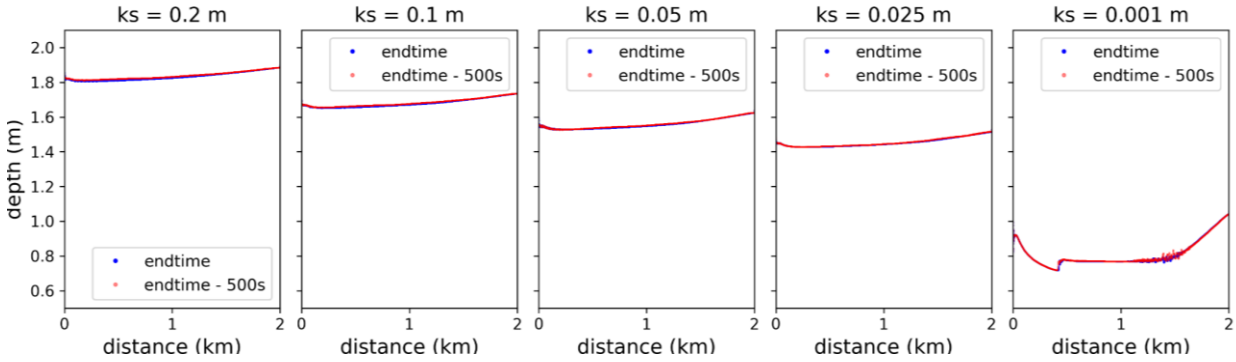

Figure 24: The water depth at the end time and 500 seconds before the end for $q = 2\ m^2/s$.

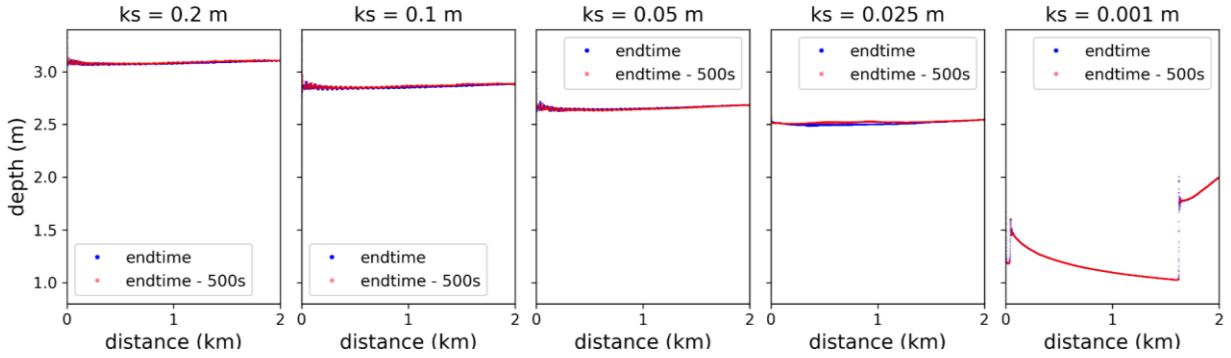

Figure 25: The water depth at the end time and 500 seconds before the end for $q = 5\ m^2/s$.

4.1.4 Y⁺-values

The y⁺-values are retrieved from the simulation and plotted in Figure 26, Figure 27 and Figure 28. The values of y^+ range from around 100 for $k_s = 0.001\ m$ to $2 \cdot 10^4$ for $k_s = 0.2\ m$.

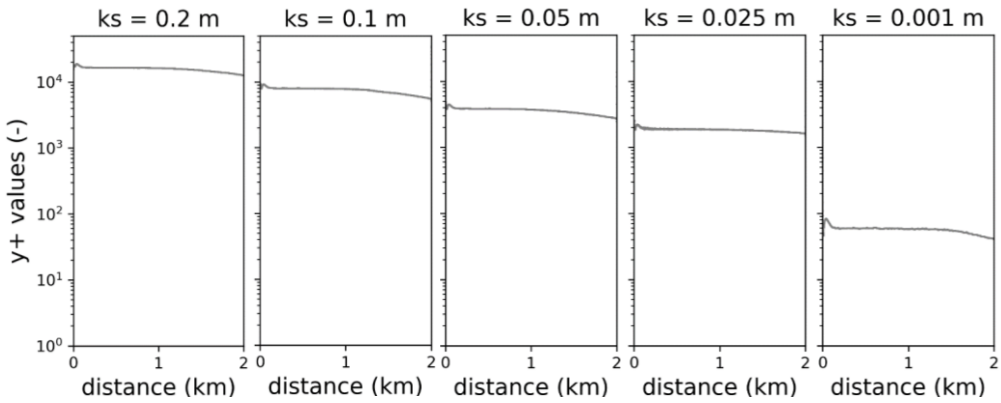

Figure 26: Y⁺ values of two-dimensional channel simulations for $q = 1\ m^2/s$.

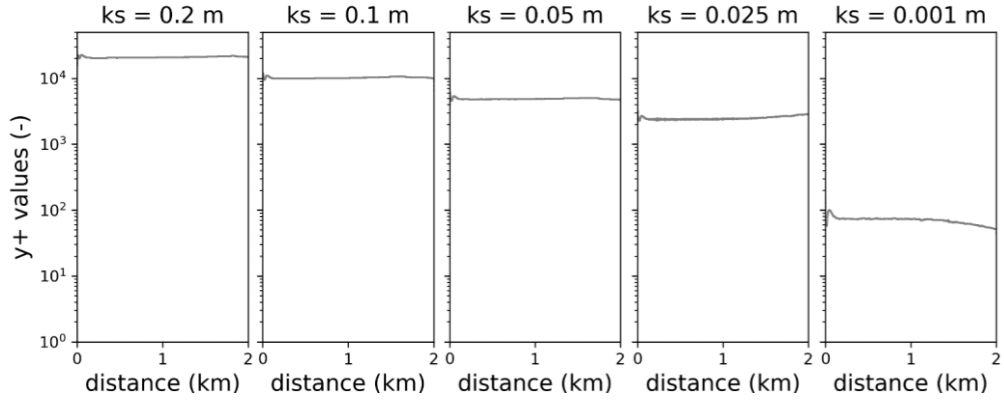

Figure 27: Y⁺ values of two-dimensional channel simulations for $q = 2\ m^2/s$.

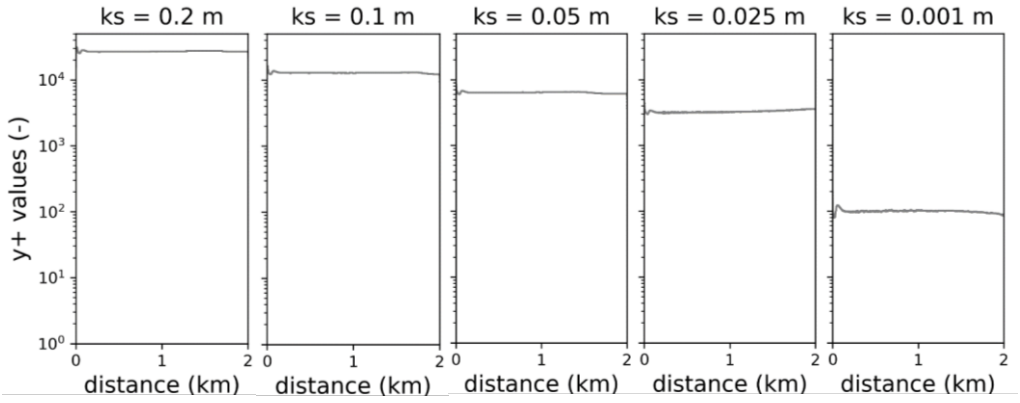

Figure 28: Y⁺ values of two-dimensional channel simulations for $q = 5\ m^2/s$.

4.1.5 Verification of post-processing of Frode number

The post-processing code of the Froude number (attachment *codeFroudeNumber.py*) is controlled against an easier calculation of the Froude number (equation (3.8)). The verification is executed on a two-dimensional channel simulation as described in section *3.3.1 Verification of post-processing of Froude number*.

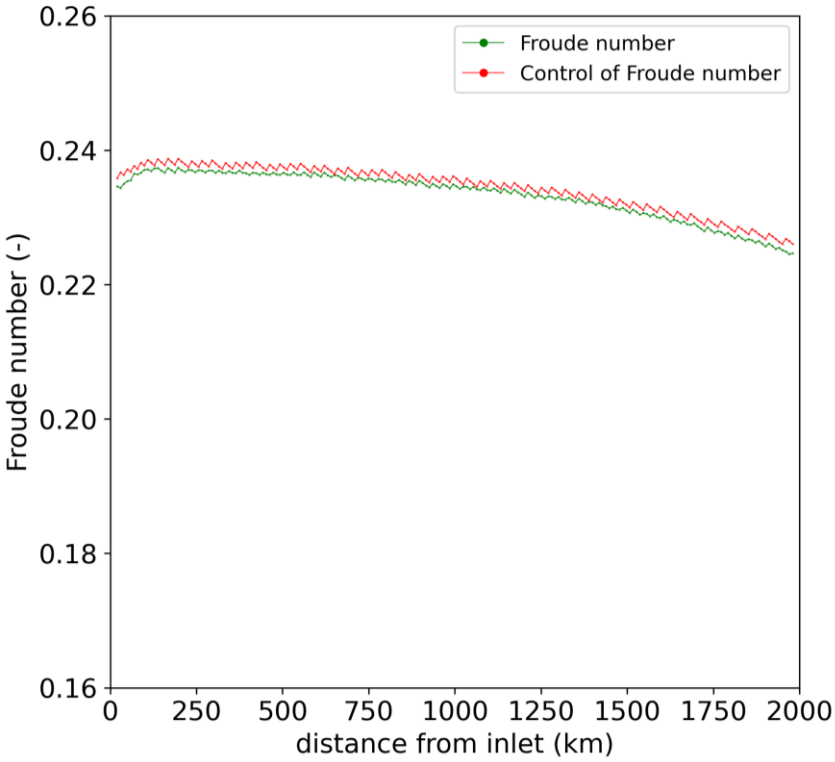

Figure 29: Control of the post-processing code for computing the Froude number.

Figure 29 shows the Froude number calculated by the post-processing code (attachment *codeFroudeNumber.py*) and a control calculation of the Froude number according to equation (3.8). The two-dimensional channel simulation has a unit discharge of $q = 1\,m^2/s$ and a sand-grain roughness of $k_s = 0.2\,m$. Figure 29 shows a previous simulation and is not included in Figure 19. The maximum difference between the control of the Froude number and the post-processing code of the Froude number is 0.85%.

4.1.6 Verification of bed slope correction

The post-processing code of the bed slope correction factor, *K*, (attachment *codeFroudeNumber.py*) is tested on a two-dimensional channel simulation (Figure 30). A hand calculation of *K* (equation (2.5)) is used to control the code. The verification is repeated three times with different slopes parallel to the flow (ϕ) and normal to the flow (α). The angle of repose for downhill slope ($\phi > 0$) is set equal to 45 degrees and equal to 34 degrees for uphill slope ($\phi < 0$). Table 11 show no errors in the code for the tested cases.

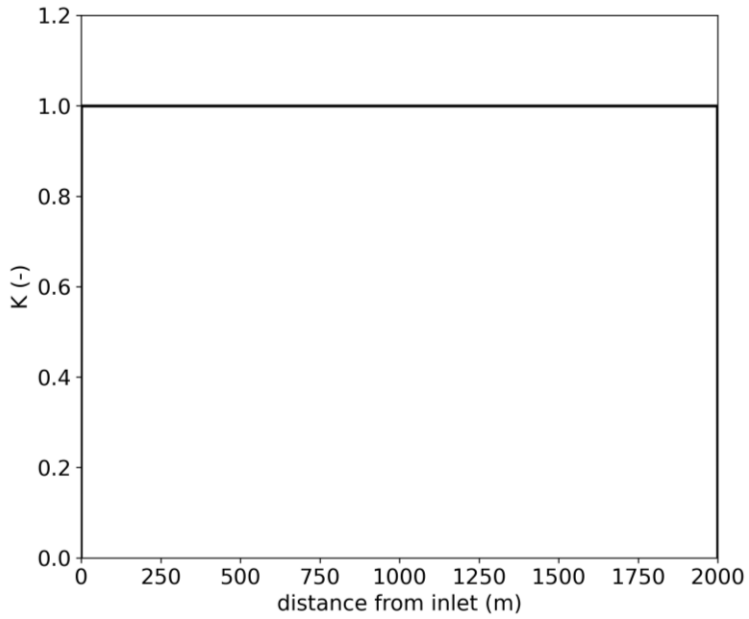

Figure 30: The bed slope correction factor, *K,* for a constant downhill slope.

Table 11: Verification of the code of the bed slope correction factor.

Case	post-processing code of K	Hand calculation of K	Difference
$\phi = 0.0006, \alpha = 0$	0.99942699	0.99942699	0
$\phi = -0.0006, \alpha = 0$	1.00075823	1.00075823	0
$\phi = 0.0006, \alpha = 0.01$	0.99469984	0.99469984	0

4.1.7 Effect of first cell height

Figure 31 shows the water depths for $q = 1\ m^2/s$ and $k_s = 0.1\ m$ when the height of the cells closest to the riverbed is varied. Three simulations are carried out with the cells closest to the riverbed being 0.2m, 0.05m and 0.01m, respectively. The depth is shown to be approximately similar for the first cell heights of 0.2m and 0.05m but is lower when the first cell height is 0.01m.

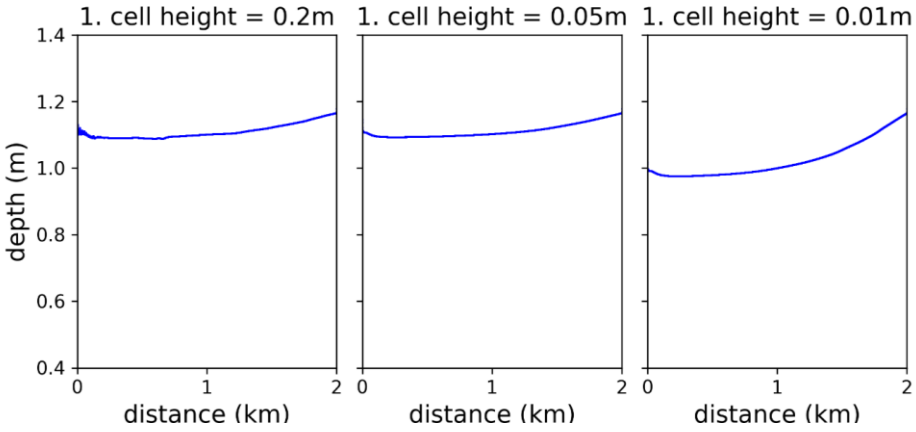

Figure 31: Height of cells closest to the riverbed is varied for $q = 1\ m^2/s$ and $k_s = 0.1\ m$.

4.2 Numerical simulation of Nidelva at the Sluppen bridge piers

4.2.1 Froude number and hydraulic jump

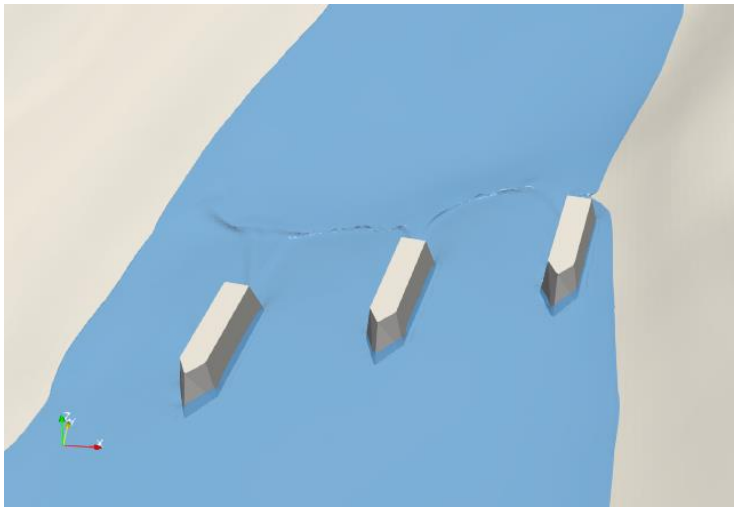

Figure 32: The free surface, the piers and the terrain are shown for $Q = 135\frac{m^3}{s}$.

The free surface for $Q = 135\frac{m^3}{s}$ is shown in Figure 32 together with the piers and the terrain. A wave is visible downstream of the piers. Figure 33 shows the domain for $Q = 135\frac{m^3}{s}$. The domain is sliced on two locations. The slice to the left is in the following denoted the west slice, and the slice to the right is denoted the east slice.

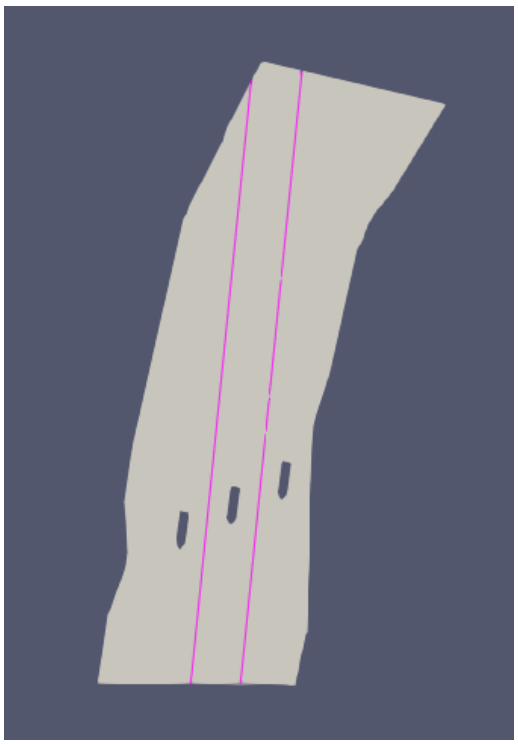

Figure 33: The simulation is sliced on two locations as shown above.

Figure 34, Figure 36 and Figure 38 show the west slice in Figure 33 for $Q = 85\frac{m^3}{s}$, $Q = 135\frac{m^3}{s}$ and $Q = 400\frac{m^3}{s}$, respectively. The blue curve shows the free surface, the riverbed is plotted in black, the Froude number is shown with a green color and the location of the hydraulic jump is indicated with a dotted line. The pier to the west of the west slice is located between 60m and 76m in the y-direction, and the east pier is located between 71m and 86m in the y-direction. The flow is subcritical upstream of the piers, the flow is supercritical downstream and in between the piers and the tailwater is subcritical. The dotted line in Figure 34, Figure 36 and Figure 38 goes from the hydraulic jump and intersects the graph of the Froude number at a value below 1.

Figure 35, Figure 37 and Figure 39 show the west slice in Figure 33 for $Q = 85\frac{m^3}{s}$, $Q = 135\frac{m^3}{s}$ and $Q = 400\frac{m^3}{s}$, respectively. The pier to the west of the east slice is located between 71m and 86m in the y-direction, and the east pier is located between 81m and 95m in the y-direction. The dotted line in Figure 35, Figure 37 and Figure 39 goes from the hydraulic jump and intersects the graph of the Froude number at a value below 1.

Figure 38 and Figure 39 show large variations in the free surface around the hydraulic jump. Figure 38 shows variation in the free surface in the upstream part of the wave, while Figure 39 indicates the formation of waves downstream of the hydraulic jump. The simulations of $Q = 85\frac{m^3}{s}$ and $Q = 135\frac{m^3}{s}$ show some of the same patterns as Figure 39: the east slices have small surface waves downstream of the hydraulic jump (Figure 35 and Figure 37).

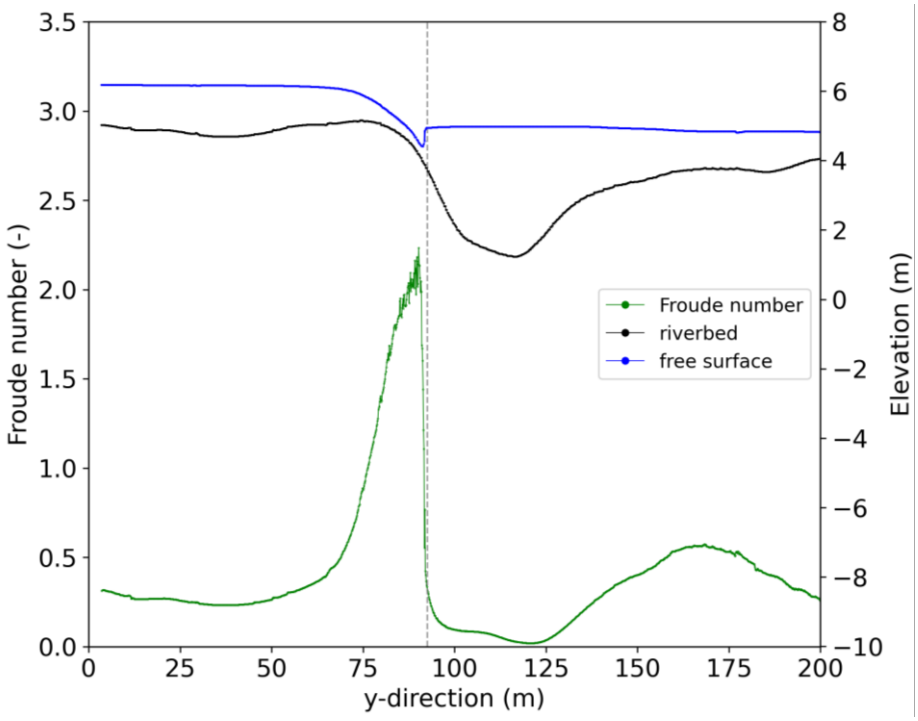

Figure 34: The free surface and Froude number for $Q = 85\frac{m^3}{s}$ along the west slice.

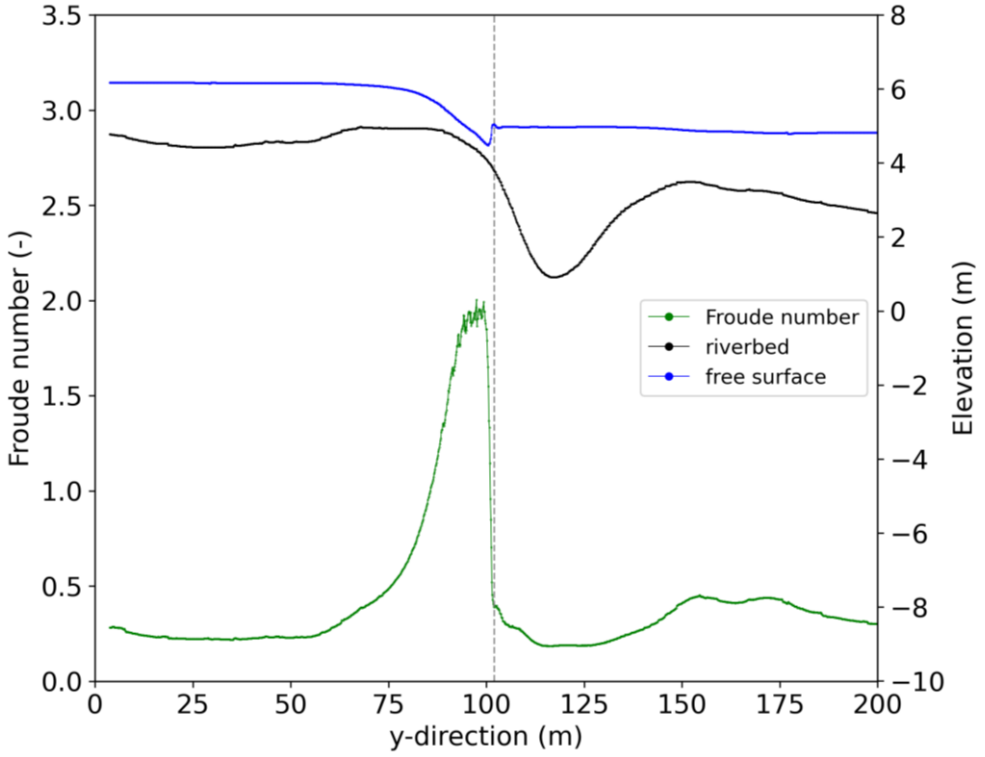

Figure 35: The free surface and Froude number for $Q = 85 \frac{m^3}{s}$ along the east slice.

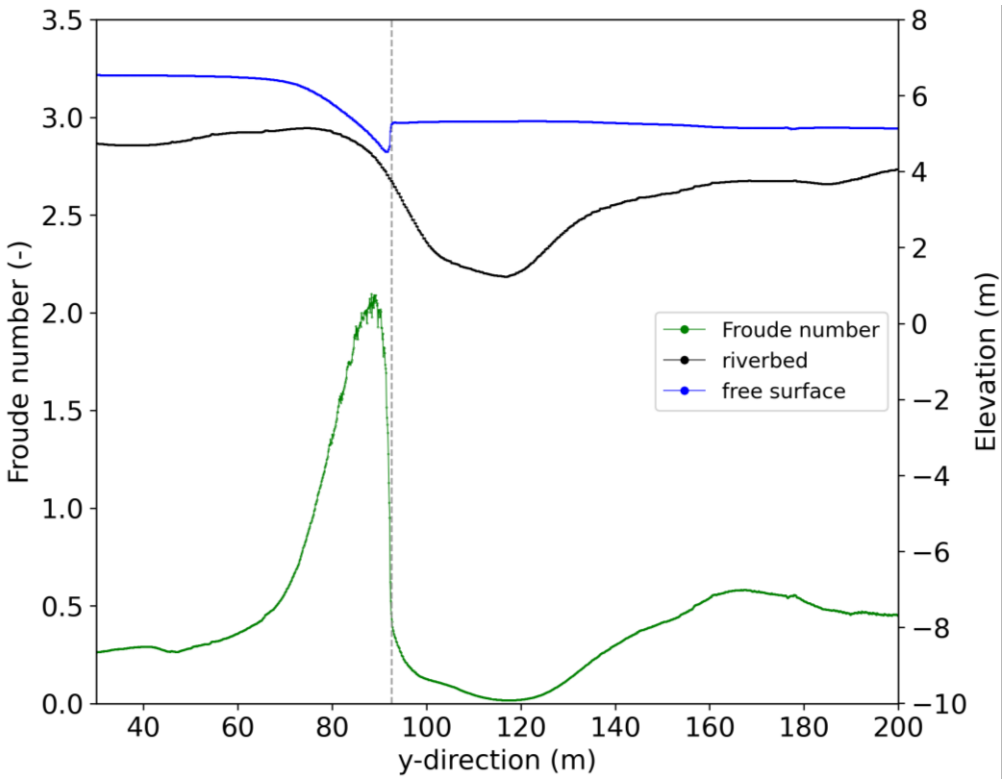

Figure 36: The free surface and Froude number are shown for $Q = 135 \frac{m^3}{s}$ along the west slice.

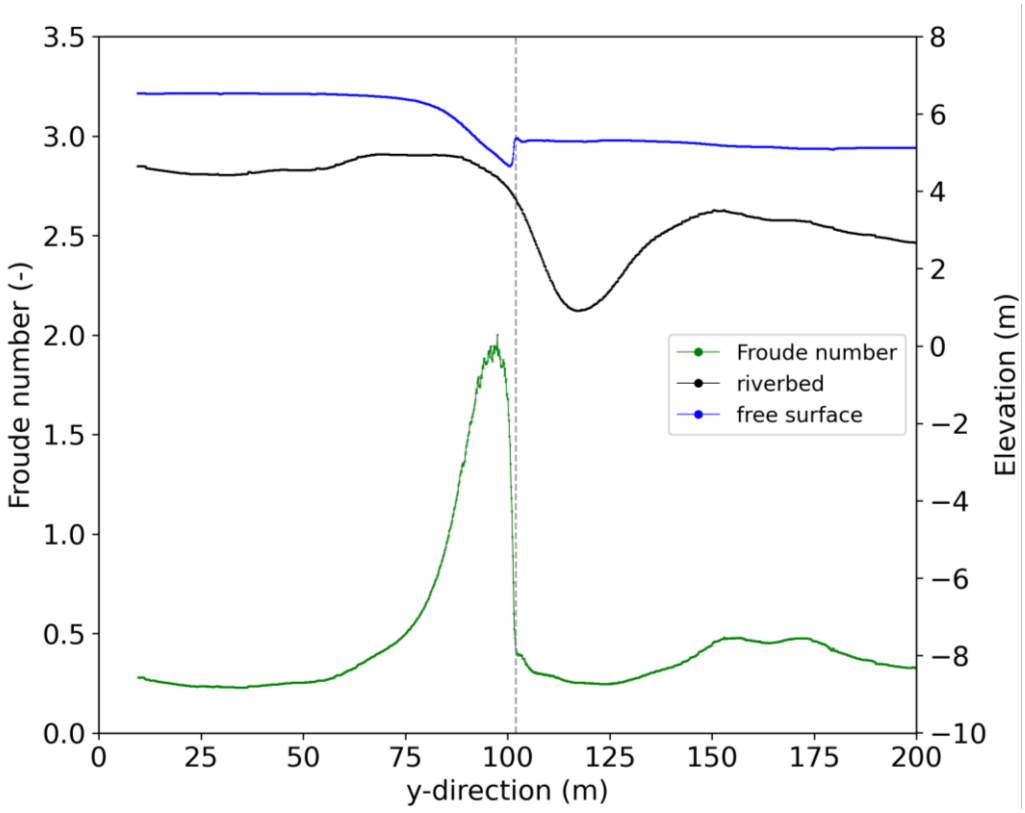

Figure 37: The free surface and Froude number are shown for $Q = 135 \frac{m^3}{s}$ along the east slice.

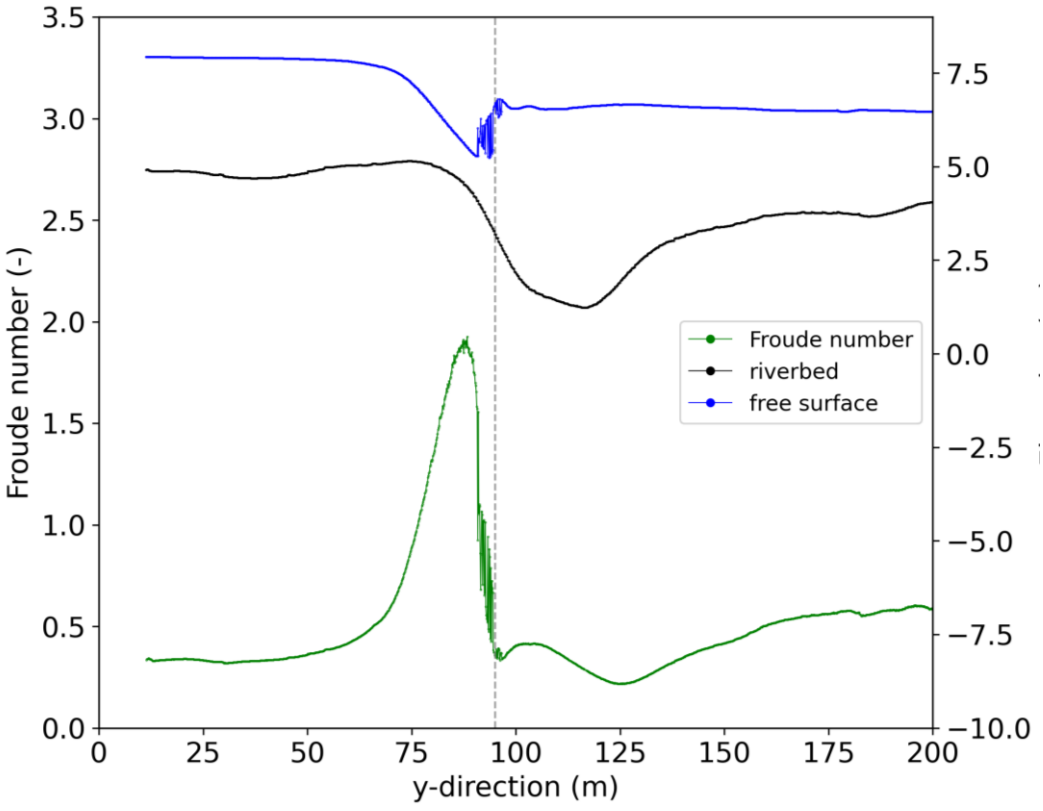

Figure 38: The free surface and Froude number are shown for $Q = 400 \frac{m^3}{s}$ along the west slice.

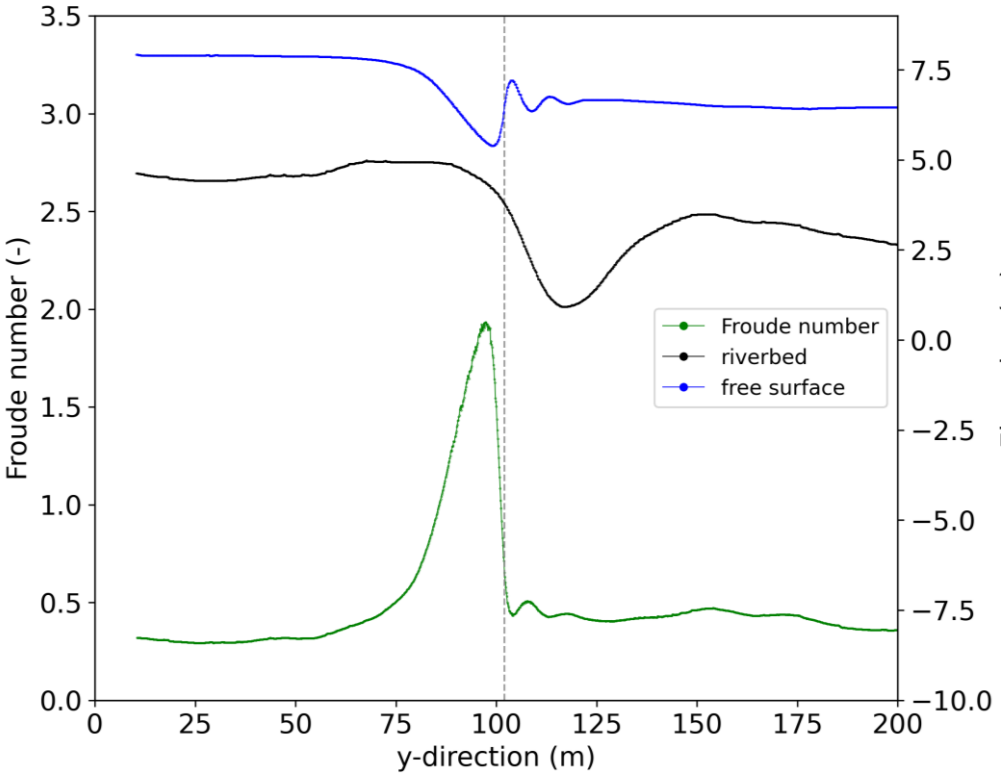

Figure 39: The free surface and Froude number are shown for $Q = 400 \frac{m^3}{s}$ along the east slice.

4.2.1 Comparison with water level measurements

The simulated water elevation for $Q = 135 \frac{m^3}{s}$ and the observed water elevation is plotted in Figure 40 and Figure 41 for the west and east slice, respectively. The water level measurements performed by SWECO are shown in red colour and the measurements done by NTNU are visible in green colour. All the measurements are taken on the east bank. The measurements and the simulation do not have the same discharge. The measurements performed by SWECO were taken on December 15, 2022, between 12:55 and 13:04 with a discharge of 124.6 m^3/s (The Norwegian Water Resources and Energy Directory, 2023). The measurements done by NTNU were taken on September 11, 2022, between 08:23 and 08:33 with a discharge of 142.4 m^3/s (The Norwegian Water Resources and Energy Directory, 2023). The free surface in Figure 40 and Figure 41 is simulated with a discharge of 135 m^3/s. The simulated downstream water level is below the water level measurements and the simulated upstream water level is exceeding the water level measurements. The average difference between the 3 most upstream water level observations of both SWECO and NTNU and the simulated water level is 0.32m. The average difference between the 6 most downstream water level observations of both SWECO and NTNU and the simulated water level is 0.19m.

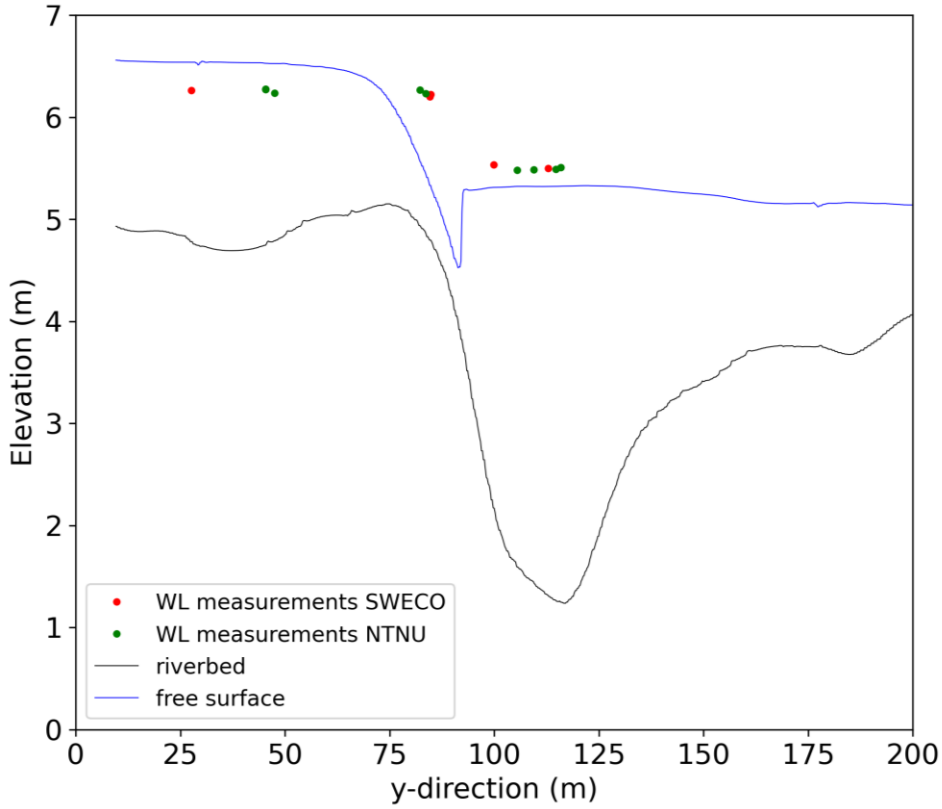

Figure 40: Simulated free surface at the west slice and observed water level.

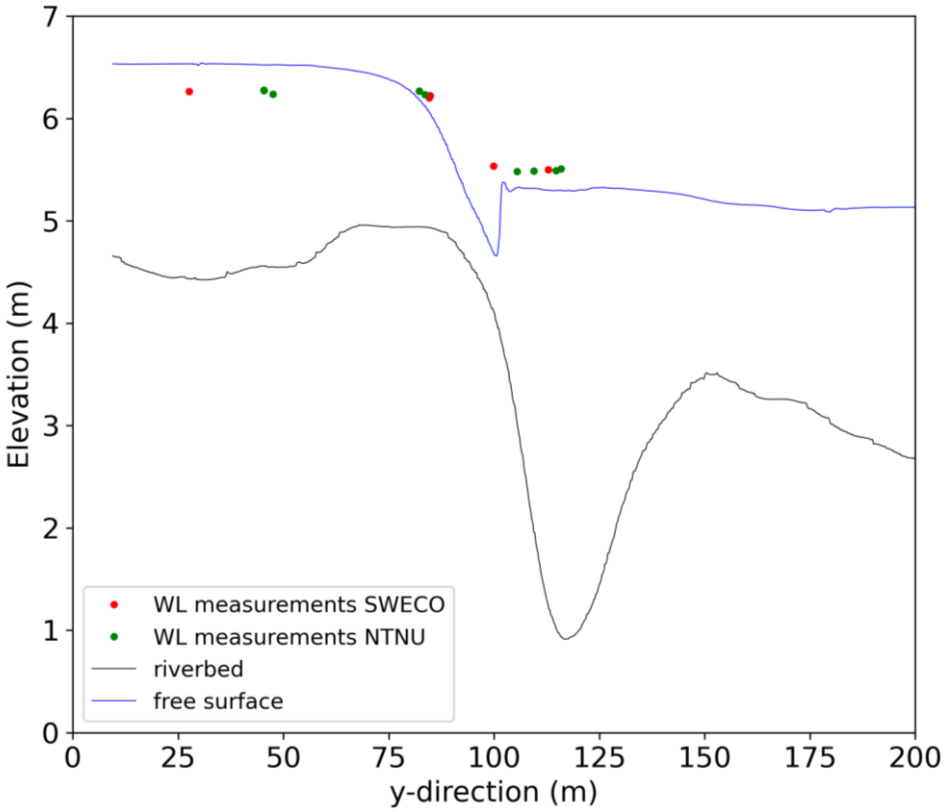

Figure 41: Simulated free surface at the east slice (Figure 33) and observed water level.

4.2.2 Bed shear stress

The bed shear stresses are retrieved from the simulations and shown for the $Q = 85\frac{m^3}{s}$, $Q = 135\frac{m^3}{s}$ and $Q = 400\frac{m^3}{s}$ in Figure 42, Figure 43 and Figure 44, respectively. Only the simulations with fine mesh are plotted. The plotted shear stresses are not a direct output from the InterFoam but interpolated to a structured grid. It is observed that the shear stresses are largest downstream and in between the piers. The shear stresses increase for increasing discharges. In addition, the area of increased shear stresses stretches further downstream for increasing discharges.

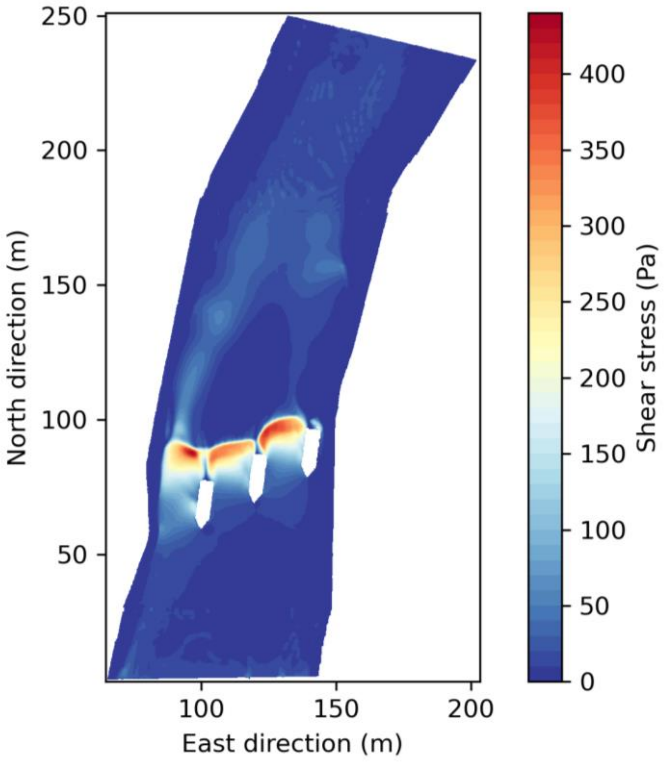

Figure 42: Riverbed shear stress for $Q = 85 \frac{m^3}{s}$.

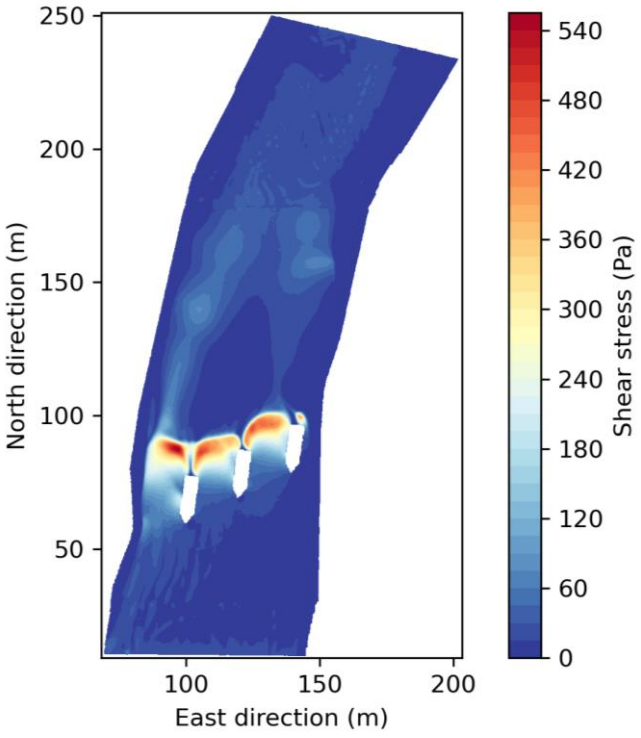

Figure 43: Riverbed shear stress for $Q = 135 \frac{m^3}{s}$.

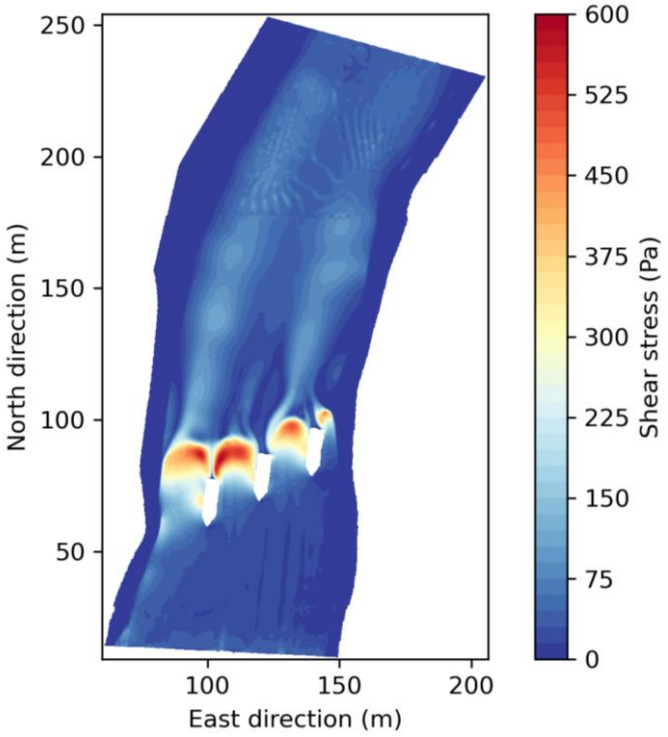

Figure 44: Riverbed shear stress for $Q = 400\frac{m^3}{s}$.

4.2.3 Critical sediment diameter

The critical sediment diameter is calculated using equation (3.4) and is shown in Figure 45 to Figure 47. These plots include the bed slope correction (equation (2.3)). The maximum critical sediment diameter is 0.72m, 0.88m and 1.0m for $Q = 85\frac{m^3}{s}$, $Q = 135\frac{m^3}{s}$ and $Q = 400\frac{m^3}{s}$, respectively. The critical sediment diameter follows the same patterns as the shear stresses: the critical sediment diameter increases for increasing discharge and the area of large critical sediment diameter increases for increasing discharges.

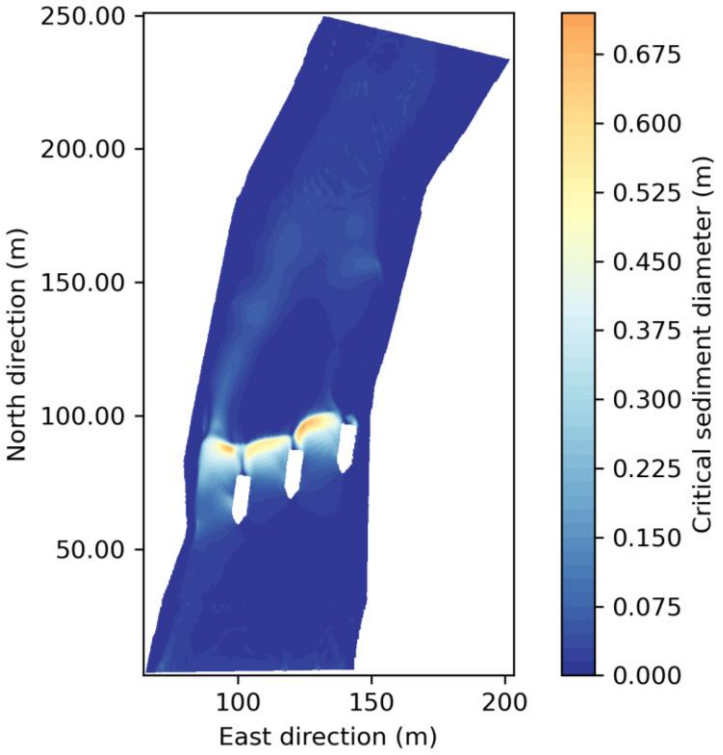

Figure 45: Critical sediment diameter for $Q = 85 \frac{m^3}{s}$.

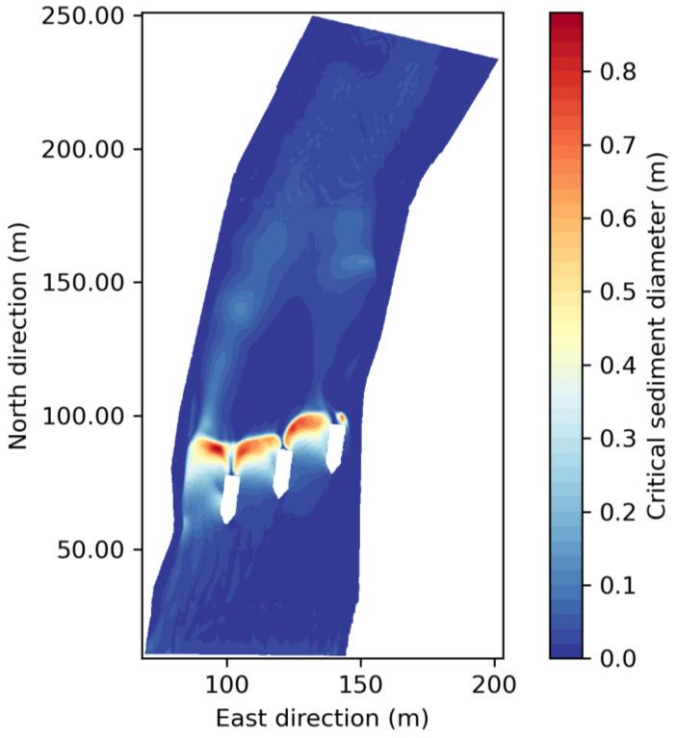

Figure 46: Critical sediment diameter for $Q = 135 \frac{m^3}{s}$.

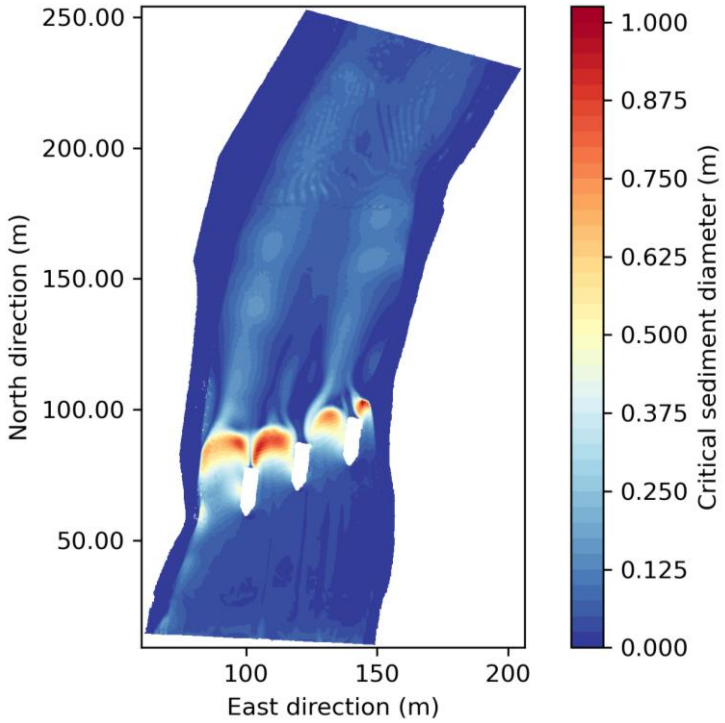

Figure 47: Critical sediment diameter for $Q = 400\frac{m^3}{s}$.

4.2.1 Effect of bed slope correction of critical sediment diameter

The bed slope correction factors of the non-dimensional critical shear stress, *K*, are shown in the left plots of Figure 48, Figure 50 and Figure 52 for $Q = 85\frac{m^3}{s}$, $Q = 135\frac{m^3}{s}$ and $Q = 400\frac{m^3}{s}$, respectively. The right plots show the increase in critical sediment diameter due to the bed slope correction. Figure 49, Figure 51 and Figure 53 show the critical sediment diameter without the bed slope correction factor for $Q = 85\frac{m^3}{s}$, $Q = 135\frac{m^3}{s}$ and $Q = 400\frac{m^3}{s}$, respectively.

The bed slope correction factor *K* is generally below 1 towards the scour hole, above 1 in front of the piers and above 1 downstream of the deepest part of the scour hole where the riverbed rises. The map of *K* changes for each discharge. Figure 52 shows values of *K* above 1 towards the scour hole, opposite to Figure 48 and Figure 50. The increase in the critical sediment diameter is largest where the shear stresses are large, and *K* is below 1. (Figure 48, Figure 50 and Figure 52).

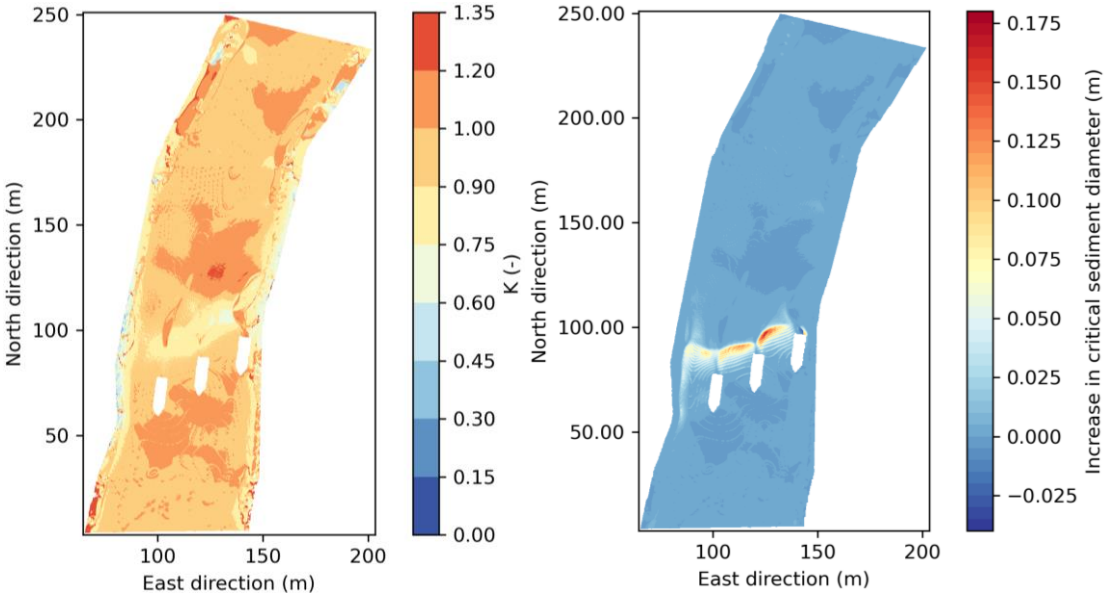

Figure 48: K and the corresponding increase in critical sediment diameter for $Q = 85 \frac{m^3}{s}$.

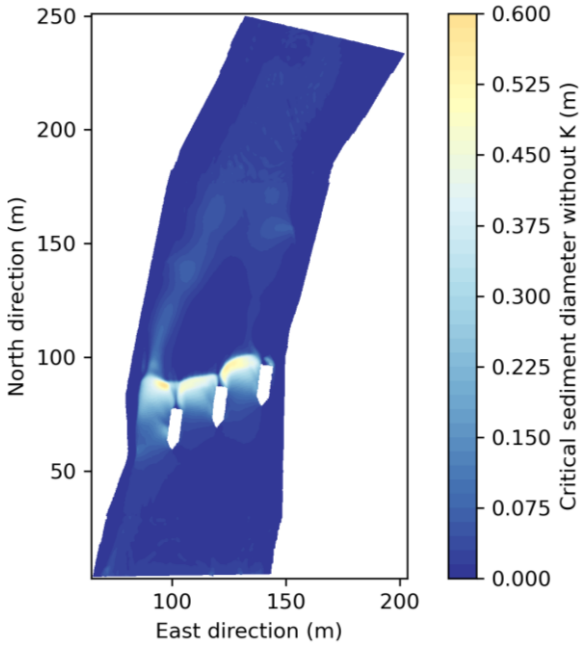

Figure 49: Critical sediment diameter without bed slope correction for $Q = 85 \frac{m^3}{s}$.

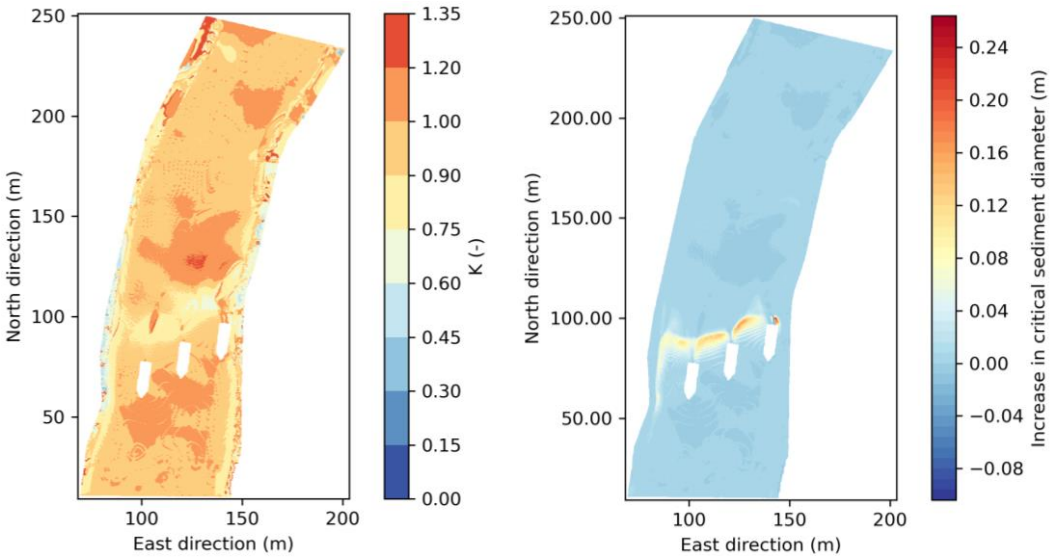

Figure 50 K and the corresponding increase in critical sediment diameter for $Q = 135 \frac{m^3}{s}$.

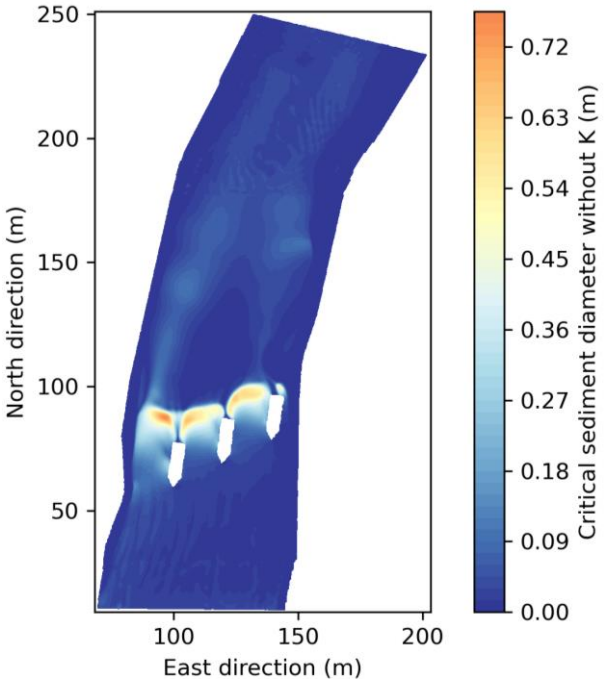

Figure 51: Critical sediment diameter without bed slope correction for $Q = 135 \frac{m^3}{s}$.

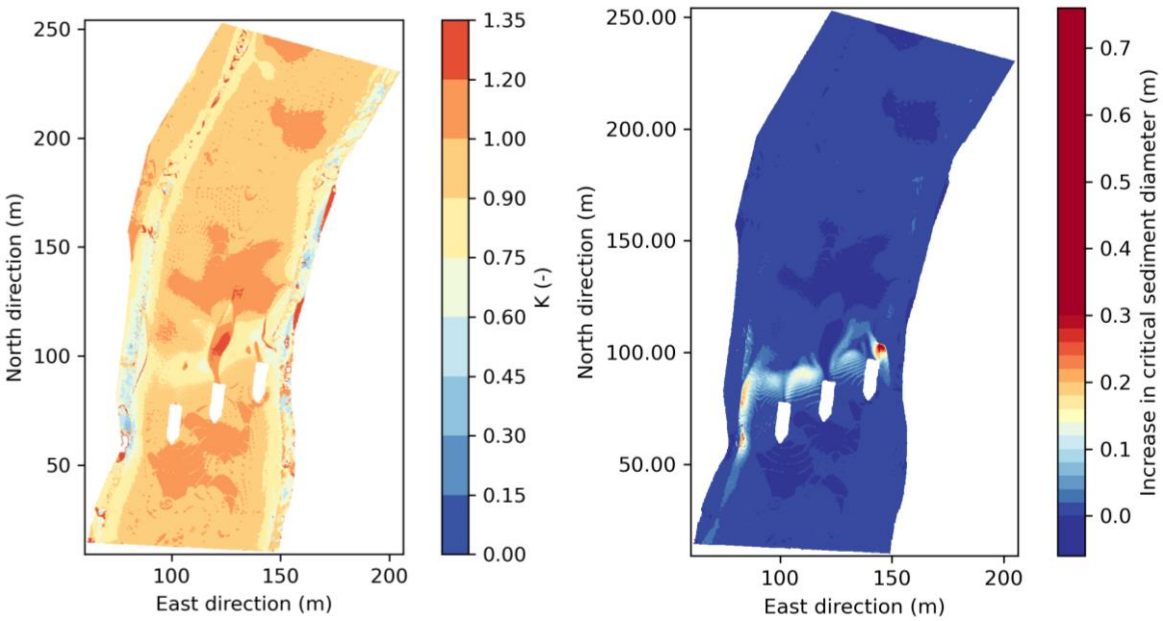

Figure 52: K and the corresponding increase in critical sediment diameter for $Q = 400 \frac{m^3}{s}$.

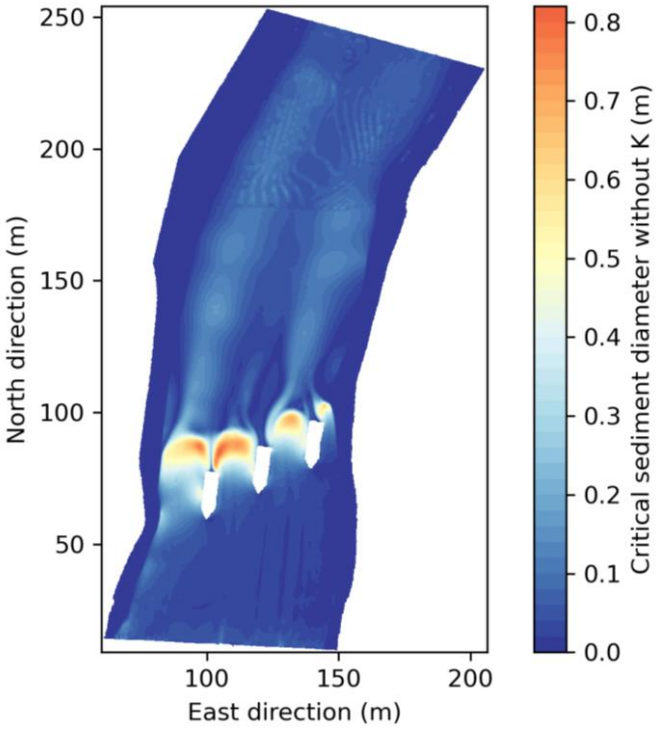

Figure 53: Critical sediment diameter without bed slope correction for $Q = 400 \frac{m^3}{s}$.

4.2.2 Comparison with scour protection regulations

The D_{50}- and D_{max}-value based on scour protection regulation is computed for each discharge in Table 12 (Equation (2.7)). The velocity is retrieved 0.5 m from the upstream edge of the middle pier.

Table 12: Critical sediment diameter based on the scour protection regulation.

Discharge (m^3/s)	Velocity (m/s)	D_{50} (m)	D_{max} (m)
85	1.23	0.08	0.16
135	1.19	0.07	0.14
400	1.95	0.2	0.4

The extent of the scour protection can be calculated using equation (2.6). The minimum extent of the scour protection to all sides of the piers is:

$$L_{protection} = (5\,m + 18\,m \cdot \sin(15)) \cdot 2 \; = 19\,m. \tag{4.1}$$

4.2.1 Convergence

Figure 54 to Figure 59 show the inflow and outflow over time. Both the simulations with fine mesh and coarse mesh are plotted. The outflow varies greatly at the beginning of the simulation. Eventually, the outflow stabilizes but to a lower discharge than the inflow. The inflow varies slightly in the beginning and stabilizes quickly. However, the inflow does not reach the user-specified inflow discharge. This is visible in Figure 59, where the inflow is less than $Q = 400\frac{m^3}{s}$. Figure 60 to Figure 62 show the water surface for two different times for the simulations with fine mesh. The free surface and riverbed are plotted along the west slice (Figure 33). It is observed that the free surface is approximately steady for all discharges. Figure 63 shows the water surface at two different times for the simulation with $Q = 135\frac{m^3}{s}$ and a coarse mesh. This figure is included to show that the simulations with coarse mesh also reach a quasi-steady state, despite the difference between the inflow and outflow in Figure 54 to Figure 59.

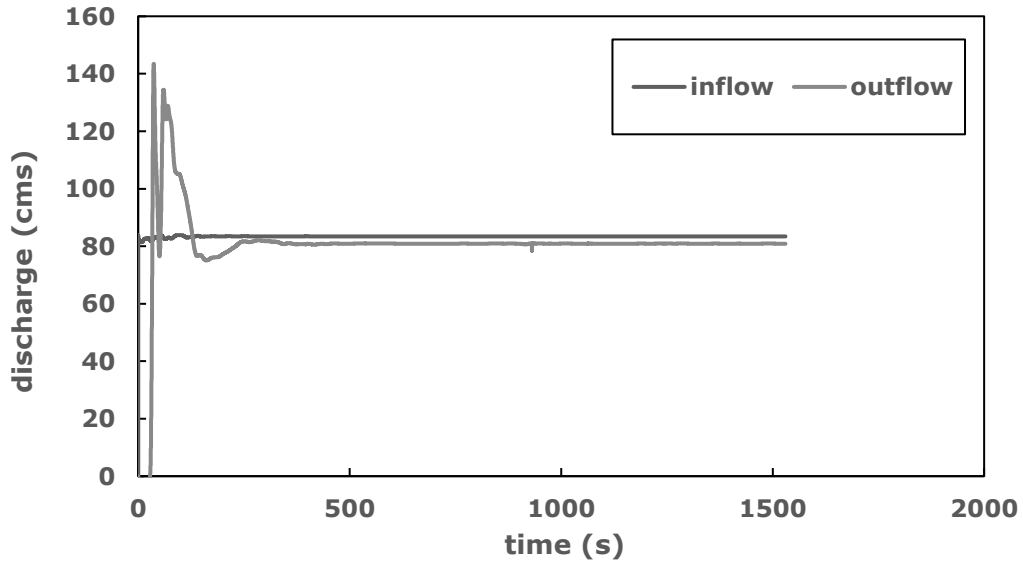

Figure 54: Inflow and outflow for $Q = 85\frac{m^3}{s}$ with a coarse grid.

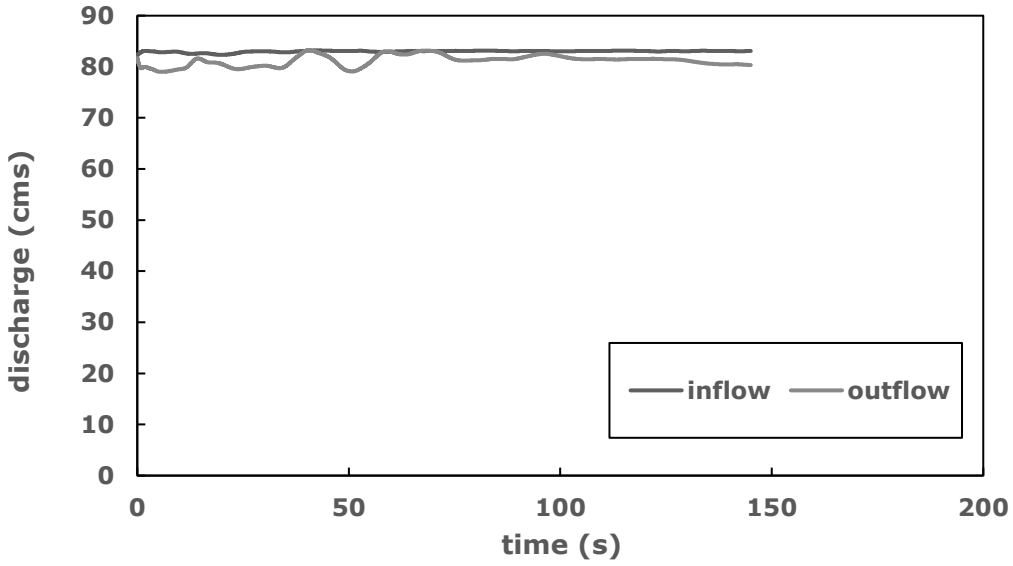

Figure 55: Inflow and outflow for $Q = 85\frac{m^3}{s}$ with a fine grid.

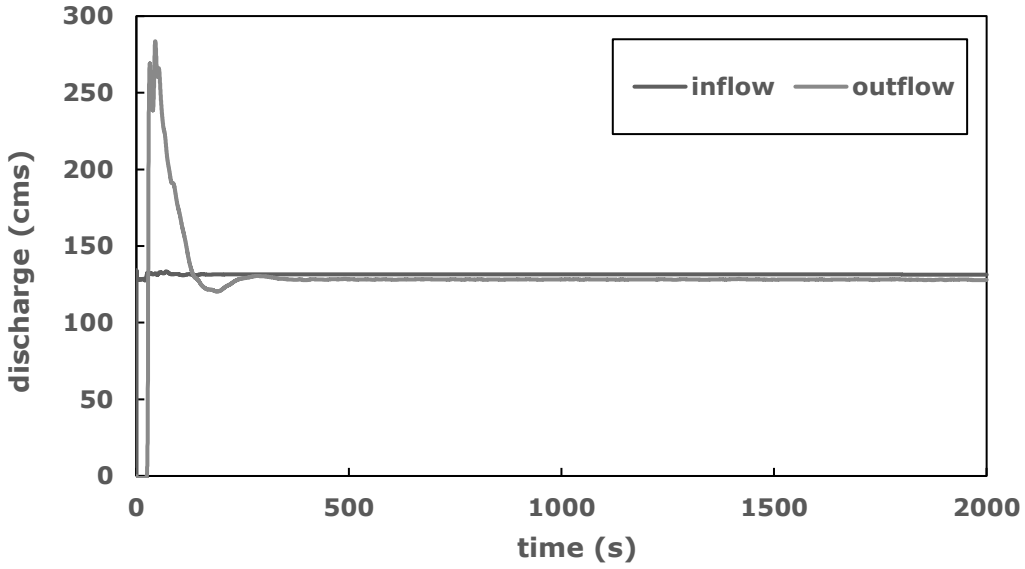

Figure 56: Inflow and outflow for $Q = 135\frac{m^3}{s}$ with a coarse grid.

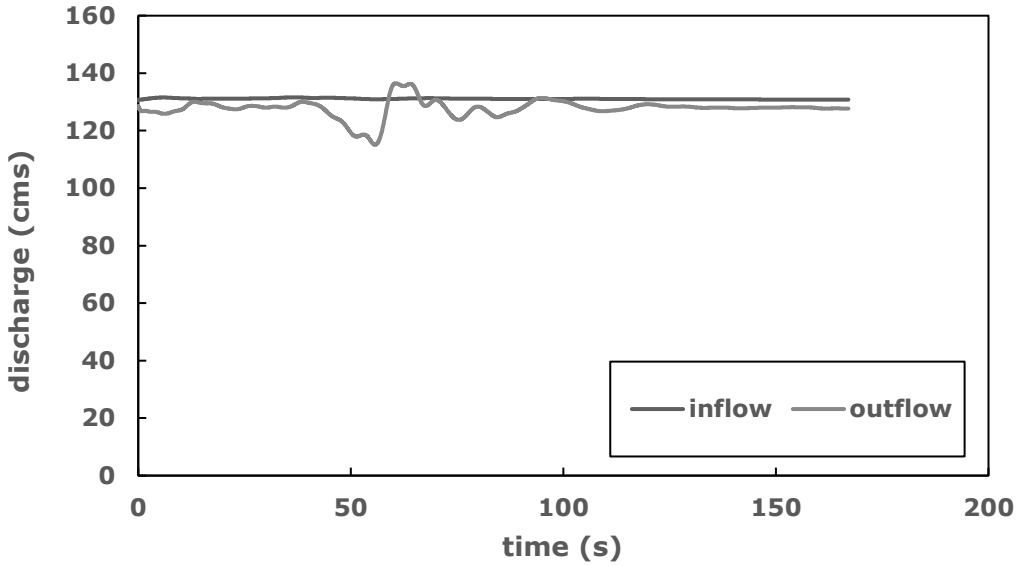

Figure 57: Inflow and outflow for $Q = 135\frac{m^3}{s}$ with a fine grid.

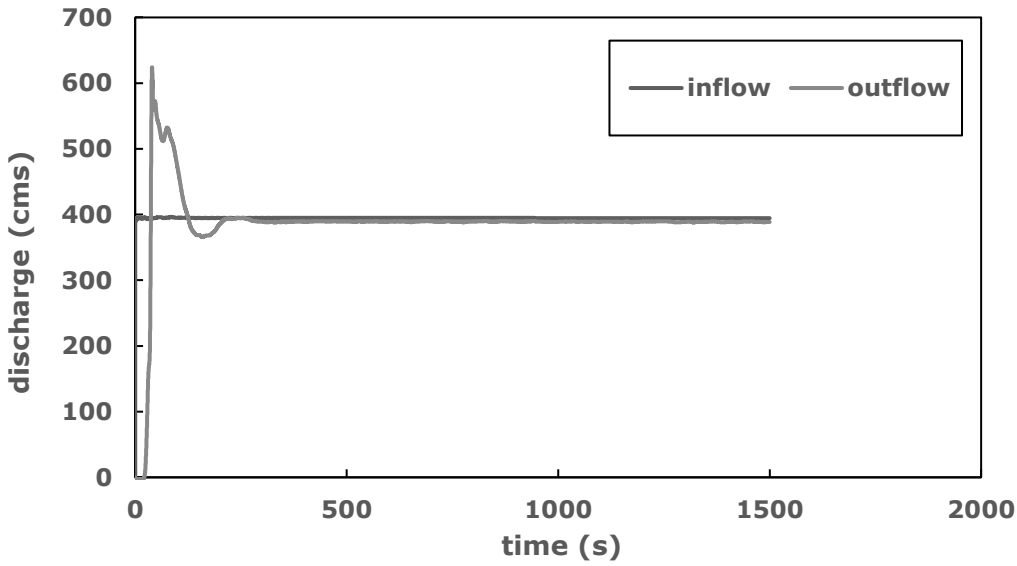

Figure 58: Inflow and outflow for $Q = 400\frac{m^3}{s}$ with a coarse grid.

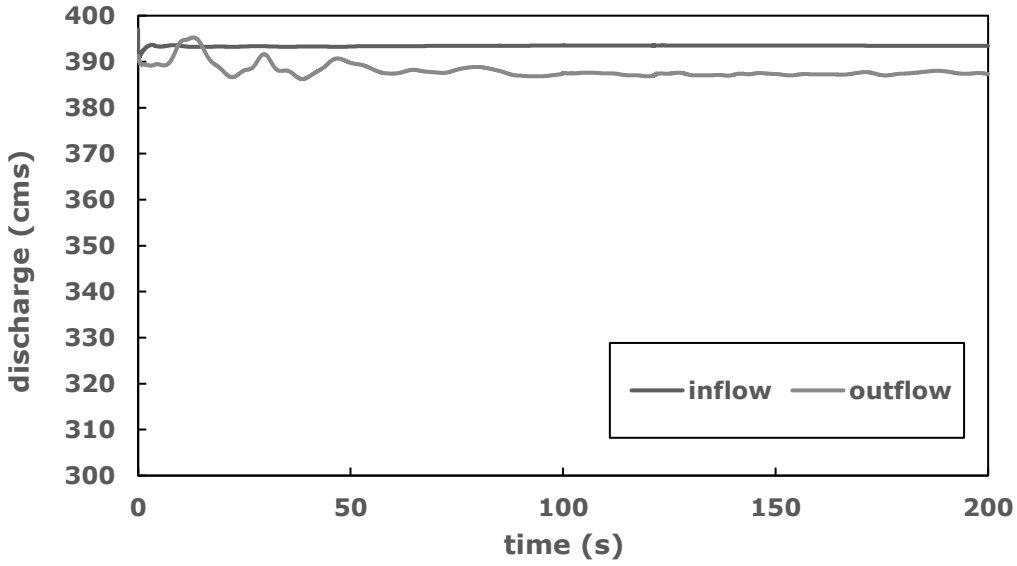

Figure 59: Inflow and outflow for $Q = 400 \frac{m^3}{s}$ with a fine grid.

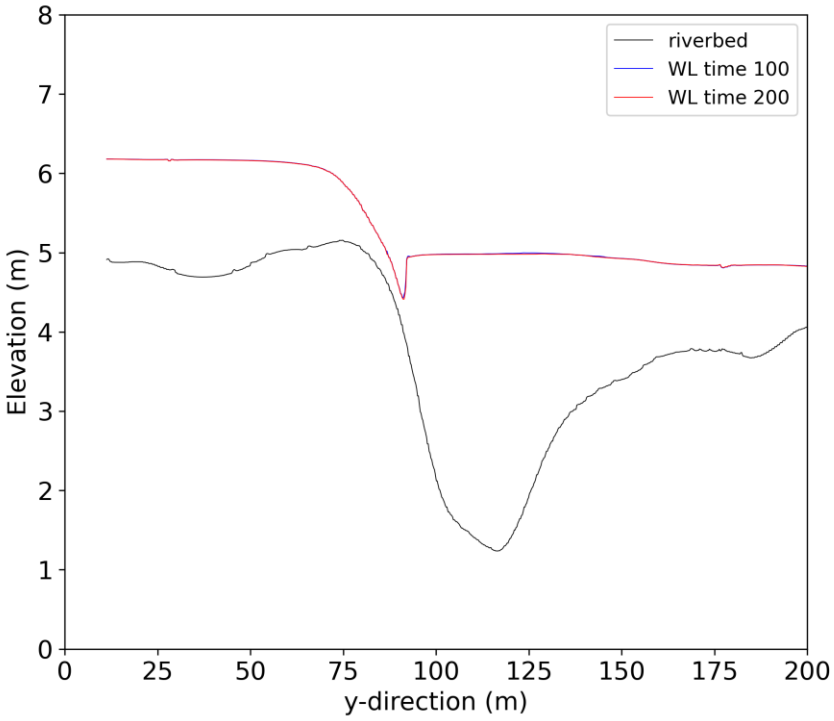

Figure 60: The free surface after 100 and 200 simulated seconds for $Q = 85 \frac{m^3}{s}$ with a fine mesh.

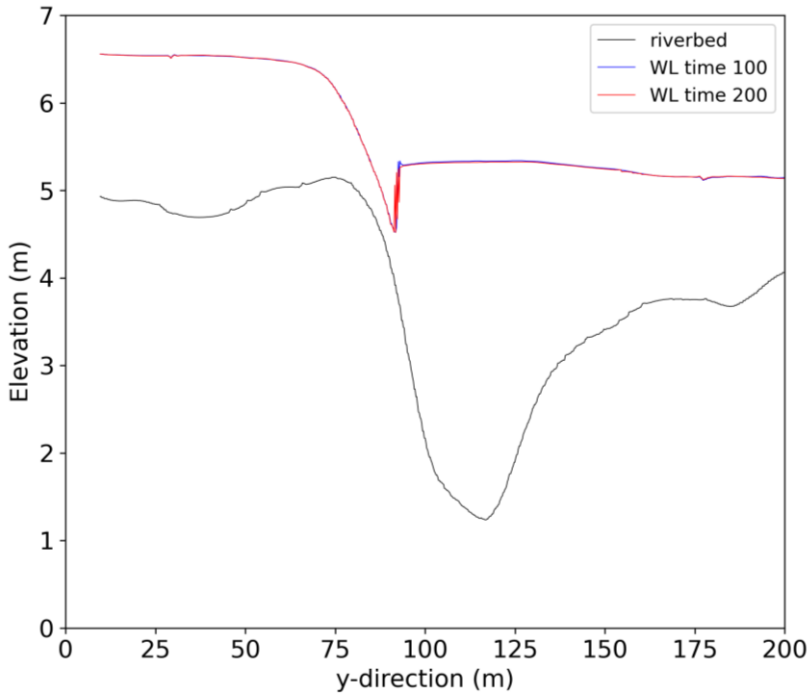

Figure 61: Free surface after 100 and 200 simulated seconds for $Q = 135 \frac{m^3}{s}$ with a fine grid.

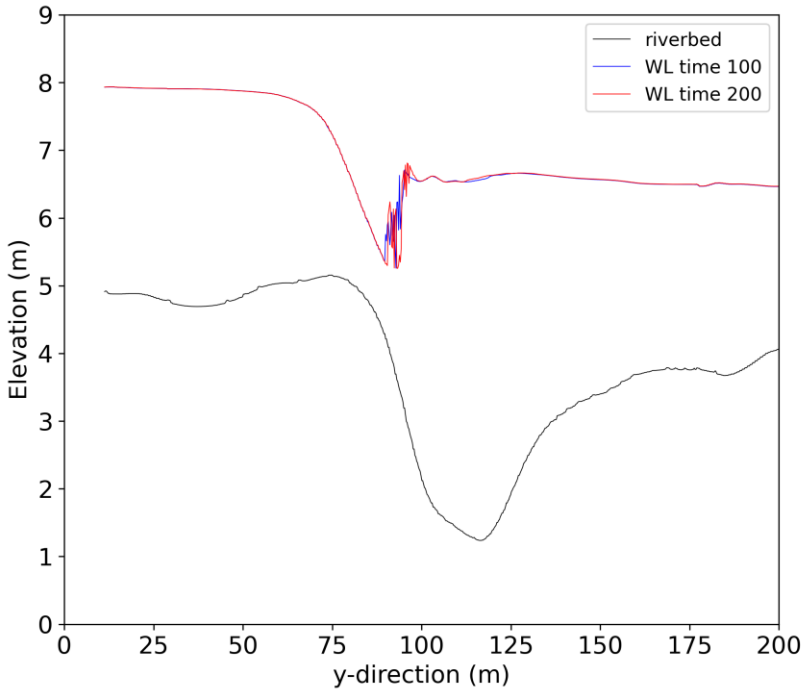

Figure 62: Free surface after 100 and 200 simulated seconds for $Q = 400 \frac{m^3}{s}$ with a fine grid.

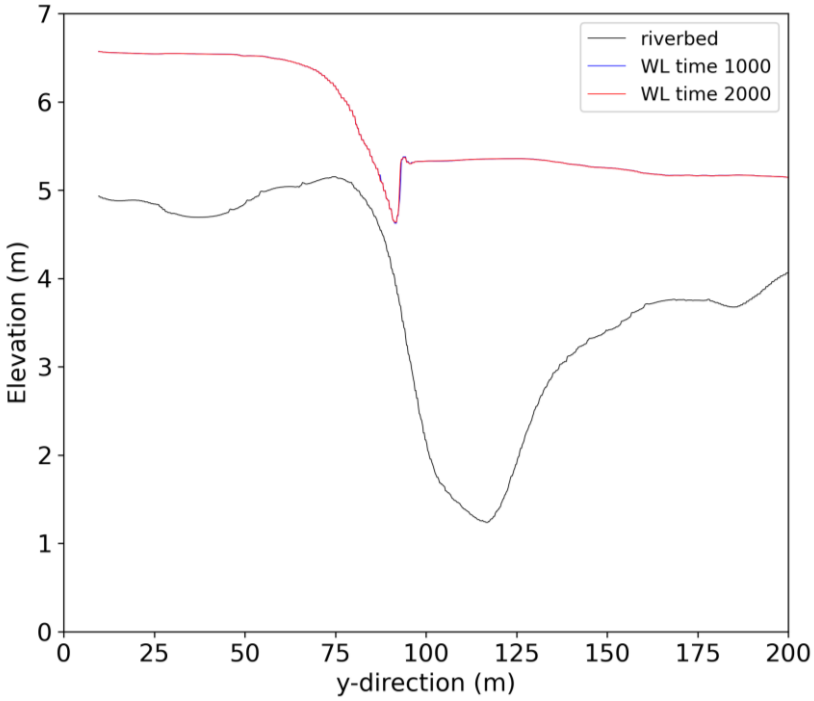

Figure 63: The free surface after 1000 and 2000 seconds for $Q = 135 \frac{m^3}{s}$ and a coarse grid.

4.3 Results of physical modelling

Several configurations of stones are made in the physical model. The most promising formations are shown in Figure 64. A line of stones is placed between the piers. A plank, representing a kicker, is located downstream of the line. The line of stones is located downstream of the piers (left photo in Figure 64) and further upstream (right photo in Figure 64). Both the upstream and downstream location is tested between each pier.

Figure 65 to Figure 68 shows the wave for the downstream and upstream positions between the middle pier and the upstream pier. Figure 65 and Figure 66 show the wave and the configuration of the stone line and the kicker from above. One configuration consists only of the line of stones, and the second is made of stones and a downstream kicker. Figure 67 and Figure 68 show the wave created by the stone line with and without a downstream kicker from the side.

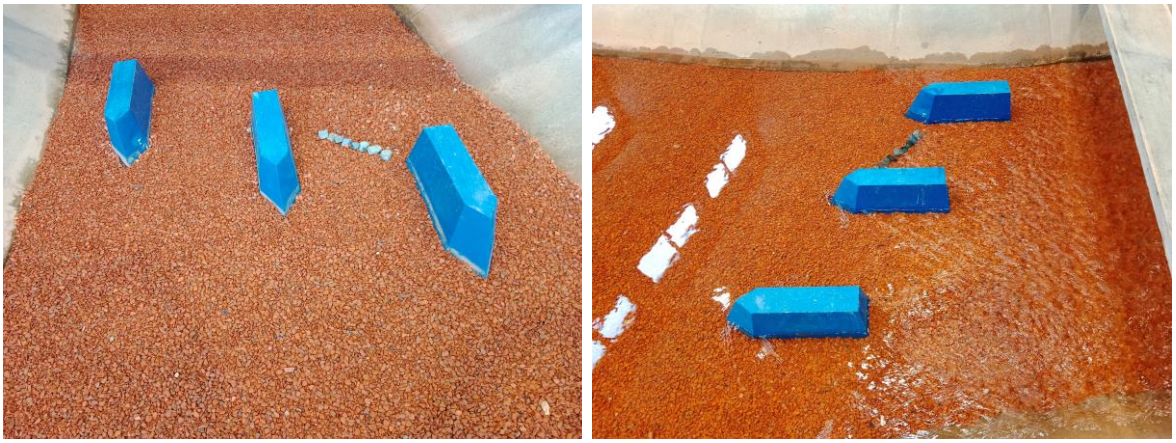

Figure 64: Configuration of stones at the downstream and upstream position

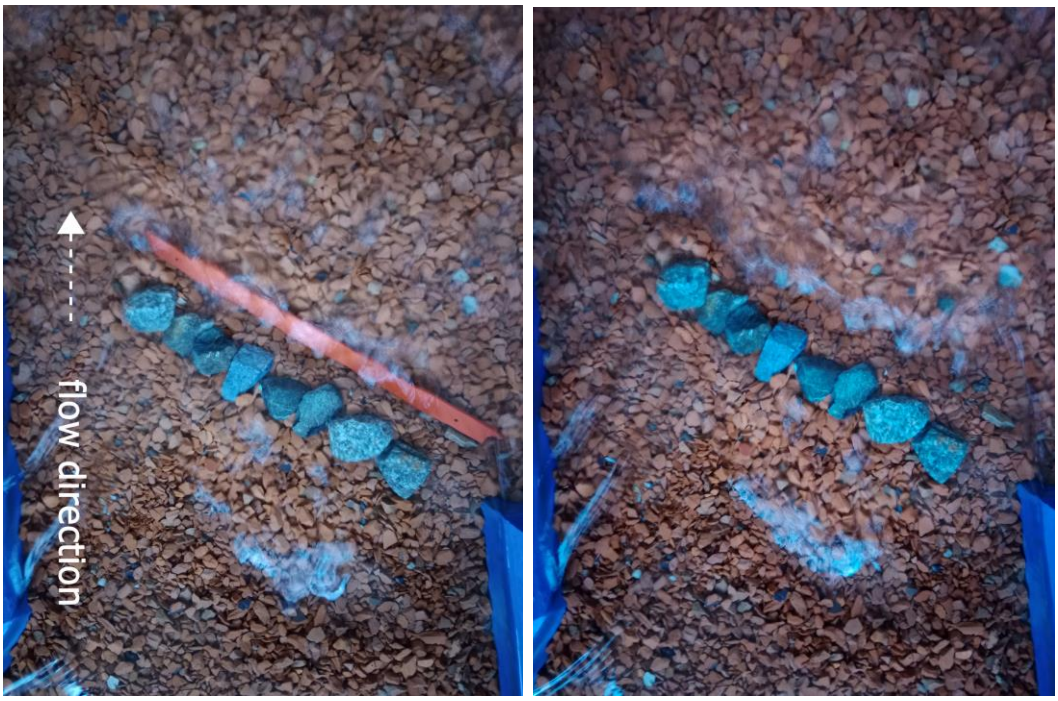

Figure 65: Wave with and without a kicker plank, downstream position.

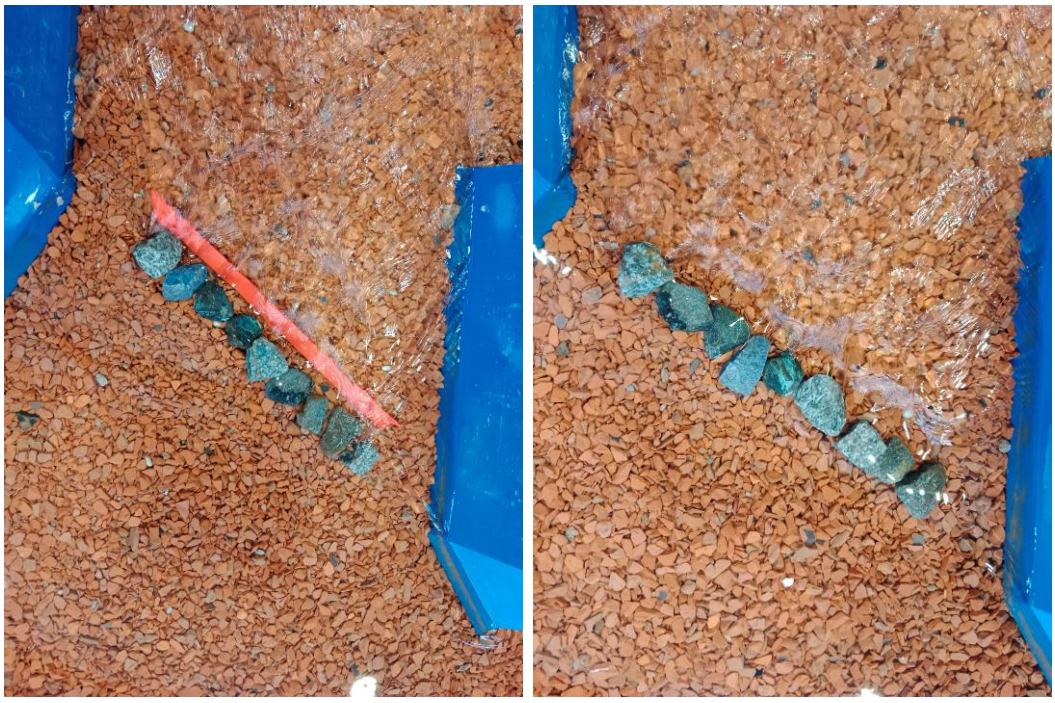

Figure 66: Wave with and without a kicker plank, upstream position.

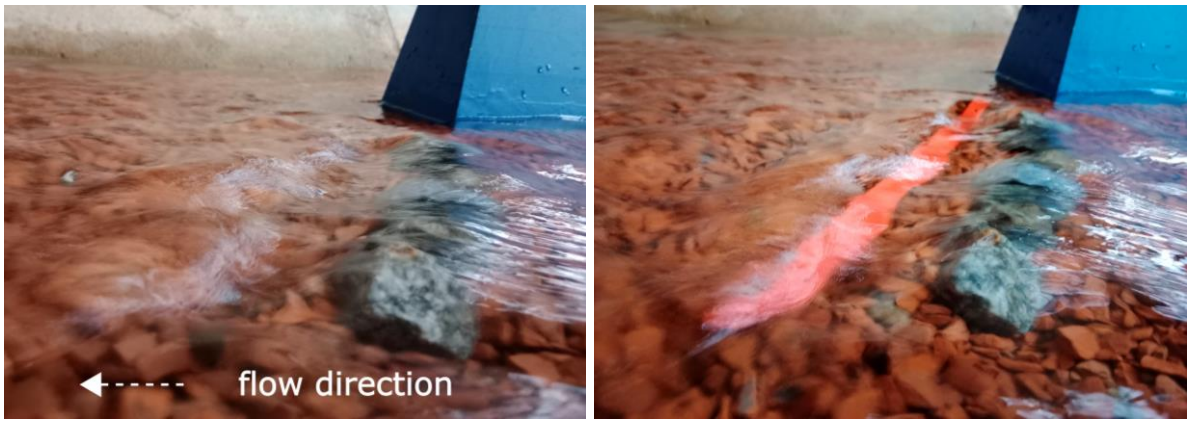

Figure 67: Wave with and without a kicker plank, downstream position.

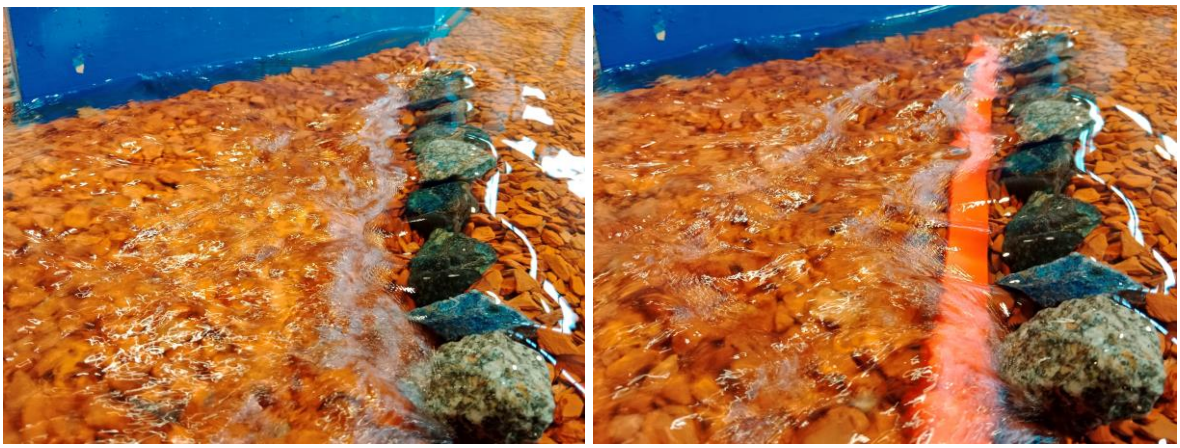

Figure 68: Wave with and without a kicker plank, upstream position.

The lowest water depth is above the stones and is in the magnitude of 0.5 cm. In addition, no air-entrainment takes place. Assuming a representative water depth of 0.02 m in the simulation with a discharge of $Q_m = 22\ \frac{l}{s}$, the estimated cross-sectional area is 0.04 m^2 and the average velocity is 0.55 $\frac{m}{s}$. The Reynolds number becomes:

$$R_e = \frac{u \cdot y}{\nu} = \frac{0.55 \cdot 0.02}{10^{-6}} = \ 1.1 \cdot 10^4\ (-)\ . \tag{4.7}$$

Despite the lack of visible air-entrainment, the upstream front of the wave created by the stone configuration without a kicker is slightly steeper and higher than the wave front created by the configuration with a kicker (Figure 67 and Figure 68). The wave is parallel to the line of stones, and the wave is not wider than the line of stones (Figure 65 and Figure 66).

5 Discussion

5.1 Two-dimensional channel simulation

5.1.1 Numerical roughness

The presented methodology in section *3.3.2 Roughness calibration* aims at relating k_s to K_{st} in a two-dimensional channel. 15 different cases are simulated with unit discharges of $q = 1\frac{m^3}{s}$ and $q = 2\frac{m^3}{s}$ and 0.1m for $q = 5\frac{m^3}{s}$ and k_s -values varying according to Table 4. The height of the cells closest to the riverbed is equal to 2 times k_s.

The free surfaces of the cases of $k_s = 0.001\,m$ differ from the simulations with higher k_s-values. The sampled depths 300m downstream of the inlet of the cases of $k_s = 0.001\,m$ are either close to or below the critical depth. Therefore, it is likely that the lowest depths are below the critical depth and the differences in the free surfaces compared to the free surfaces of other simulations are caused by hydraulic jumps.

The 15 simulations (Figure 19, Figure 20 and Figure 21) yielded a relatively stable β-value (equation (3.6)) for most cases. Excluding the case of $k_s = 0.001\,m$, the average β-value is $24.1\,m^{0.5}/s$ with a standard deviation of the sample of 0.86 $m^{0.5}/s$ (Table 9) for the remaining k_s -values and all discharges.

The result of the β-value in this study differs from the experimental form of equation (2.12) (Meyer-Peter & Müller, 1948) and previous applications of equation (2.12) in numerical modelling. Almeland et al. (2018) uses $k_s = 0.0017$ m to simulate $K_{st} = 90\,m^{\frac{1}{3}}/s$, and Richter et al. (2021) uses $k_s = 0.3\,m$ to simulate $K_{st} = 32\,m^{\frac{1}{3}}/s$. However, if $\beta = 24.1\,m^{0.5}/s$ were applied, the respective k_s-values would become $k_s = 0.0004\,m$ and $k_s = 0.18\,m$ for $K_{st} = 90\,m^{\frac{1}{3}}/s$ and $K_{st} = 32\,m^{\frac{1}{3}}/s$. It must be noted that neither of the above-mentioned articles used interFoam. Chen et al. (2021) proposes $\beta = 21.6$ for interFoam, which differs from the result of this study.

5.1.1 First cell height

Two restrictions on the height of cells closest to walls were presented in section *2.2.3 Height of cells closest to walls.* The first restriction proposes that the height of cells closest to walls should be 2 times k_s (Blocken, Stathopoulos, & Carmeliet, 2007). The second restriction proposes that cells closest to walls should be located in the log-law region with a y^+-value between 30 and 500 (Versteeg & Malasekera, 2007). These restrictions are difficult to combine (Figure 26, Figure 27, Figure 28). Only the case of $k_s = 0.001\,m$ succeeds fulfilling both criterions because the first cell center is located in the log-law region and is 2 times k_s. However, this k_s-value corresponds to a K_{st}-value too high for natural rivers. Therefore, fulfilling both criterions is difficult for typical K_{st}-values of natural rivers.

Figure 31 shows that the restriction of to 2 times k_s does not necessarily need to be fulfilled: the first cell height being 0.5 times k_s produces the same free surface as when the first cell height is 2 times k_s. However, when the first cell height is reduced to 0.1 times k_s, the results change. This effect might be caused by a change in the k_s^+-value and y^+-value, but further investigation is needed.

5.1.1 Simulated shear stresses

Figure 22 shows the simulated shear stresses (equation (2.31) and equation (2.35) and the theoretical shear stress assuming uniform flow (equation (2.9)). Table 10 shows that the simulated shear stresses and the theoretical shear stress 300m downstream of the inlet are closely related. This shows and verifies the application of shear stress from CFD simulation for hydraulic engineering.

Table 10 also shows that the shear stress based on the utility *wallShearStress* (equation (2.35)) predicted the uniform shear stress slightly better than the shear stress based on the turbulent kinetic energy (equation (2.31)). The turbulent kinetic energy must be sampled in the cell closest to the bed and is more difficult to post-process than the *wallShearStress* utility.

5.1.1 Froude number

A post-processing tool of the Froude number is developed and tested on a two-dimensional channel simulation. A separate calculation of the Froude number, which utilizes the simplicity of a two-dimensional channel, is used to control the code of the Froude number. The post-processing tool of the Froude number and the control of the Froude number produces similar results. This verifies the post-processing code of the Froude number. The post-processing code of the Froude number can output the Froude number for a varying riverbed along a slice of the domain. The Froude number is widely used to evaluate and categorize free surface phenomenon, but to the author's knowledge, this tool is not yet publicly available for interFoam.

5.1.1 Convergence

The water depth is for each case plotted at the end of the simulation and 500 seconds before the end of the simulation (Figure 23, Figure 24 and Figure 25). The flow has reached a steady state and the water level is stable over the last 500 seconds of the simulation. It is assumed that the plots of the water level are sufficient to show convergence. In addition, the similarity between the theoretical shear stress and the simulated shear stresses 300m downstream of the inlet indicates that the simulations have reached a steady uniform flow in the upstream part of the channel. However, the inflow and outflow are not monitored, and no convergence criteria are applied.

5.2 Scour model

The scour model in its simplicity, consists of 1) retrieving the shear stress at the riverbed from a CFD simulation, 2) computing the bed slope correction factor and 3) computing the critical sediment diameter that balances the equation: the dimensionless critical shear stress is equal to the bed slope corrected, non-dimensional critical shear stress. Points 1), 2) and 3) are discussed below.

1. The shear stress is retrieved from the interFoam simulation using the utility *wallShearStress*. Figure 22 shows that the shear stress retrieved from this utility closely resembles the theoretical shear stress of uniform flow. This shows the applicability of *wallShearStress* to hydraulic engineering. However, the utility is not verified on a three-dimensional simulation. Furthermore, simulating accurate shear stresses is dependent on resolving the flow field accurately. Small-scale eddies, such as horseshoe-vortices, demand a fine mesh to be resolved accurately.

2. The formula of the bed slope correction, equation (2.5), is chosen instead of equation (2.3) because equation (2.3) includes the factor 0.954. For a horizontal riverbed, equation (2.3) returns the value 0.954 because of this factor. This is not preferable, because the dimensionless critical shear stress is valid for horizontal beds and should not be reduced further. The use of bed slope correction is well established and used in multiple studies (e.g., Bihs and Olsen (2011)). The code of the bed slope correction factor has been verified on a two-dimensional channel simulation in section *3.3.1 Verification of bed slope correction*. There are no differences between the control calculation and the bed slope (Table 11). However, the verification lacks a test where the velocity vector is not aligned with the structured grip points.

3. Most articles implementing sediment transport rate models, which were read by the author of this thesis, use a formulation of the bed load which depends on the dimensionless critical shear stress and the dimensionless critical shear stress (Table 1). This made the way short to determine the critical sediment diameter based on these two parameters. While many studies use a formula for calculating the dimensionless critical shear stress based on the velocity near the riverbed, a simplified method has been implemented: the dimensionless critical shear stress is constantly equal to 0.045. This method has also been used in sediment transport rate models (Rüther, Singh, Olsen, & Atkinson, 2005). This method of computing the critical sediment diameter is also discussed in the Norwegian scour protection regulations (Jenssen & Tesaker, 2009).

The proposed scour model has limitations compared to existing models: two-phase Euler-Euler scour models might provide a better estimate of scour under sheet flow with high sediment concentration. CFD-DEM models have the advantage of further describing sediment-flow interaction and have the potential of modelling scour using different sediment shapes and sizes. Standard sediment transport rate models can reveal increased scour on new locations as the scour propagates and the riverbed is updated. The advantage of the applied model is the computational efficiency and its simple application – the scour model is applicable as a post-processing tool of three-dimensional interFoam simulations.

5.3 Numerical simulation of Nidelva at Sluppen bridge

5.3.1 Numerical errors

The numerical simulation is a mathematical representation of nature and will not describe nature correctly. The following discussion is based on section *2.2.4 Errors in numerical modelling*.

1. Modelling errors include the use of the RANS equations, which does not fully capture the unsteady nature of turbulent flow: one can argue that scour is related to the peak of the velocity fluctuations rather than a velocity average.

2. Numerical approximation errors include the use of a relatively coarse grid, cells not aligned to the stream direction, and the use of lower-order schemes.

   The finest grid size of the hexahedral cells is approximately $0.4 \cdot 0.4 \cdot 0.1\, m^3$, which for standard CFD modelling is coarse. The large size of the domain and the computational capacity limits the finest grid cells. However, the simple refinement

method: the cell size in each direction inside a user-specified box is 50% of the cell size outside the box (Figure 16) could have been improved using a more advanced refinement technique such as adaptive mesh refinement or a more advanced geometry of the refined region. Improved refinement methods could potentially reduce the cell sizes in the region of interest without excessively increasing the total number of cells. However, the Courant number will be increased by a finer grid independent of the refinement method.

Also, increasing the computational capacity will decrease the computational time and facilitate for a finer mesh. However, at a given number of processors, increasing the number of processors does only negligible decrease the computational time, but the 39 processors used in this thesis are likely not near this limit. Finally, reducing the domain is an easy way of reducing computational costs. To the author's knowledge, most CFD studies of piers are performed on only one pier, which enables the grid to be much finer. A similar approach could have been implemented by studying only the flow between two half piers or having one pier in the middle and two half piers on each side of the domain. However, it would be harder to define the upstream inflow, and the inflow and outflow from the sides of the domain would be more difficult to simulate if only parts of the piers are simulated. It can also be argued that the lengths from the piers to the inlet and the outlet are too large, and reducing these distances would free computational capacity. To sum up, decreasing the cell size will normally reduce numerical approximation error and can be achieved by applying a more advanced refinement method, increasing the number and speed of the processors, or reducing the domain. The standard method of evaluating the effect of the cell size is to perform a grid independency analysis with a finer grid, but this has not been done in this study.

Cells not aligned to the stream direction can lead to numerical approximation errors. Figure 13 shows the horizontal extent of the background mesh in relation to the bathymetry. There are 3 blocks in the stream direction aiming at aligning the background mesh direction with the stream direction. Figure 14 shows that the background mesh has the same elevation over the entire length. The 3 blocks shown in Figure 13 align the mesh to the stream direction with acceptable accuracy. However, the piers obstruct the flow and guide the flow around and in between the piers. The flow change induced by the piers is not aligned with the background mesh.

Furthermore, Figure 14 shows that the background mesh is not aligned with the stream direction when the flow velocities are not horizontal. The plots of the water surface profile (e.g., Figure 34) show that the surface, and thus, the flow velocities are not horizontal between the piers and downstream of the piers. In addition, the riverbed bathymetry is not horizontal - especially near the scour hole. The flow velocity vectors near the bed are parallel to the riverbed, and thus, the flow direction is not aligned with the background mesh. The background mesh is created using blockMeshDict, which for an inexperienced user is not so intuitive. An alternative is an additional software to create a more advanced background mesh. SALOME (OPEN CASCADE, EDF, CEA, 2022) is an open-source software that enables the user to create complex background meshes. SALOME is often utilized by OpenFOAM-users. To sum up, the background mesh is aligned with the stream direction using 3 blocks in the stream-direction (Figure 13), but the change in flow

direction due to the piers are not aligned with the cell direction. In addition, all cells are horizontal (Figure 14) and not aligned with non-horizontal velocity vectors.

Lower-order schemes can also introduce numerical approximation errors. The first-order scheme Gauss upwind is used for the divergence terms *div(phi, k)* and *div(phi, epsilon)* and the first-order scheme Euler is used for the time dimension. It is not evaluated how higher-order schemes would affect the solution.

3. Errors due to wrong boundary conditions and input data include errors in the bathymetry measurements, the geometry of the piers, the pre-processing of the bathymetry measurements, and the boundary conditions of the riverbed roughness, the inlet, and the outlet.

   First, the measurements from the site contain errors. While the ADCP measurements from SWECO have relatively many measurement points, the bathymetry from NTNU is coarse. The coarse bathymetry from NTNU has clear errors compared to the finer measurements from SWECO in the same location. In addition, the geometry of the piers is made from drawings created in 1976. These drawings are not controlled. Any errors in the drawings or changes of the piers since 1976 are not considered in this thesis.

   One step of the pre-processing of the bathymetry is smoothing the terrain to increase numerical stability. However, it is possible that the geometry was smoothed out too much, losing features of the prototype terrain. This was especially the case for the smoothing of the geometry in the direction normal to the flow. This smoothing limit the cross-sectional area in the direction normal to the flow. The reduced cross-sectional area increases the flow-obstruction induced by the piers. The upstream water level increases and the head between the upstream and downstream water levels increases. This causes the velocities, Froude numbers and critical sediment diameters to increase in between and downstream of the piers. Figure 40 shows that the simulated upstream water level is too high compared to observations. This effect could have been reduced by reducing the smoothing of the terrain.

   The boundary condition of the riverbed is an abstraction of nature. The k_s-value, which describes the roughness of the bed using the boundary condition *nutkRoughWallFunction* has been related to the Manning-Strickler number in the two-dimensional channel simulations. However, the Manning-Strickler number in the simulation of the Sluppen bridge piers is only chosen based on the experience of natural rivers and is not based on in-situ sediments. To the author's knowledge, there exist no measurements of the sediments at the site, which makes the determination of a realistic roughness value difficult. Furthermore, the piers are likely surrounded by scour protection and the roughness in nature has a spatial variability which is not considered with the constant k_s-value. Using one- or two-dimensional simulation of the river with hydraulic software (e.g., HEC-RAS), and calibration of the Manning-Strickler number could provide further knowledge about the roughness, but also this method is flawed. The higher geometric accuracy in the three-dimensional simulation provides roughness that is not captured in simulations with fewer dimensions. Thus, calibrated roughness values in simulations with fewer dimensions can be higher than corresponding well-calibrated roughness values in three-dimensional CFD simulations. Figure 40 shows that the simulated

upstream water level is too high, which could have been adjusted by decreasing the k_s-value.

Figure 26, Figure 27 and Figure 28 indicate that keeping y^+-values of the grid nodes closest to walls in the log-law layer while satisfying the criterion of the height of the first cells being 2 times k_s is difficult for typical k_s-values of natural rivers. The figures are from the two-dimensional simulation, but the trend is assumed to hold also for the simulation of the Sluppen bridge piers. While wall functions should satisfy the y^+-criterion, this is not done in this study and the effect of this is not evaluated. However, it is seen that multiple studies, such as Hoff et al. (2010), accept high y^+-values when using high k_s-values.

The inlet and outlet boundary conditions are also erroneous. A riverbend is located approximately 200m upstream of the bridge (Figure 1). The inlet boundary condition does not consider the upstream bend in the river. The bend might cause a non-uniform velocity profile along the width of the channel.

The water level at the outlet is fixed by using a constant value for *p_rgh* at the outlet of the water phase and a fixed value equal to 0 in the air phase. This boundary condition performed acceptable in the three-dimensional simulation of flow around Sluppen bridge piers: the outlet water level did not vary, and the simulations converged well. However, it is not clear how the dynamic pressure, $0.5 \cdot \rho \cdot U^2$, affect the pressure at the outlet or how the large gradient of *p_rgh* between the water and air phase affects the simulation. Like the inlet boundary condition, the velocity profile along the width of the channel might be affected by river geometry outside of the investigated domain. The fixed water depth at the outlet is retrieved from the one-dimensional HEC-RAS model. Figure 40 shows that the outlet water level used in the simulation of the Sluppen bridge piers is lower than the measurement from the site. This impacts the flow velocities in between the piers and increases the critical sediment diameter because the head between the upstream and downstream water levels are too high. In addition, a too low outlet depth moves the hydraulic jump downstream and enlarges the area of increased sediment diameters. Further calibration of the outlet depth is needed.

4. A lack of knowledge of how to conduct a CFD study can lead to errors. The author had around 15 hours of previous experience using OpenFOAM, and no other CFD software. The author has attended the classes Numerical calculations TKT4140 (NTNU, 2020) and Numerical models and hydraulics TVM4155 (NTNU, 2020), but to sum up, the experience of the user is scarce.

5. Bugs in the software can lead to errors. This error source is likely smaller than the above-mentioned error sources since OpenFOAM is an established software.

6. Lack of convergence can lead to errors. The inflow, outflow and water level are monitored for each simulation (Figure 54 to Figure 63). The convergence of the discharge shows a slight discrepancy between the inflow and the outflow throughout the simulation time. It is believed that this is a sampling error rather than a lack of convergence for the following two reasons: 1) the sampling of the inflow differs from the specified inflow input in the boundary condition of the inlet and 2) the plots of the free surface show only small changes despite a constant difference between the inflow and the outflow. This is especially visible in Figure 63, where

there are almost no changes in the water level despite a difference in inflow and outflow (Figure 56) over 1000 seconds. A disadvantage of this study is that the shear stress at the riverbed is not monitored over time. Since the shear stress is the primary output, this field should have been used to control convergence.

5.3.1 Calibration

Figure 40 and Figure 41 show simulated water levels and observed water levels. The simulated water levels are plotted along the west and east slice (Figure 33) for $Q = 135\frac{m^3}{s}$ in Figure 40 and Figure 41, respectively. The observed water levels are measured along the east bank by SWECO for $Q = 124.6\frac{m^3}{s}$ and NTNU for $Q = 142.4\frac{m^3}{s}$. The measurements show good agreement between themselves, despite a difference in discharge. However, the simulated water depth is too high upstream of the piers and too low downstream of the piers. The calibration should be performed by:

1) Increasing the outlet depth in the outlet boundary condition by approximately 0.2m.
2) Reducing the smoothing of the DEM of the bathymetry. This would increase the volume available for the water below the water level and decrease the upstream depth.
3) Decreasing k_s if point 2) does not reduce the upstream depth enough.

5.3.2 Hydraulic jump

Figure 34 to Figure 39 shows the water surface profiles between each pier for each discharge and the corresponding Froude numbers. The Froude numbers can be used to verify the simulation and to evaluate how a surf wave can be recreated.

The hydraulic jump is formed downstream of the piers. This is similar to the hydraulic jump in the prototype, as shown in Figure 4. The flow is subcritical upstream of the piers, supercritical between the piers and subcritical downstream of the piers with a recirculation zone behind the piers. This behaviour is also observed in the prototype (Smith, N. S., personal communication, 2022). The maximum Froude number is approximately 2 for all discharges. This corresponds to a weak hydraulic jump. The hydraulic jump downstream of the piers is subcritical in both the simulation and prototype. Therefore, the wave is not suitable for surfing (Figure 6).

5.3.3 Critical sediment diameter

The critical sediment diameters are shown in Figure 45, Figure 46 and Figure 47. The highest values are located downstream of the piers. The critical sediment diameters are larger between the two most upstream piers than the two most downstream piers. In addition, the critical sediment diameter is high between the downstream pier and the east bank.

The jets formed between the piers are more separated for larger discharges. This is especially visible for $Q = 400\frac{m^3}{s}$ (Figure 47). The jet between the two most downstream piers is separated by the recirculation zone behind the middle pier and the recirculation zone downstream of the jet between the most downstream pier and the east bank. The recirculation zone downstream of the middle pier has a length of approximately 50m. Furthermore, the jet between the downstream pier and the east bank is pointing inwards towards the river. These two jets, the jet between the two most downstream piers and the

jet between the most downstream pier and the east bank, seem to meet at the location of the deepest scour hole. However, the simulated downstream water level for $Q = 135\frac{m^3}{s}$ is lower than the observed water levels and the simulated upstream water level is larger than the observed water levels. This error is likely also existing in the simulation with a discharge of $Q = 400\frac{m^3}{s}$, and could cause larger simulated jets than in nature.

The bed slope correction factors are shown in Figure 48, Figure 50 and Figure 52. The bed slope correction factors are mostly below 1 on the downhill slope towards the deepest parts of the scour hole, and above 1 on the uphill part of the scour hole. From a qualitative point of view, this seems correct. Also worth noting is the bed slope correction factor above 1 in the recirculation zone behind the middle pier in Figure 52. The velocities in the recirculation zone are pointing upstream towards the bridge. Since there is an uphill slope towards the bridge, the bed slope correction factor becomes above 1.

Figure 48, Figure 50 and Figure 52 does also show the increase in the critical sediment diameter due to the bed slope correction. The largest increases in critical sediment diameter are located where the bed slope correction is less than 1 and the shear stresses are large. The shear stress has a great influence on the increase in the critical sediment diameter. The largest increases in critical sediment diameter due to the bed slope correction are found in the same places as the maximum critical sediment diameter. Therefore, introducing a bed slope correction could prove to be necessary for the dimensioning of scour protection because of the potential to increase the largest critical sediment diameters.

The bed slope correction factor is low (0.6-0.7 (-)) between the downstream pier and the east bank, which produces a large increase in the critical sediment diameter for all discharges. This is especially the case for $Q = 400\frac{m^3}{s}$, where the increase in the critical sediment diameter is 0.76m. This is a large increase in the critical sediment diameter compared to the rest of the increases in the critical sediment diameter. Further sensitivity analysis of the bathymetry and the smoothing parameters are needed.

The code could be improved by only outputting a map of the critical sediment diameter where the river is located. The side banks in Figure 45, Figure 46 and Figure 47 are above the water level, but this is not easy to read from the figures.

5.3.1 Comparison with scour protection regulation

Equation (2.7) shows the formula for D_{50} based on the scour protection regulation, and D_{max} is 2 times D_{50}. Table 12 shows the computed D_{50}-value and D_{max}-value for each discharge ($Q = 85\frac{m^3}{s}$, $Q = 135\frac{m^3}{s}$, and $Q = 400\frac{m^3}{s}$). The computed D_{50}-values range from 0.07m to 0.2m and the D_{max}-values range from 0.14m to 0.4m (Table 12). The maximum critical sediment diameters from the CFD simulations range from 0.72m to 1.0m (Figure 45, Figure 46 and Figure 47). For a non-uniformly graded grain size distribution, the critical sediment diameter from the CFD simulations can be replaced by D_{60}. The D_{60}-values from the CFD simulations are exceeding both the D_{50}-values and the D_{max}-values based on equation (2.7). However, it is expected that the empirical equation should yield more conservative values than the more advanced CFD simulation. No measurements of the in-situ sediment have been performed, and it is not clear which calculation of the critical diameter is more representative of the site.

One explanation of the difference between the critical sediment diameters from the CFD-simulations and the equation (2.7) is the unorthodox geometry of the piers. The piers were built in 1864 and do not follow modern standards. Empirical equations, such as equation (2.7) are based on experiments. These experiments are made under certain conditions. If the geometry of the piers is too different from the piers in the experiments on which equation (2.7) is based, equation (2.7) might not be a good estimate of the critical sediment diameter.

The simulated velocity in front of the middle pier is used as input to equation (2.7). Thus, both equation (2.7) and the simulated critical sediment diameters (Figure 45, Figure 46 and Figure 47) are based on the CFD-simulation. Hence, several numerical errors can be ruled out as the explanation for the discrepancy between equation (2.7) and the simulated critical sediment diameters. For example, errors due to wrong boundary conditions and input data are likely not the cause of the discrepancy, because both equation (2.7) and the numerical simulation are based on the same boundary condition and input data. In addition, false diffusion smears out the result and causes a reduction of the local shear stress. Less false diffusion might increase the difference between equation (2.7) and the simulated critical sediment diameters even further. On the other hand, modelling error could have over-estimated the shear stresses compared to the velocity in front of the middle pier.

The length of the scour protection to all sides of the piers is 19m according to equation (4.). Figure 47 shows that the highest values of the critical sediment diameter are mostly inside the area of scour protection. However, the erroneous low downstream water level makes the hydraulic jump move downstream and is likely moving the area of high critical sediment diameters further downstream and away from the piers.

5.4 Physical model test

A qualitative physical model is presented in section *3.5 Physical model test of Nidelva at Sluppen* bridge and pictures of stone configurations are shown in *4.3 Results of physical modelling*. The aim of the physical model is to propose drafts of how to reestablish the surf wave under the Sluppen bridge.

It must be noted that the physical model test is qualitative. The physical model test has several error sources related to geometry and scale. The downstream scour hole was dug out after a few key numbers: maximum scour depth, location of maximum scour depth and start of scour hole. Thus, the scour hole and the bathymetry in the model contain large abstractions compared to the prototype. The outlet water depth was adjusted so the hydraulic jump would be located downstream of the piers, but the water level is not controlled against measurements. The model embankments and upstream riverbend could not be changed and are not representative of the prototype.

The flow is turbulent, but below the recommended value of $2 \cdot 10^{-5}$ for physical models of open-channel flow with high air entrainment (Pfister & Chanson, 2014). The water depth above the line of stones is in the magnitude of 5mm, and below the recommended value of 2cm to avoid influential surface tension.

The tests indicate that a hydraulic jump can be formed by placing lines of stones or large sandbags between the piers. The current physical model revealed no differences between placing the line between the middle and the east piers, or between the middle and the west pier. The line was placed in between the piers in 2 locations: in the upstream part

and downstream part. There were no noticeable differences in the wave if the line was placed further upstream or downstream.

The kicker plank seemed to make the wave less steep. This could prove to be advantageous if the kicker can guide the supercritical flow upwards without creating a steep white-water hydraulic jump (Figure 6). The wave is relatively straight and parallel to the line of stones. This is desirable, as the surfers can utilize the width of the wave. The line of stone is not continued until the end of the piers, and the wave does also end at the end of the stone line. This effect is wanted because the surfers must be able to enter the wave (Figure 7).

Shear stresses are moved upstream if the wave is in the upstream position and the wave is formed in between the piers instead of downstream of the piers. This could prove to be advantageous for the stability of the bridge because the largest scour potential is moved to the scour protected region. On the other hand, the new construction might generate local scour, and threaten the stability of the scour protection.

In the prototype, sandbags (e.g., of biodegradable material) can replace the line of stones in the model (Figure 64). Large sandbags can be lifted down from the bridge by crane, and smaller sandbags can be eased down into the river by boats or kayaks. The proposed scour model can be used to find an appropriate size of the sandbags – the dimensioning could aim at making the sandbags erodible for a certain flood discharge, but stable for lower discharges. The kicker can be introduced by tying a wooden plank to a rope and attaching the rope around the piers. The Eisbach wave is also created by using a system of a plank and ropes.

The post-processing tool of the Froude number can in the future be used in the process of recreating the surf wave. The physical model tests indicate some formations of stones or sandbags that might produce a surf wave. However, due to the small scale, it is not feasible to interpret if the wave is supercritical and not broken by white-water. The geometry of the formation of stones or sandbags can be inserted into the numerical simulation, and the post-processing tool of the Froude number can reveal further information about the properties of the wave.

5.5 Summary and recommendations

It is shown that the experimental formula of equation (2.12) (Meyer-Peter & Müller, 1948) and the numerical applications (Richter, Vereide, Mauko, Havrevoll, & Schneider, 2021; Almeland, Olsen, Bråveit, & Aryal, 2018; Chen, 2021) differ from the result of this study. The computed β-value in this study is higher than the one found by calibration by Chen et al. (2021), and lower than the experimental values proposed by Mayer-Peter and Müller (1948) and The US Army Corps of Engineers (2016). The two-dimensional channel simulations lack sensitivity analysis, and the β-value needs to be studied further. However, this study shows that it is not recommended to choose the k_s-value based on experimental relations only.

Existing sediment scour models are often computationally expensive, and the experimental formulas of scour protection have a limited area of validity. The proposed scour model aims at filling the gap between these methods for scour protection applications. The proposed scour model is based on the first steps of *sediment transport rate models* and *equilibrium scour rate models*. The critical sediment diameter at the bed is computed by finding the sediment diameter which balances the equation: the dimensionless bed shear stress is equal to the bed slope corrected dimensionless critical shear stress (equation (3.4)). The

bed slope correction (equation (2.5)) is tested on 3 different geometries of the two-dimensional channel simulation and produces accurate results.

Three simulations of Nidelva around the Sluppen bridge piers are performed for $Q = 85\frac{m^3}{s}$, $Q = 135\frac{m^3}{s}$, and $Q = 400\frac{m^3}{s}$. The simulated water depth exceeds the upstream measurements, and the downstream water depth is lower than the measurements (Figure 40 and Figure 41). The simulation needs further calibration: the head between the upstream and downstream depth is too large. However, the subcritical flow upstream of the piers, the supercritical flow in between the piers, the subcritical flow downstream of the piers and the recirculation zone behind the piers are observed in the prototype (Figure 4; Smith, N. S., personal communication, 2022).

A map of the critical sediment diameter is produced for each discharge (Figure 45, Figure 46 and Figure 47) by the scour model. The erroneous large hydraulic head between the upstream and downstream water depth is likely causing a false increase in the simulated critical sediment diameter. The critical sediment diameter between the east pier and the east bank increases for increasing discharge and the flow is centred inwards into the flow, towards the location of the maximum scour hole (Figure 47). The scour protection regulation (equation (2.7)) predicts a lower critical sediment diameter than the simulated critical sediment diameter (Figure 45, Figure 46 and Figure 47) for all discharges (Table 12).

The physical model is a qualitative study of how a surf and kayak wave can be recreated under the Sluppen bridge. The tests indicate that it could be possible to create a surf wave with a line of stones or large sandbags. However, the model test has significant scale and geometric errors. It is recommended to repeat the model test with a larger scale or further numerical modelling. Afterwards, the scour model in this study can be used to evaluate the change in critical sediment diameter for the new geometry. The post-processing tool of the Froude number can be used to control that the recreated wave is supercritical.

6 Bibliography

Ahmad, N., Bihs, H., Myrhaug, D., Kamath, A., & Arntsen, A. (2020). Three-dimensional numerical modelling of wave-induced scour around piles in a side-by-side arrangement. *Coastal Engineering. 138*, 132-151.

Almeland, K. S., Olsen, N. R., Bråveit, K., & Aryal, P. R. (2018). Multiple solutions of the Navier-Stokes equations computing water flow in sand traps. *Engineering Application of Computational Fluid Mechanics*, 199-219. doi:https://doi.org/10.1080/19942060.2019.1566094

ANSYS Inc. (2013). *ANSYS Fluent User's Guide.* Canonsburg, Pennsylvania: ANSYS, Inc.

Asiaban, P., Rennie, C. D., & Egsgaard, N. (2021). Sensitivity analysis of adhustable river surf waves in the absence of channel drop. *Water*. doi:https://doi.org/10.3390/w13091287

Baranaya, S., Olsen, N. R., & Sturm, T. (2014). Three-Dimensional Rans Modeling of Flow AroundCircular Piers using Nested Grids. *Engineering Applications of Computational FluidMechanics*.

Bensow, R., Fureby, C., & Liefvendahl, M. (2006). A Comaprative Study of RANS, DES and LES. *26th Symposium on Naval Hydrodynamics.* Rome.

Bihs, H., & Olsen, N. R. (2011). Numerical Modeling of Abutment Scour with the Focus on the Incipient Motion on Sloping Beds. *Journal of Hydraulic Engineering Volume 137, Issue 10*, 1103-1309.

Blocken, B., Stathopoulos, T., & Carmeliet, J. (2007). CFD simulation of the atmospheric boundary layer: wall function problems. *Atmospheric Environment, Volume 41, Issue 2*, 238-252. doi:https://doi.org/10.1016/j.atmosenv.2006.08.019

Briggs, M. J. (2013). Basics of physical modeling in coastal and hydraulic engineering. *US Army Engineer Research and Development Center, Coastal & Hydraulics Laboratory*.

Buffington, J. M., & Montgomery, D. R. (1999). A systematic analysis of eight decades of incipient motion studies, with special reference to gravel-bedded rivers. *Water Resources Research, 33*, 1993-2029. doi: https://doi.org/10.1029/96WR03190

Casey, M., & Wintergerste, T. (2000). *Quality and Trust in Industrial CFD.* ERCOFTAC Special Interest Group.

Celik, I. B., Ghia, U., Roache, P. J., Freitas, C. J., Coleman, H., & Raad, P. E. (2008). Procedure for Estimation and Reporting of Uncertainty Due to Discretization in CFD Applications. *Journal of Fluids Engineering*. doi:https://doi.org/10.1115/1.2960953

CFD Direct. (2018, July 10). Retrieved from OpenFOAM v6 User Guide - 2.3 Breaking of a dam: https://doc.cfd.direct/openfoam/user-guide-v6/dambreak

Chen, Y. e. (2021). Modeling of streamflow in a 30-kilometer-long reach spanning 5years using OpenFOAM 5.x. *Geoscientific Model Development*.

Cheng, Z., Hsu, T., & Calantoni, J. (2017). SedFoam: A multi-dimensional Eulerian two-phase model for sediment transport and its application to momentary bed failure. *Journal of Coastal Engineering, 119*, 32-50. doi:https://doi.org/10.1016/j.coastaleng.2016.08.007

Cho, Y., Dao, M., & Nichols, A. (2022). Computational fluid dynamics simulation of rough bed open channels using openFOAM. *Frontiers in Environmental Science*. doi:https://doi.org/10.3389/fenvs.2022.981680

Constantinescu, G., & Koken, M. (2011). The structure of turbulent flow in an open channel bend of strong curvature with deformed bed: Insight provided by detached eddy simulati. *Water Resources Research, 47*. doi:https://doi.org/10.1029/2010WR010114

Dey, S. (2001). Experimental study on incipent motion of sediment particles on generalized sloping fluvial beds. *Journal of Sediment Reasearch*.

Engelund, F., & Fredsoe, J. (1976). Sediment Transport Model For Straight Alluvial Channels. *Hydrology Reasearch. 7.*, 293-306.

Fergus, T., Hoseth, K. A., & Sæterbø, E. (2010). *Vassdragshåndboka.* Trondheim: Tapir Akademisk Forlag.

Fluent Inc. (2003). *FLUENT 6.1 User's Guide.* Lebanon, New Hampshire: Fluent Inc.

Fremstad, E., & Thingstad, P. (2007). *Nidelva, Trondheims hjerte. Bli med ut 7.* Trondheim: NTNU Vitenskapsmuseet.

Frisch, U. (1989). *Lectures on turbulence and lattice gas hydrodynamics. Lecture notes on turbulence.*

Geimer, T. (2014). *River Surfing in Munich*. Retrieved from "Keep Surfing" – Riding the Eisbach: https://www.surfingmed.com/recent-posts/river-surfing-in-munich/

Google Earth Pro. (2017, July 20). Google Earth. Trondheim, Norway.

Hellevik, L. R. (2020). *Numerical Methods for Engineers.* Trondheim: Department of Structural Engineering, NTNU.

Hey, R. D. (1979). Flow Resistance in Gravel-Bed Rivers. *Journal of Hydraulic Division, 105*. doi:https://doi.org/10.1061/JYCEAJ.0005178

Hoff, T., Blocken, B., & Harten, M. (2010). 3D CFD simulations of wind flow and wind-driven rain shelter in sports stadia: Influence of geometry. *Builing and environment, 46*, 22-37. doi:https://doi.org/10.1016/j.buildenv.2010.06.013

Jalal, H. K., & Hassan, W. H. (2020). Three-dimensional numerical simulation of local scour around circular bridge pier using Flow-3Dsoftware. *IOP Conference Series:* (p. 012150). Baghdad: Materials Science and Engineering.

Jenssen, L., & Tesaker, E. (2009). *Veileder for dimensjonering av erosjonssikringer av stein.* Oslo, Norway: The Norwegian Water Resources and Energy Directorate.

Jesudhas, V., Balanchandar, R., & Murzyn, F. (2018). IDDES Evaluation of oscillating hydraulic jumps. *E3S Web of Conferences.* doi:DOI: 10.1051/e3sconf/20184005067

Keulegan, G. H. (1938). Laws of turbulent flow in open channels. *Journal of Reasearch of the National Berau of Standards, Volume 21*.

Kim, H., Chen, H., & Briaud, J. (2020). Numerical Simulation of Scour Hole Backfilling in Unidirectional Flow. *Journal of Hydraulic Engineering. 148.*, 04022013.

Kitware, Inc. (2023). *ParaView*. Retrieved from https://www.paraview.org

Lai, Y. G., & Wu, K. (2018). Bridge scour simulation with a new 3D flow and sediment transport model. *Proc., 9th Int. Conf. on Scour and Erosion.* Oxfordshire.

Lai, Y. G., Liu, X., Bombardelli, F. A., & Song, Y. (2022). Three-Dimensional Numerical Modeling of Local Scour: A State-of-the-Art Review and Perspective. *Journal of Hydraulic Engineering, 148*. doi:https://doi.org/10.1061/(ASCE)HY.1943-7900.0002019

Lia, L., & Havrevoll, O. H. (2021). *Lecture notes on modelling laws. Vannkraftverk og vassdragsteknikk, videregående kurs TVM4128.* Trondheim: NTNU.

Lysne, D. K. (1969). Movement of Sand in Tunnels. *Journal of Hydraulic Division Volume 95 Issue 6*.

Mandviwalla, X., Qwist, J. R., & Christensen, E. D. (2020). Prediction of equilibrium scour holes using optimization procedures. *Coastal Engineering Proceedings*. doi:https://doi.org/10.9753/icce.v36v.papers.12

Martinez, B. (2011). *Wind resource in complex terrain with OpenFOAM.* Technical University of Denmark. Nation Laboratory for Sustainable Energy.

Meyer-Peter, E., & Müller, R. (1948). Formulas for Bed-Load transport. *Proceedings of 2nd meeting of the International Association for Hydraulic Structures Research*, (pp. 39-64). Delft.

Miljøpakken. (2022, January). *Nydalsbrua -ny bru på Sluppen*. Retrieved from Miljøpakken: https://miljopakken.no/prosjekter/sluppen-bru

Nemry, F., & Demirel, H. (2012). *infrastructures, Impacts of Climate Change on Transport: A focus on road and rail transport.* Luxenbourg: European Commision.

NTNU. (2020). *NTNU*. Retrieved from TKT4140 - Numeriske beregninger: https://www.ntnu.no/studier/emner/TKT4140/2020#tab=omEmnet

NTNU. (2020). *NTNU*. Retrieved from TVM4155 - Numeriske modeller og hydraulikk: https://www.ntnu.no/studier/emner/TVM4155/2020#tab=omEmnet

Olsen, N. R. (2015). *Numerisk modellering av kapasitet på flomløp- et litteraturstudium.* Trondheim: Norges vassdrags- og energidirektorat.

Olsen, N. R. (2017). *Numerical Modelling and Hydraulics.* Trondheim: Department of Hydraulic and Environmental Engineering NTNU.

OPEN CASCADE, EDF, CEA. (2022). Retrieved from SALOME: https://www.salome-platform.org/

OpenCDF Ltd. (2018). *Hydrostatic pressure effects*. Retrieved from OpenFOAM: User Guide v2112: https://www.openfoam.com/documentation/guides/latest/doc/guide-applications-solvers-variable-transform-p-rgh.html

OpenCFD Ltd. (2016). *Common Combinations Pressure-velocity systems*. Retrieved from User Guide v2112: https://www.openfoam.com/documentation/guides/latest/doc/guide-bcs-common-combinations.html

OpenFOAM Foundation Ltd. (2021). *createFields.H*. Retrieved from C++ Source Code Guide: https://cpp.openfoam.org/v9/solvers_2multiphase_2interFoam_2createFields_8H_source.html

OpenFOAM Foundation Ltd. (2021). *gh.H*. Retrieved from C++ Source Code Guide: https://cpp.openfoam.org/v9/gh_8H_source.html

OpenFOAM Foundation Ltd. (2022). OpenFOAM User Guide version 10. In C. J. Greenshields. 12. Retrieved from https://foam.sourceforge.net/docs/Guides-a4/OpenFOAMUserGuide-A4.pdf

Pang, A. L., Skote, M., Lim, S. Y., Gullman-Strand, J., & Morgan, N. (2016). A numerical approach for determining equilibrium scour depth around a mono-pile due to steady currents. *Journal of Applied Ocean Research, 57*, 114-124. doi:https://doi.org/10.1016/j.apor.2016.02.010

Parker, G. W., Bratton, L., S., & D., A. (1997). *Stream Stability and Scour Assessments at Bridges in Massachusetts.* Marlborough: Massachusetts Highway Department Bridge Section. doi:https://doi.org/10.3133/ofr97558

Pfister, M., & Chanson, H. (2014). Two-phase air-water flows: Scale effects in physical modelling. *Journal of Hydrodynamics*, 291-298. doi:https://doi.org/10.1016/S1001-6058(14)60032-9

Richter, W., Vereide, K., Mauko, G., Havrevoll, O. H., & Schneider, J. (2021). Retrofitting of Pressurized Sand Traps in Hydropower Plants. *Water*. doi:https://doi.org/10.3390/w13182515

Roulund, A., Sumer, B. M., Fredsøe, J., & Michaelsen, J. (2005). Numerical and experimental investigation of flow and scour around a circular pile. *Journal of Fluid Mechanics. 543.*, 351-401.

Rüther, N., Singh, J. D., Olsen, N. R., & Atkinson, E. (2005). 3-D computation of sediment transport at water intakes. *Water management. 158.*, 1-7.

Shields, A. (1936). *Application of similarity principles and turbulence research to bed-load movement.* California Institute of Technology. California: United States Department of Agriculture Soild Conservation Service.

SimFlow. (2017). *SimFlow overview*. Retrieved February 2, 2023, from Solution: https://help.sim-flow.com/documentation/panels/solution

Song, Y., Xu, Y. I., & Liu, X. (2022). Scour modeling based on immersed boundary method: A pathway to practical use of three-dimensional scour models. *Journal of Coastal Engineering, 171*. doi:https://doi.org/10.1016/j.coastaleng.2021.104037

Soulsby, R. (1997). *Dynamics of Marine Sands.* London: Thomas Telford Pubications.

Statens vegvesen. (2022, December 20). Retrieved from Styrker overvåkingen av riksvegbruer i elver og vann: https://www.vegvesen.no/om-oss/presse/aktuelt/2022/12/styrker-overvakingen-av-riksvegbruer-i-elver-og-vann/

Statkraft. (2022). *Leirfossene vannkraftverk*. Retrieved February 4, 2023, from Statkraft: https://www.statkraft.no/om-statkraft/hvor-vi-har-virksomhet/norge/leirfossene-vannkraftverk/

Sun, R., & Xiao, H. (2016). SediFoam: A general-purpose, open-source CFD–DEM solver for particle-laden flow with emphasis on sediment transport. *Journal of Computers & Geosciences, 89*, 207-219. doi:https://doi.org/10.1016/j.cageo.2016.01.011

Teuber, K., Broecker, T., Bayon, A., Nutzmann, G., & Hinkelmann, R. (2019). CFD-modelling offree surface flows in closed conduits. *Progress in Computational Fluid Dynamics, 19*. doi:https://doi.org/10.1504/PCFD.2019.103266

The Norwegian Water Resources and Energy Directory. (2023, February). *Sildre*. Retrieved February 2023, from Rate: https://sildre.nve.no/station/123.20.0

The OpenFOAM Foundation Ltd. (2014, February 17). *The OpenFOAM Foundation*. Retrieved from OpenFOAM 2.3.0: Multiphase Modelling : https://openfoam.org/release/2-3-0/multiphase/

Thorenz, C., & Strybny, J. (2012). On the numerical modelling of filling-emptying system for locks. Hamburg: Hydraulic Engineering Repository. Retrieved from https://hdl.handle.net/20.500.11970/106397

US Army Corps of Engineers. (2016). *HEC-RAS River Analysis System.* US Army Corps of Engineers Hydrologic Engineering Center.

Van Rijn, L. C. (1982). Equivalent Roughness of Alluivial Bed. *Journal of the Hydraulics Division, 108*, 1215-1218. doi:doi:10.1061/JYCEAJ.0005917

Van Rijn, L. C. (1987). Mathematical Modelling of Morphological Processes in the Case of Suspended Sediment Transport. *Delft Hydraulics Communication. 382.*

Versteeg, H. K., & Malasekera, W. (2007). *An Introduction to Computational Fluid Dynamics The Finite Volume Method .* Essex: Pearson Education Limited.

Walstra, D. J., van Rijn, L. C., van Ormondt, M., Briere, C., & Talmon, A. M. (2007). The effect of bed slope and wave skewness on sediment transport and morphology. *Coastal Sediments*, 137-150. doi:https://doi.org/10.1061/40926(239)11

Wardhana, K., & Hadipriono, F. C. (2003). Analysis of Recent Bridge Failures in the United States. *Journal of Performance of Constructed FacilitiesVolume 17, Issue 3*, 144-150. doi:10.1061/~ASCE!0887-3828~2003!17:3~144!

Wolf Dynamics. (2014, February). *Multiphase flows modeling in OpenFOAM(R): Guided Tutorials*. Retrieved from Online Training:

http://www.wolfdynamics.com/training/mphase/OF2021/mphase_2021_OF8_guided_tutorials.pdf

Xi, C. (2005). *Preconditioners for iterative solutions of large-scale linear systems arising from Biot's consolidation equation.* Doctoral thesis, National University of Singapore, Department of Mathematics, Singapore.

Zhao, M. (2022). Review on Recent Development of Numerical Modelling ofLocal Scour around Hydraulic and Marine Structures. *Journal of Marine Science and Engineering, Volume 10*. doi:https://doi.org/10.3390/jmse10081139

Zhao, M., Cheng, L., & Zang, Z. (2010). Experimental and numerical investigation of local scour around a submerged vertical circularcylinder in steady currents. *Coastal Engineering. 57.*, 709-721.

Appendix

Appendix 1: DTM provided by Norwegian University of Science and Technology.

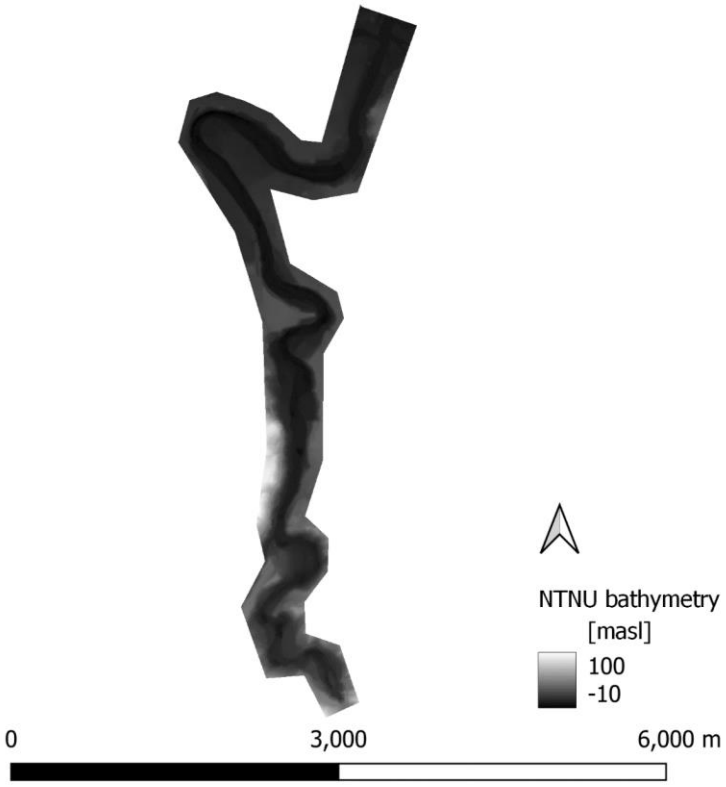

Appendix 2: Drawing of Sluppen bridge piers.

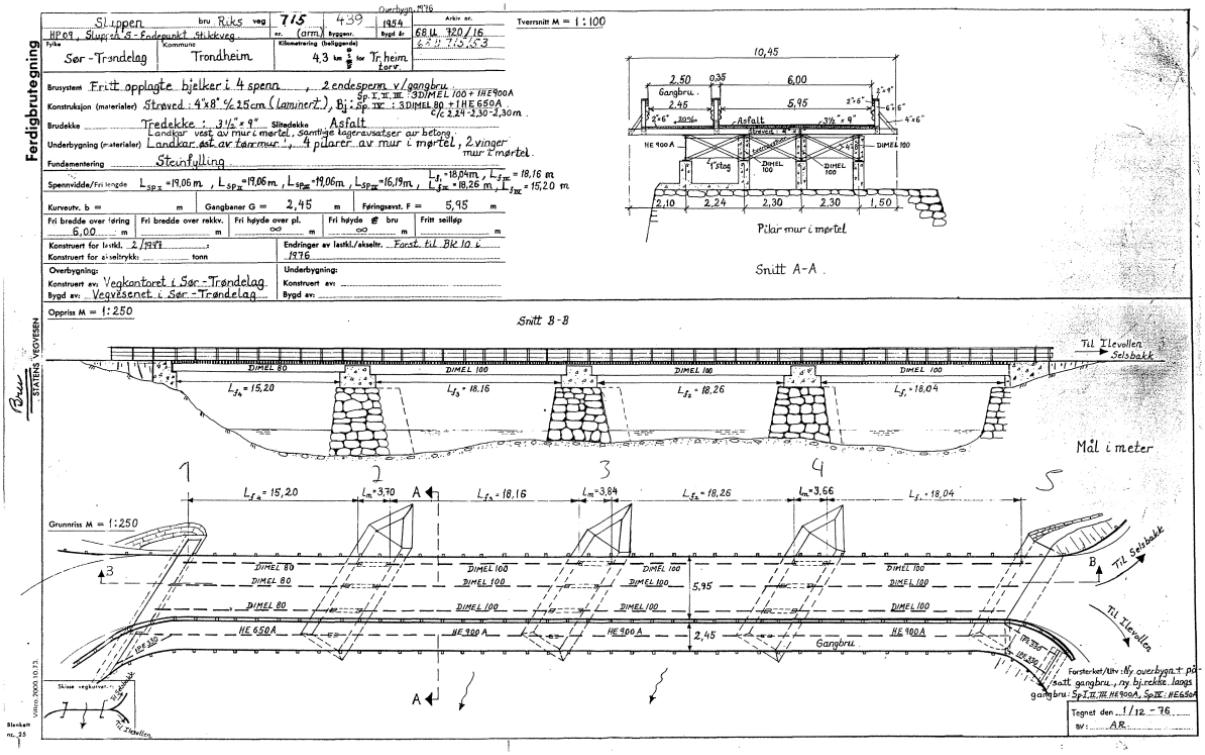

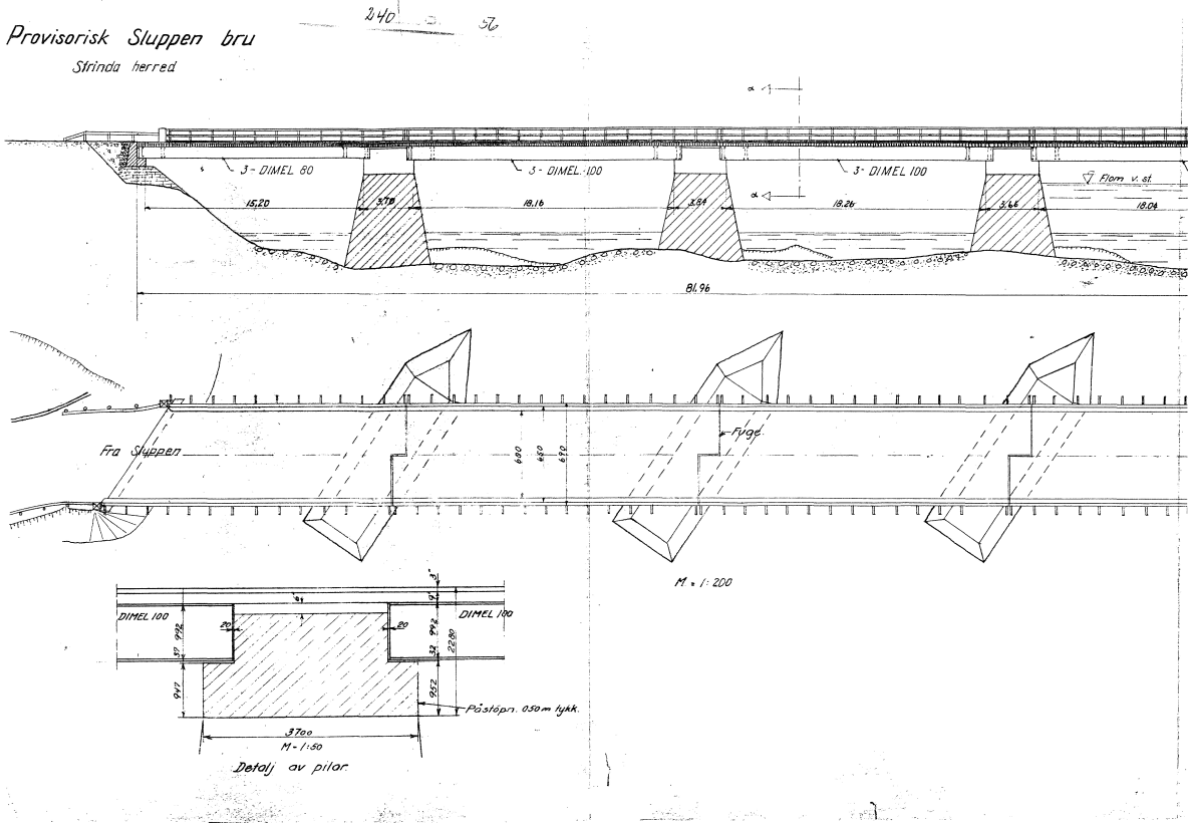

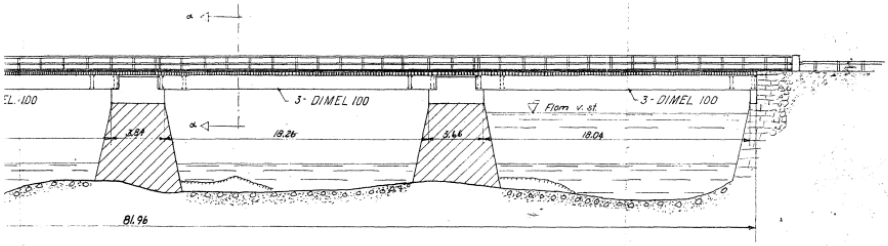

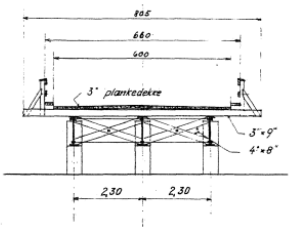

Snitt α-α

M. = 1:100

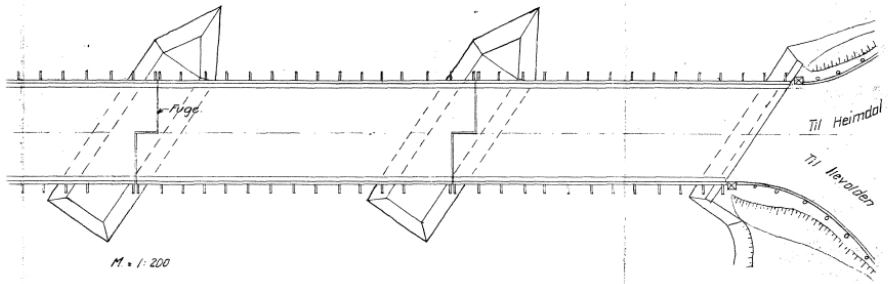

M. = 1:200

Stålbjelkebru med tredekke
Lysvidde: 15,20 + 18,16 + 18,24 + 18,04
Spennvidde: 16,19 + 19,06 + 19,06 + 19,06
Total lengde: 81,96
Kjørebanebredde: 6,00
Lastklasse 2/1947
Dekke og rekkverk av Rüpingimpreg materialer.

Ny ombygning 1954.
Km 4,0

Herred: Strinda	Bruksnr. 39
Last: 2/ 47	16,0
Tillatt 100	
Sluppen bru	
Kart: 165/63	

Vegvesenet i Sør-Trøndelag 20-1-1955

J.Nº 3696 1927

Sluppen bro.

Snitt parallel broaksen.
1:200

Snitt tvers strømretningen.
1:200

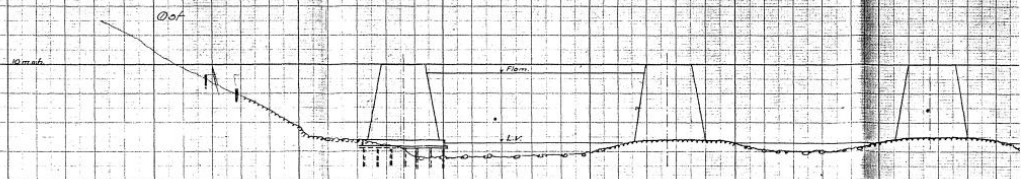

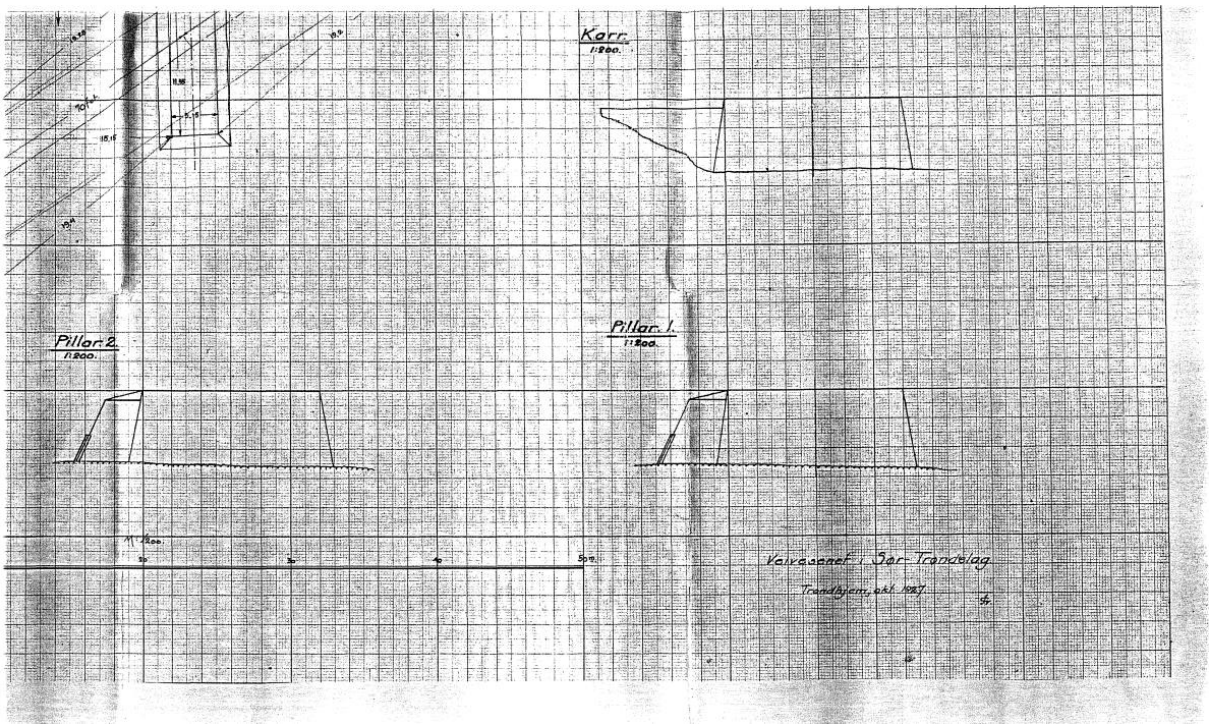
Korr.
1:200.
Pillar 2.
1:200.
Pillar 1.
1:200.
M. 1:200.
Valvegaard i Sør-Trøndelag
Trondhjem, okt. 1927.

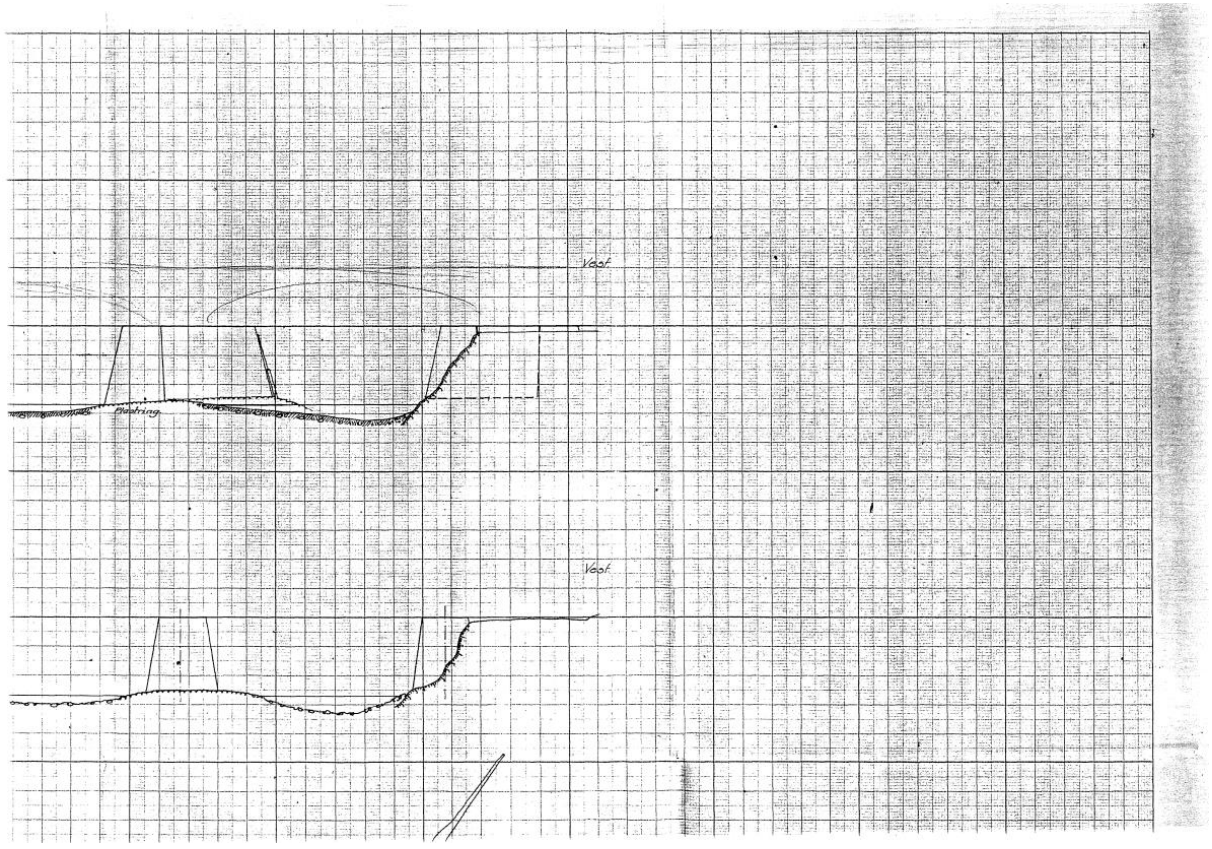
Vaal
Vaal

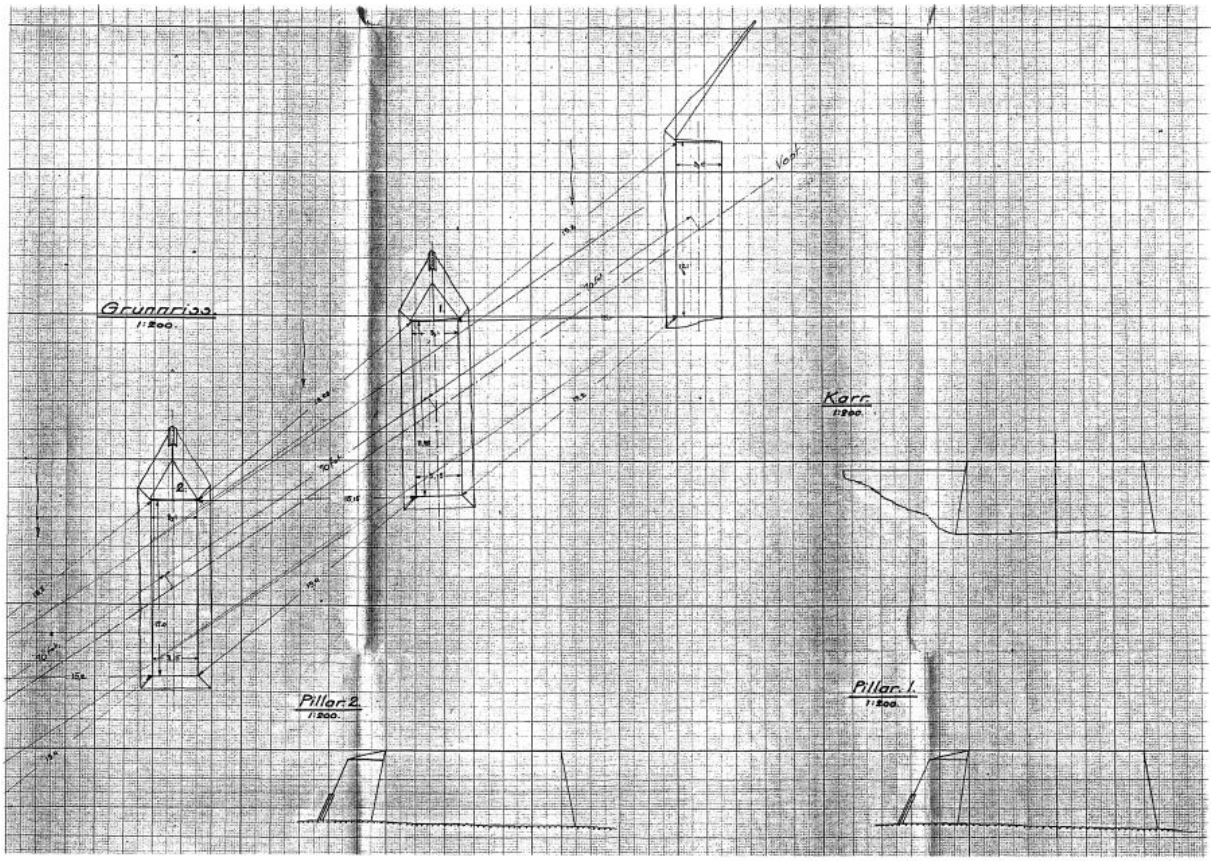
Grundriss.
1:200.
Pillar 2.
1:200.
Pillar 1.
1:200.
Korr.
1:200.

Appendix 3: Location and angle of the piers.

Appendix 4: DEM of Bathymetry from SWECO and the location of the piers.

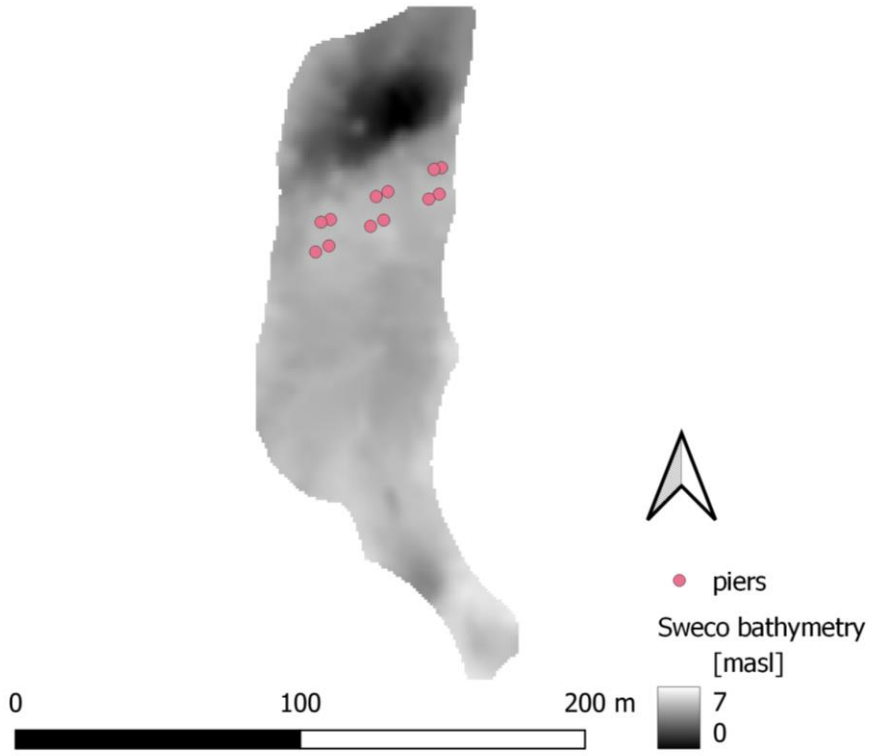

Appendix 5: ADCP measurement points measured by SWECO.

Appendix 6: Settings for Gaussian Filter.

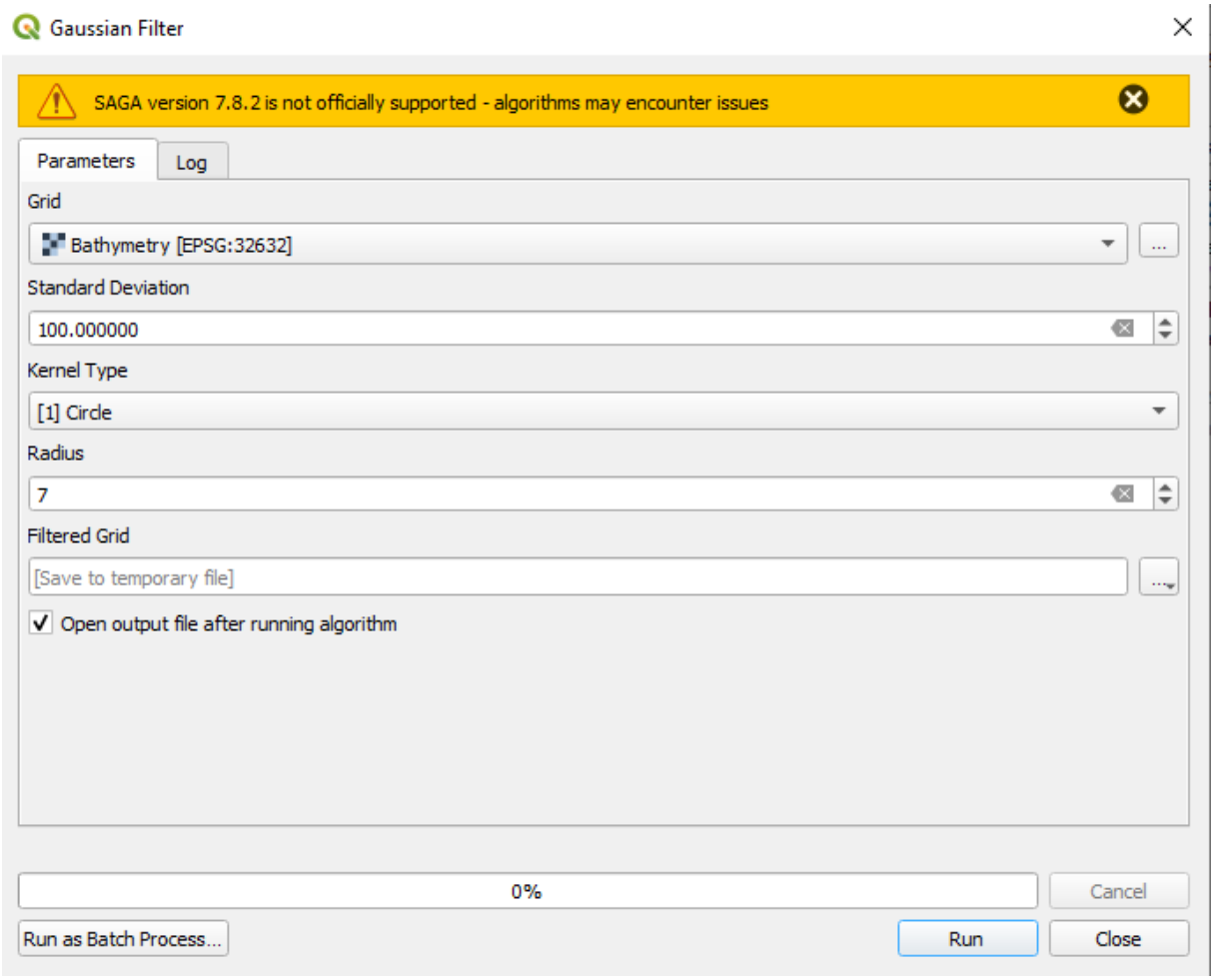

Appendix 7: Description of the attachments.

1. ParaView/turbulentKineticEnergy.py: This ParaView macro outputs a CSV file of the turbulent kinetic energy along a slice of the domain. The input is a VTK file of the turbulent kinetic energy extracted in the cell centre closest to a wall. The code is first created using the python trace functionality of ParaView. Then, the code is modified so it can post-process several cases, timesteps and slices at once. This code is only used in two-dimensional channel simulations.

2. ParaView/wallShearStressUtility.py: This ParaView macro outputs a CSV file of the shear stress based on the *wallShearStress* utility along a slice of the domain. The input is a VTK file of the *wallShearStress* utility. The code is first created using the python trace functionality of ParaView. Then, the code is modified so it can post-process several cases, timesteps and slices at once. This code is only used in two-dimensional channel simulations.

3. ParaView/freeSurface.py: This ParaView macro outputs a CSV file of the free surface along a slice of the domain. The input is a VTK file of the surface where the α-fraction is equal to 0.5. The code is first created using the python trace functionality of ParaView. Then, the code is modified so it can post-process several cases, timesteps and slices at once.

4. ParaView/froudeNumber.py: This ParaView macro outputs CSV files of the velocity along a slice, the free surface along a slice and the riverbed along a slice. The input is a FOAM file of the simulation and a VTK file of the surface where the α-fraction is equal to 0.5 and a VTK file of the unstructured riverbed coordinates. The code is first created using the python trace functionality of ParaView. Then, the code is modified so it can be applied to any case by changing the name of the case and the paths. In addition, the code is modified to post-processes several slices at once. The CSV files are used as input for the computation of the Froude number.

5. ParaView/riverbedShearStress.py: This ParaView macro outputs CSV files of the geometric edge of the simulation, the velocity 2cm above the riverbed and the product of the α-fraction, the shear stress from the *wallShearStress* utility and the density of water (1000 kg/m^3). The input is VTK files of the shear stress from the *wallShearStress* utility, the free surface where the α-fraction is equal to 0.5, the velocity 2cm above the riverbed and the coordinates of the riverbed. The code is first created using the python trace functionality of ParaView. Then, the code is modified so it can be applied to any case by changing the name of the case and the paths. The CSV files are used as input in the generation of computation of the critical sediment diameter. The edge of the simulation is used as geometric limits of the computation (e.g., to not compute a critical sediment diameter inside of the piers). The velocity near the bed and the coordinates of the riverbed are used to compute the bed slope correction. The product of the α-fraction, the shear stress from the *wallShearStress* utility and 1000 is equal to the shear stress at the riverbed and is used to compute the critical sediment diameter.

6. CriticalSedimentDiameter.py: This script uses the output of the attachment ParaView/riverbedShearStress.py to compute the critical sediment diameter as described in section *3.2 Scour model*.

7. codeFroudeNumber.py: This script computes the Froude number as described in section 3.3.1 Verification of post-processing of Froude number. The code uses the output of the script ParaView/froudeNumber.py as input data.

8. 2Dchannel: the *2Dchannel* directory contains the *0*, *constant* and *system* directories of the two-dimensional channel simulation with a unit discharge of $q = 1\frac{m^2}{s}$ and a sand-grain roughness of $k_s = 0.1m$. The log.checkmesh and the Allrun file are also included.

9. Q135Coarse: the *Q135Coarse* directory contains the *0*, *constant* and *system* directories for the simulation of Nidelva through the Sluppen bridge for $Q = 135\frac{m^3}{s}$ and a coarse mesh. Log files of the *checkMesh* and *snappyHexMesh* utilities are attached in addition to the Allrun file.

10. Q135Fine: the *Q135Coarse* directory contains the *0*, *constant* and *system* directories for the simulation of Nidelva through the Sluppen bridge for $Q = 135\frac{m^3}{s}$ and a fine mesh. Log files of the *checkMesh*, and *snappyHexMesh* utilities are attached in addition to the Allrun file.

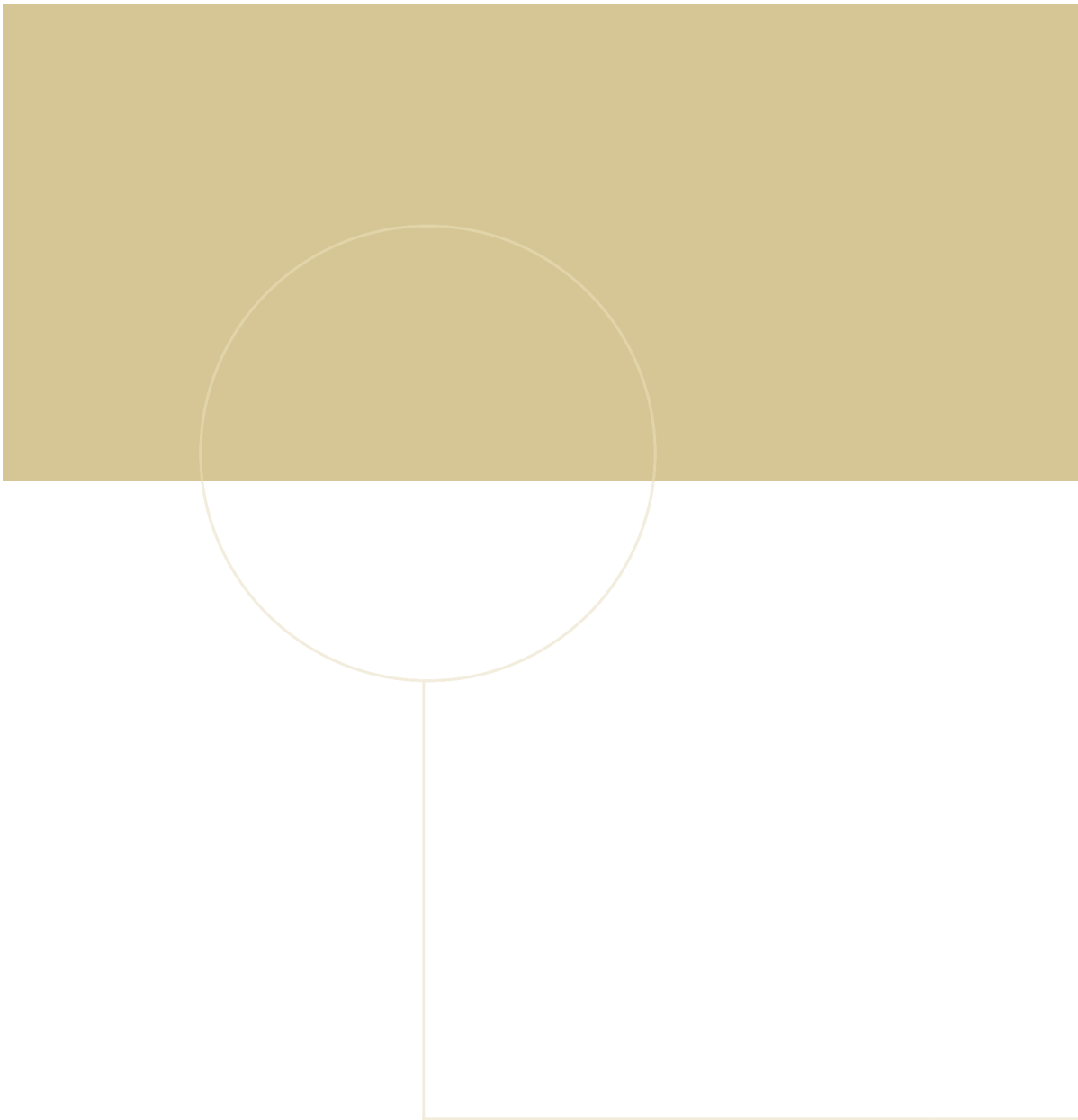

NTNU

Norwegian University of
Science and Technology